

Composite Structures

Beyond Time: Enhancing Corrosion Resistance of Geopolymer Concrete and BFRP Bars in Seawater --Manuscript Draft--

Manuscript Number:	COMSTR-D-23-02056R1
Article Type:	Full Length Article
Keywords:	geopolymer concrete; Basalt fiber reinforced polymer (BFRP) bars; Seawater; Time-dependence; Interface characteristic
Corresponding Author:	Yunchao Tang Guangxi University CHINA
First Author:	Zheng Chen
Order of Authors:	Zheng Chen Jiamin Yu Yumei Nong Yongmin Yang Hexin Zhang Yunchao Tang
Abstract:	<p>To improve the durability of Basalt fiber reinforced polymer (BFRP) bars reinforced geopolymer concrete (GPC), it is important to study the time-dependent variation of the corrosion resistance ability of GPC and BFRP in a seawater environment. This paper presents an experimental investigation to study the time-dependent mechanical properties and durability of BFRP bars and geopolymer materials synthesized. The resulting GPC and Portland cement (PC) concrete were exposed to artificial seawater. The corrosion resistance of geopolymer (GP) mortar and PC mortar was evaluated by studying the migration ability and pore structure in corrosive ions attack in artificial seawater. In addition, the dual interface transition zones (ITZs) characteristics of BFRP reinforced GPC under artificial seawater were also investigated by SEM and BSE tests. The results showed that the volume expansion rate and strength loss rate of GPC decreased by 77.6% and 8.7%, respectively. In addition, the effect of seawater corrosion on the tensile strength of BFRP bars increases with the increase of bars' diameter, and the ultimate strengths of BFRP bars with diameters of 6 mm and 8 mm were 695 MPa and 663 MPa, respectively. This research can provide a theoretical basis for the service life prediction of BFRP reinforced geopolymer concrete.</p>
Suggested Reviewers:	Zhe Xiong, Dr. Associate Professor, Guangdong University of Technology gdgyxz263@gdut.edu.cn Wengui Li, Dr. Professor, University of Technology Sydney wengui.li@uts.edu.au Guijun Xian, Dr. Prof., Harbin Institute of Technology gjxian@hit.edu.cn Shishun Zhang, Dr. Prof., Huazhong University of Science and Technology shishun@hust.edu.cn Yu Zheng, Dr. Prof., Dongguan University of Technology zhengy@dgut.edu.cn Peiyan Huang, Dr. Prof., South China University of Technology

	pyhuang@scut.edu.cn
Response to Reviewers:	

Dear Prof. Heng Hu
Editor-in-Chief
Composite Structures

We wish to re-submit the manuscript titled titled “*Beyond Time: Enhancing Corrosion Resistance of Geopolymer Concrete and BFRP Bars in Seawater*”.

The manuscript has been rechecked and appropriate changes have been made in accordance with the reviewers’ suggestions. The responses to their comments have been prepared and attached herewith. The manuscript has been proofed by language edit center.

We thank you and the reviewers for your thoughtful suggestions and insights, which have enriched the manuscript and produced a better and more balanced account of the research. We look forward to working with you and the reviewers to move this manuscript closer to publication in COMSTR.

Thank you for your consideration. We look forward to hearing from you.

Sincerely,

Yunchao Tang

State Key Laboratory of Featured Metal Materials and Life-cycle Safety for Composite Structures

Guangxi University

Email: joshua0115@gxu.edu.cn

A handwritten signature in black ink, appearing to read 'Yunchao Tang', written over a horizontal line.

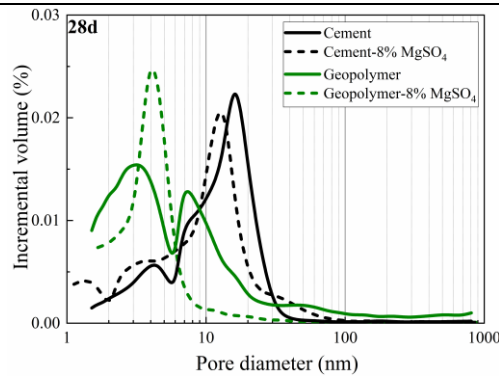
Manuscript Number: COMSTR-D-23-020568

Title: “Beyond Time: Enhancing Corrosion Resistance of Geopolymer Concrete and BFRP Bars in Seawater”

Authors: Zheng Chen; Jiamin Yu; Yumei Nong; Yongmin Yang; Hexin Zhang; and Yunchao Tang

Serial No.	Comments	Authors' Response	Action Taken
Comments from Reviewer #1			
Comment 1	<p>The citation format should follow the journal's guidelines. To improve the research depth of the paper, it is recommended that the author refer to some of the latest relevant papers, such as:</p> <p>https://doi.org/10.1016/j.jmrt.2022.11.135</p> <p>https://doi.org/10.1016/j.ocecoaman.2022.106038</p> <p>https://doi.org/10.1016/j.job.2021.103828</p> <p>https://doi.org/10.1016/j.compstruct.2020.113078</p> <p>https://doi.org/10.1016/j.conbuildmat.2020.121399</p> <p>https://doi.org/10.1016/j.conbuildmat.2020.122195</p> <p>https://doi.org/10.1016/j.conbuildmat.2021.123218</p>	<p>The authors thank this comment from the reviewer.</p> <p>Some of the suggested articles have now been added to the Introduction</p>	<p>Some of the suggested articles have now been referred as [37-40] in the Introduction, to suitably address this comment.</p>
Comment 2	Was the equipment shown in Figure	The authors appreciate the valuable	The Section 3.1.2, (lines 296-305,

	<p>2designed and developed by the authors themselves? It is indeed an interesting aspect of this study. However, the device lacks a detailed description of the equipment. It would be helpful if the authors could provide a more comprehensive explanation of the design, components, and functioning of the equipment. This would allow readers to better understand its novelty and relevance to the research conducted in this study.</p>	<p>comment from this reviewer.</p> <p>The suggested detailed description of the equipment has now been added to the Section 3.1.2, (lines 296-305, page 11)</p>	<p>page 11) has now been improved to address this comment.</p>
<p>Comment 3</p>	<p>The meaning of symbols $F_c(t)$ and $F_w(t)$ in Eqs.(4) and Eqs. (5) need to be clarified.The meaning of symbols C and C_0 in Eqs. (8) and Eqs. (9) need to be clarified.</p>	<p>The authors appreciate this comment from the reviewer.</p> <p>$F_c(t)$ is strength retention rate of concrete in marine environments in immersion time t. $F_w(t)$ is strength retention rate of GPC in marine environments in immersion time t. C_0 is the chloride concentration on the exposed surface of concrete. C is the free chloride concentration in diffusion time t</p>	<p>The meaning of $F_c(t)$ and $F_w(t)$ in Eqs. (4) and (5) have now been clarified in Section 4.2 to address this comment.</p> <p>The meaning of C and C_0 in Eqs. (8) and (9) have now been clarified in Section 4.3 to address this comment.</p>
<p>Comment 4</p>	<p>The label of the curve in Figure 7(c) is mislabeled</p>	<p>The authors thank this comment from the reviewer.</p> <p>The new Figure 7(c) in the revised manuscript also is attached below.</p>	<p>To suitably address this comment, the new Figure 7(c) are changed in the revised manuscript.</p>



(c) Pastes with MgSO₄

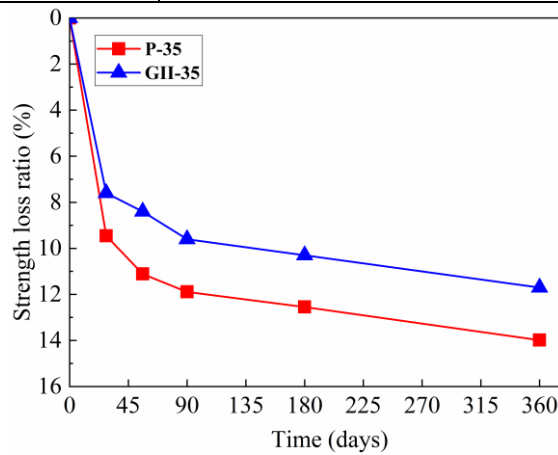
Fig.7. Pore size distribution of geopolymer and cement pastes with NaCl, Na₂SO₄ and MgSO₄

<p>Comment 5</p>	<p>The authors studied the effect of Cl⁻, SO₄²⁻ and Mg²⁺ on the pore structure of geopolymers under seawater erosion. However, the article has less analysis of magnesium ions, please explain further the effect of magnesium ion erosion on geopolymers in chapter 4.4.</p>	<p>In order to help address this comment, the author has now been added at lines 483-491 on page 19.</p> <p>This may be due to the fact that in the early stage of erosion, the erosion products of SO₄²⁻ first fill the pores, thus leading to a decrease in the median pore size like of the cement paste. In addition, the addition of 8% Mg²⁺ resulted in a significant increase in the number of macropores in the cement paste and a significant decrease in the percentage of macropores in the geopolymer. This suggests that the erosive effect of Mg²⁺ may be more likely to convert the hydration product C-S-H gel to M-S-H, leading to the appearance of loose macropores in the structure. These results indicate that geopolymers have good resistance to penetration of erosive materials due to their compact pore structure.</p>	<p>A detailed analysis has now been added at lines 484-492 on page 19 to suitably resolve this comment in the revised manuscript.</p>
<p>Comment 6</p>	<p>The graphs, tables and figures are of very good standard.</p>	<p>The authors thank this comment from the reviewer</p>	<p>No action taken at this stage.</p>
<p>Comment 7</p>	<p>The data and analysis provided in the paper are extensive and detailed. However, I believe that the content could be slightly</p>	<p>We have adjust the tables and charts based on the reviewer's comment.</p>	<p>Figure 7 has been modified.</p>

	condensed by removing some secondary data tables and charts.		
--	--	--	--

Serial No.	Comments	Authors' Response	Action Taken
Comments from Reviewer #2			
Comment 1	The introduction of other studies is summarized thoroughly in the preface, but it would be beneficial to provide further explanation of the content and significance of this paper's study.	The content and significance of this paper's study has now been lines 211-220 on page 7.	The manuscript was left unchanged in respect to this comment.
Comment 2	In Table 9, the authors investigated the impact of different dosages of NaCl, Na ₂ SO ₄ , and MgSO ₄ added into the GP paste. However, the text does not provide a basis for the chosen dosage of marine corrosive substances. Please provide further reasons for this choice of dosage in chapter 3.3.3.	The authors thank this comment from the reviewer. In Table 9, the purpose of mixing NaCl, Na ₂ SO ₄ and MgSO ₄ inside the slurry is only to compare the corrosion ion migration resistance of GP with that of ordinary cement slurry, so the dosage is not selected according to the content of marine corrosive substances. Secondly, the content of corrosive ions in the actual marine environment is low, and the effect of studying the ion migration performance in a short time is not obvious. In the existing research literature [1-5], the content of chloride ion is basically taken as 0%~5% and sulfate ion is basically taken as 0%~10%, but the reason for the selection of dosage has not been shown. Therefore, in this paper, the content of sodium chloride is taken as 3.5% and 5%, and the content of sodium sulfate and magnesium sulfate is taken as 3% and 8%. [1] https://doi.org/10.1016/j.conbuildmat.2018.12.168 [2] https://doi.org/10.1016/j.conbuildmat.2021.122970 [3] https://doi.org/10.1016/j.conbuildmat.2017.09.159 [4] https://doi.org/10.1061/(ASCE)MT.194	No action taken at this stage.

		3-5533.0001618 [5] https://doi.org/10.1016/j.compositesb.2019.107689	
Comment 3	In Figure 4.(b), it is suggested to change the strength loss ratio from 0-16 to 16-0. This change would present a clearer representation of the intensity loss between GPC and PC concretes.	The authors thank this comment from the reviewer. the new Figure 4(b) in the revised manuscript also is attached below.	To suitably address this comment, the new Figure 4(b) are changed in the revised manuscript.



(b) Strength loss

Fig. 4. The corrosion resistance of GPC and PC concretes

Comment 4	Discussion about the limitations of the study is suggested	Yes, the authors agree fully with this reviewer here Yet, the present study focuses on analyzing the ionic attack resistance of BFRP reinforced geopolymer concrete by simulating seawater environment in the laboratory. However, in real marine environments, the migration of ions is not only by diffusion, but there may be convective effects under hydrostatic pressure. Certain key questions are still waiting to be considered: How to simulate more realistic ocean conditions is further investigated through systematically designed experiments? What is the effect of competing antagonistic effects on the	As advised by Reviewers 2, the Section 5 on “Conclusions” summarizes and lists the limitations from the present study. As well, the future direction is also detailed in the revised manuscript.
-----------	--	---	---

		<p>performance of BFRP reinforced geopolymer concrete under multiple-ion combined attack in marine environments?</p> <p>Further studies, with systematically designed experiments and research including long-term observation that will help tune the proposed mathematical models will address the above questions.</p>	
--	--	---	--

Declaration of interests

The authors declare that they have no known competing financial interests or personal relationships that could have appeared to influence the work reported in this paper.

CRedit authorship statement

Zheng Chen: conceptualization, software, validation, and writing the original draft. **Jiamin Yu:** reviewing and editing. **Yumei Nong, Yongmin Yang:** software, data curation and editing. **Hexin Zhang:** investigation, data curation and validation. **Yunchao Tang:** Supervision, conceptualization and editing.

46 mortar and PC mortar was evaluated by studying the migration ability and pore
47 structure in corrosive ions attack (Cl^- , SO_4^{2-} , Mg^{2+}) in artificial seawater. Moreover,
48 the time-dependent tensile strength of BFRP was comparatively investigated by
49 immersing in different solutions (tap water, artificial seawater, and alkaline simulated
50 seawater). In addition, the dual interface transition zones (ITZs) characteristics of
51 BFRP reinforced GPC under artificial seawater were also investigated by SEM and
52 BSE tests. The results showed that the volume expansion rate and strength loss rate of
53 GPC decreased by 77.6% and 8.7%, respectively, after 360 days of seawater corrosion
54 compared with PC concrete. This enabled the development of a time-dependent
55 strength model of GPC in marine environments. The coefficient of ions diffusion in
56 GP mortar is much lower than that of PC mortar, and GP mortar shows excellent
57 resistance to ion migration. In addition, the effect of seawater corrosion on the tensile
58 strength of BFRP bars increases with the increase of bars' diameter, and the ultimate
59 strengths of BFRP bars with diameters of 6 mm and 8 mm were 695 MPa and 663
60 MPa, respectively. The tensile strength degradation model of BFRP bars in
61 geopolymer concrete under seawater corrosion was established. After 360 days of
62 seawater immersion, the average porosity of the ITZ between geopolymer and
63 aggregates, and the average porosity of the ITZ between geopolymer and BFRP bars
64 increased insignificantly compared to that of PC concrete. This research can provide a
65 theoretical basis for the service life prediction of BFRP reinforced geopolymer
66 concrete within marine environments.

67 **Keywords:** Geopolymer concrete, Basalt fiber reinforced polymer (BFRP) bars,
68 Seawater, Time-dependence, Interface characteristic.

69

70

71 1 Introduction

72 Geopolymer concrete (GPC) has attracted extensive attention from researchers
73 due to its excellent characteristics, such as stable hydration products, compact paste
74 structure, adjustable setting time, early strength, and high strength [1-4]. Meanwhile, it
75 can effectively reduce energy consumption and greenhouse gas emissions of ordinary
76 Portland cement (OPC) production [5-10]. The process of preparing GPC is given in
77 Fig.1. In addition, GPC has excellent seawater corrosion resistance, enabling the use
78 of local materials and sea sand as aggregate, to solve the problem of insufficient river

79 sand resources. Therefore, GPC is suitable for the characteristics of marine
80 engineering construction, and it can address issues such as the shortage of materials
81 and fresh water, the influence of tidal action in the construction process, and the
82 corrosion from harmful ions in seawater in the service process of buildings.
83 Experimental results show that the mechanical properties of seawater sea sand
84 concrete (SWSSC) are similar to those of traditional concrete^[11]. However, seawater
85 and sea sand contain high concentrations of chloride ions, which will lead to the
86 corrosion of steel bars in SWSSC structures ^[12, 13]. Corrosion and expansion of steel
87 bars cause durability problems such as cracking and peeling of the protective concrete
88 layer. These problems seriously reduce the safety of SWSSC structures and lead to
89 high maintenance costs. However, fiber reinforced polymer (FRP) bars are believed to
90 be another effective way to solve these problems, potentially eliminating the
91 limitation that seawater sea sand cannot be directly used as concrete raw material ^[14].
92 Recently, basalt fiber reinforced polymer (BFRP) bars have been used in some
93 concrete structures subjected to extreme environmental conditions due to their
94 superior chemical resistance ^[15-17]. There is no corrosion and expansion problem in
95 marine environments, so BFRP reinforced geopolymer concrete (hereafter called
96 BFRP GPC) has broad application prospects in marine engineering construction.
97 However, it is worth noting that BFRP GPC has double interface transition zones
98 (ITZs), and the transport of corrosive ions in seawater in the GPC is time-dependent.
99 Existing research results do not reveal the time-dependence variation of corrosive ions
100 transported in GPC under seawater corrosion and the influence of the time-
101 dependence variation on the performance of BFRP bars. Thus, it is necessary to study
102 the time-dependence mechanism of GPC and BFRP bars under seawater corrosion as
103 it can provide a basis for service life prediction of BFRP GPC in marine environments.

104 In previous studies, there have been numerous research efforts on the seawater
105 corrosion resistance of GPC, including Cl^- permeability resistance, sulfate resistance
106 (SO_4^{2-} and Mg^{2+}), and the variation of properties in artificial seawater. On Cl^-
107 permeability resistance of GPC, Thomas et al. ^[18] studied the chloride ion
108 permeability of alkali-activated fly ash, alkali-activated slag, and PC concrete
109 immersed in 3% NaCl for 90 days. In general, alkali-activated slag concrete has better
110 chloride ion permeability resistance, slightly better than PC concrete. Gunasekara et al.
111 ^[19] studied the corrosion of fly ash-based geopolymers and PC concrete immersed in

112 3% NaCl for 540 days. Test results indicated that the three-dimensional N-A-S-H and
113 C-A-S-H crosslinking formed in the fly ash-based geopolymers reduces the diffusion
114 of chloride ions into the depth of the concrete, resulting in a lower corrosion rate
115 compared to PC concrete. Amorim Junior et al. [20] showed that metakaolin GPC has
116 similar or higher durability than OPC concrete by the migration test of chloride.
117 Therefore, GPC has excellent resistance to chloride ion penetration, which is related
118 to the type of activator, alkali content, and curing mode in GPC. In addition, the
119 presence of sulfate ions and magnesium ions can also affect the durability of concrete
120 structures in the marine environment. Krivenko et al. [21] proposed that slag-based
121 geopolymer concrete has better sulfate resistance than PC paste, even better than
122 sulfate-resistant cement pastes, and sodium sulfate is beneficial to promote the
123 polymerization of GPC continuous reaction, making the structure more compact.
124 Dzunuzovic et al. [22] studied the influence of 5% sodium sulfate solution on the
125 mechanical properties and microstructure properties of fly ash-slag base binder (FA-
126 BFS) and PC concrete for 180 days. During the whole immersion period, the strength
127 loss index was higher than 1, and the compressive strength of specimens exposed to
128 the sulfate solution developed slowly. XRD (X-ray diffractometer) analysis shows that
129 there were no new substances produced by the alkali-activated material and sulfate
130 reaction. Sanghamitra Jena [23] used silica ash to partially replace fly ash to prepare
131 GPC. Specimens were respectively immersed in 5% NaCl and 2% MgSO₄ corrosive
132 solution for 28 days. The experimental results showed that adding fly ash and silica
133 fume can improve the strength of GPC. Hafez E. Elyamany et al. [24] compared the
134 corrosion resistance of GP mortar with added slag and silica fume substituted for fly
135 ash, GP mortar with fly ash, and OPC mortar after immersion in 10% MgSO₄ solution
136 for 48 weeks. The results showed that the corrosion resistance of GP mortar mixed
137 with slag and silica fume is higher than that of GP mortar mixed with fly ash only, and
138 both are higher than that of OPC mortar. Valencia Saavedra et al. [25] studied the
139 performance of GPC (composed of 80% fly ash and 20% mineral powder) and OPC
140 concrete after curing in 5% MgSO₄ solution for 360 days. The results showed that the
141 expansion rate of FA/GBFS (Class fly ash and granulated blast-furnace slag) concrete
142 is 0.04% and the mechanical resistance is reduced by 33%, while the expansion rate
143 of OPC concrete is 0.08% and the mechanical resistance is reduced by 48% under the
144 same conditions. Therefore, FA/GBFS concrete has better resistance to MgSO₄

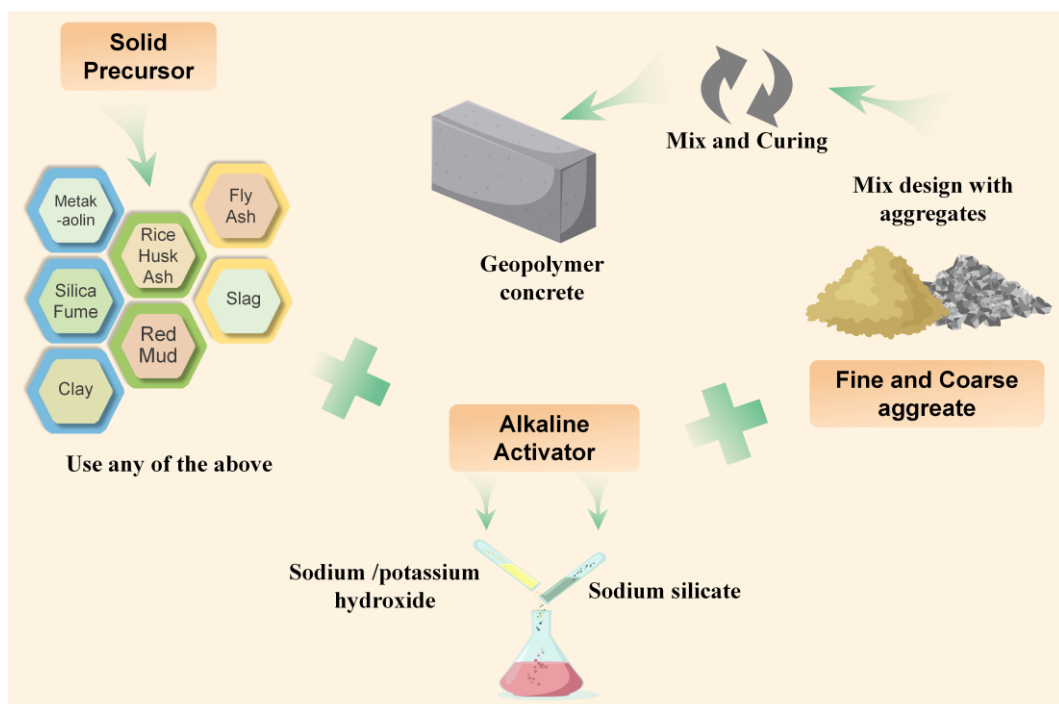
145 corrosion than OPC concrete. The above research shows that all kinds of GPC have
146 better sulfate resistance than OPC concrete, as the reaction products are difficult to
147 corrode and the microstructure is compact. However, existing research on the
148 seawater corrosion resistance of GPC does not consider the time-dependence of
149 corrosive ion transport, and the influence mechanism of the dynamic transport process
150 of corrosive ions in GPC on their macroscopic properties and microstructure evolution
151 has not been determined. In addition, the corrosion resistance of GPC in marine
152 environments is an important problem to understand to enable their successful
153 application [20, 26, 27].

154 Some researchers have studied the corrosion resistance of steel bars in GP
155 mortars and concrete in marine environments [21, 28-32], but few articles have evaluated
156 the long-term performance (such as durability and strength degradation) of BFRP bars.
157 Yan et al. [14] concluded that the tensile strength of BFRP bars in an alkaline concrete
158 pore solution decreases much faster than in distilled water, salt, or acid environments.
159 In addition, they found that the long-term performance degradation of BFRP bars in
160 alkaline solutions was more obvious than in seawater because OH^- broke the Si-O-Si
161 bonds in the basalt fibers [13]. Z. Wang et al. [32] conducted accelerated corrosion tests
162 on BFRP bars under different pH values, immersion temperatures, and durations.
163 Subsequently, they used Arrhenius degradation theory to predict the long-term
164 behavior of BFRP bars under service conditions. The study [33] evaluated the residual
165 tensile properties of BFRP bars coated with different SWSSC thicknesses exposed to
166 tap water, simulated seawater, and alkaline solution at 28°C, 40°C, 60°C. It was found
167 that the alkaline solution has a more harmful effect on the tensile properties of BFRP
168 bars than tap water or seawater. Alkalinity is the key factor leading to the deterioration
169 of BFRP bars. Therefore, thicker SWSSC-coated BFRP bars have higher resistance in
170 alkaline environments, and their tensile strength retention is lower than bare BFRP
171 bars. To sum up, although BFRP bars have an excellent ability to resist chloride
172 corrosion, the high alkaline environment in concrete will deteriorate their performance
173 [33-36]. Therefore, it is important to evaluate the long-term durability of BFRP bars in
174 marine environments. Existing studies have not revealed the time-dependence
175 mechanism of the mechanical properties and microstructure of BFRP under seawater
176 corrosion, so further research work is necessary to establish the strength degradation
177 model of BFRP under seawater corrosion.

178 Many studies^[37-40] have focused on the macroscopic analysis of the bonding
179 properties of BFRP bars and concrete, while less research has been done on the
180 microscopic mechanism of the interface. Furthermore, interface transition zones (ITZs)
181 play a crucial role in BFRP GPC, both between aggregates and pastes and between
182 pastes and BFRP bars. While the ITZ between GP pastes and aggregates is denser
183 than that between OPC pastes and aggregates^[41], it remains a weak area prone to the
184 development of microcracks and is key to controlling the overall strength, chemical
185 corrosion resistance, permeability, and other macro properties of GPC ^[42]. Current
186 research on the ITZ between pastes and aggregates primarily focuses on PC concrete,
187 with limited investigation on GPC. Luo ^[35] compared the performance of ITZs in PC
188 concrete and GPC, finding that the interface bond between the GPC matrix and
189 aggregates is stronger than in PC concrete. In PC concrete, the ITZs contain numerous
190 crystalline hydration products, whereas in GPC, the ITZs consist of a gelate-rich paste
191 with a denser microstructure. Tian et al. ^[43] examined the interface characteristics and
192 mechanical behavior of slag aggregates and GPC, comparing different GPC/steel slag
193 interface systems. They observed that the interface interaction between GPC and steel
194 slag aggregates significantly influenced the interface properties and mechanical
195 behavior. Xin Ren et al. ^[44] conducted comparative experiments to study the bond
196 strength of ITZs between GPC and aggregate, as well as OPC and aggregate. Their
197 experiments suggested that the development of ITZ bond strength in GPC appeared to
198 be more rapid than in OPC concrete after 7 days. In summary, both domestic and
199 international scholars have investigated the microstructure, composition, and bond
200 strength of the ITZ in GPC. However, it should be noted that previous research
201 primarily relied on qualitative analyses, lacking quantitative characterization, and the
202 mechanism of deterioration remains unclear, making it difficult to establish the
203 regulatory influence of ITZ microstructure on mesoscopic and macroscopic properties.
204 Furthermore, the double interface transition zone of BFRP reinforcement geopolymer
205 concrete has not been adequately considered.

206 As a result, the time-dependent strength model of GPC and the tensile strength
207 model of BFRP in marine environments have yet to be established. Additionally, the
208 changes in composition and microstructure of reaction products with GPC when
209 exposed to corrosive ions in seawater environments are not well understood. The
210 mechanism by which corrosive ions affect the properties of double interface transition

211 zones in BFRP GPC has not been confirmed. Consequently, this study aims to
212 investigate the volume and strength loss rates of GPC in a simulated seawater
213 environment during various immersion periods. The migration of corrosive ions (Cl^- ,
214 SO_4^{2-} , Mg^{2+}) in seawater will be evaluated. Simultaneously, the tensile strength of all
215 BFRP bars will be tested after immersion in artificial seawater and alkaline simulated
216 seawater for different durations, considering the effects of GP mortar wrapping on the
217 properties of BFRP bars. The research will analyze the microstructural changes of
218 BFRP bars in artificial seawater environments. Ultimately, this study aims to provide
219 a theoretical basis for predicting the service life of BFRP GPC in marine
220 environments.



221
222 **Fig. 1.** Production of geopolymer concrete
223

224 **2 Experimental Design**

225 **2.1 Materials**

226 The feasibility of utilizing a Geopolymer in marine environments was
227 investigated using a composition comprising 70% granulated blast-furnace slag
228 (GGBFS), 12% fly ash, 5% silica fume, and 13% activator, which consisted of a solid
229 mixture of sodium silicate and sodium carbonate. The composites and chemical
230 composition of the Geopolymer are provided in Table 1 and Table 2 [45]. By

231 considering the results of MgO compensation GPC volume shrinkage, stability, and
 232 mortar strength, it was possible to prepare a Geopolymer with minimal volume
 233 shrinkage (referred to as GII) by incorporating 6% MgO (in a ratio of 60 seconds: 220
 234 seconds = 1:1) into the GPC [45]. This formulation was then used to assess its
 235 suitability for marine environments. The mixture ratio and mechanical properties of
 236 the GPC and PC concrete are presented in Table 3 and Table 4, respectively. The sand
 237 was sourced from Huilai County, Guangdong Province and is natural sea sand. Table
 238 5 provides information on the performance and ion content of the sea sand.
 239 Additionally, Table 6 presents the basic physical properties of limestone gravel. The
 240 BFRP bars were supplied by Sichuan Aerospace Tuoxin Basalt Industry Co., LTD, an
 241 industrial manufacturer. Table 7 displays the initial physical properties of the BFRP
 242 bars.

243 **Table 1.** Composition of Geopolymer (wt%)

Material	Composites				Blaine specific surface area, m ² /kg	Density, g/cm ³	Flexural strength, MPa		Compressive strength, MPa	
	GGBFS	Fly ash	Silica fume	Activator			3 d	28 d	3 d	28 d
Geopolymer	70%	12%	5%	13%	375	2.90	4.5	7.9	30.6	50.2

244 **Table 2** Chemical composition of geopolymer binder /wt%

Composition	SiO ₂	Al ₂ O ₃	Fe ₂ O ₃	TiO ₂	CaO	Mg O	SO ₃	P ₂ O ₅	K ₂ O	Na ₂ O	LOI
Geopolymer	30.5 6	19.56	2.22	0.85	34.40	3.23	1.2 3	0.05	2.09	4.88	0.9 3

245 **Table 3** Mix proportions of geopolymer and Portland cement concretes

Sample ID.	Strengt h grade	W/ C	ρ /%	Binder /(kg/m ³)	Sand /(kg/m ³)	Aggrega te /(kg/m ³)	Superplastictiz er /(kg/m ³)	Water /(kg/m ³)
P-35	C35	0.4 0	42	440	760	1050	7.92	176
GII-35		0.4 0	42	440	720	1000	/	176

246 **Table 4** Physical and mechanical properties of geopolymer and Portland cement
 247 concretes

Sample ID.	Workability		Compressive strength /MPa		
	Slumps/cm	Slump flow/mm	3 days	7 days	28 days
P-35	14.0	170	30.5	38.5	45.0

GII -35 18.0 220 39.6 45.0 56.5

248 **Table 5** Performance of sea sand from Huilai County of Guangdong Province

Fineness modulus	Particle size range	Apparent density/(kg/m ³)	Bulk density/(kg/m ³)	Shell /(wt%)	Cl ⁻ (wt%)	Mg ²⁺ (wt %)	SO ₄ ²⁻ /(wt %)
2.52	II	2590	1520	2.5~3.6	0.1008	0.0098	0.0090

249 **Table 6** Physical properties of aggregate

Percentage of flat-elongated particles /%	Crushin g index/ %	Bulk density/(kg/m ³)	Apparent density/(kg/m ³)	Voidage/%
7.5	9.1	1560	2750	43.3

250 **Table 7** Physical properties of BFRP bars

Type	Length/(mm)	Diameter/(mm)	Tensile strength/(MPa)	Anchorage length/(mm)
BFRP	1000	$\frac{6}{8}$	800~1100	400

251

252 **2.2 Exposure condition**

253 In this study, two immersion environments were employed for testing purposes.
 254 The GPC specimens were immersed in tap water, while the bare BFRP bars were
 255 immersed in artificial seawater. The composition of the artificial seawater solution
 256 was designed based on ASTM D 1141-98 and is outlined in Table 8. Considering the
 257 alkaline nature of the concrete environment, the BFRP bars were additionally
 258 immersed in alkaline simulated seawater. This simulated seawater was prepared using
 259 a saturated Ca(OH)₂ solution, following the composition specified in Table 8. To
 260 facilitate comparative analysis, BFRP bars coated with GP mortar were also immersed
 261 in artificial seawater. The exposure periods for all specimens were 28 days, 56 days,
 262 90 days, 180 days, and 360 days.

263 **Table 8** The composition of artificial seawater

Ion types	NaCl	MgCl ₂	Na ₂ SO ₄	CaCl ₂
Concentration (g/L)	4.53	20	4.09	1.16

264 3 Test methods

265 3.1 Seawater resistance of geopolymer concrete

266 3.1.1 Volume expansion and strength loss of geopolymer concrete

267 The specimens were prepared according to the mix proportions specified in Table
268 3. They were cast in the form of 150×150×150 mm blocks and cured at room
269 temperature for 24 hours. After demolding, the specimens were transferred to a
270 standard curing chamber maintained at a temperature of 25 °C and a relative humidity
271 of 95% for a period of 28 days.

272 Following the curing period, any loosely adhering portions at the corners of the
273 test blocks were removed, and the resulting volume was measured using the drainage
274 method. This initial volume measurement was recorded as the original volume of the
275 specimens.

276 During the immersion and corrosion period, the volume and compressive
277 strength of the specimens were measured after a certain duration denoted as "t" days.
278 The V_t (volume corrosion resistance coefficient) and S_t (strength corrosion resistance
279 coefficient) were utilized to characterize the seawater corrosion resistance of the
280 concrete. The physical meanings of these parameters are as follows:

$$281 \quad V_t = \frac{v_t - v_{28}}{v_{28}} \quad (1)$$

282 Where, V_t is coefficient of the volume corrosion resistance at time, t ; v_t is the volume
283 of the concrete specimens at t age (mm^3); v_{28} is the volume of the concrete specimens
284 at 28 days (mm^3).

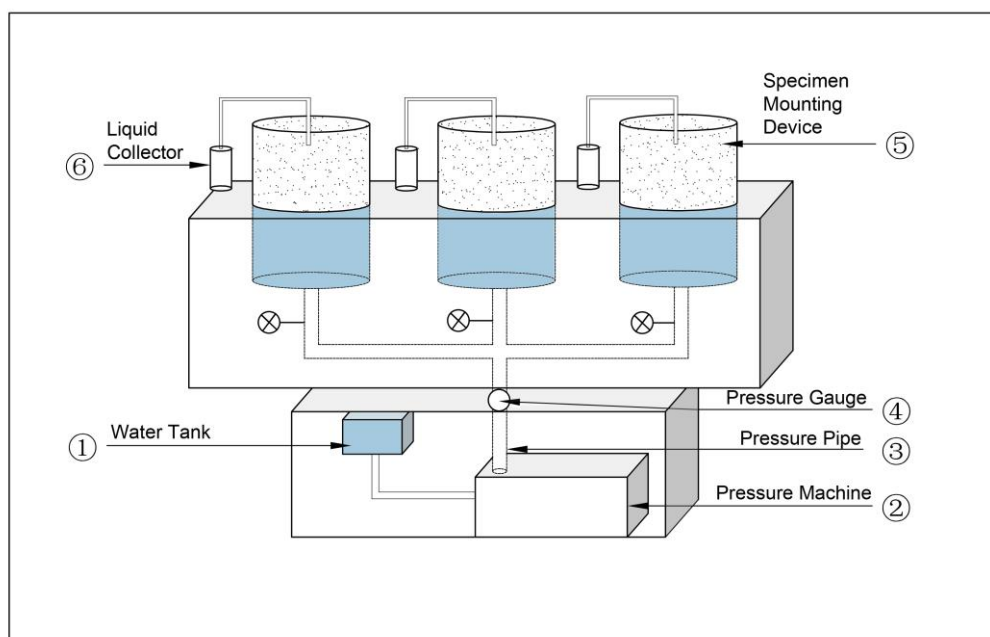
$$285 \quad S_t = \frac{s_{28} - s_t}{s_{28}} \quad (2)$$

286 Where, S_t is coefficient of the strength corrosion resistance at time, t ; s_t is the
287 compressive strength of the concrete specimens at t age (MPa); s_{28} is the compressive
288 strength of the concrete specimens at 28 days (MPa).

289 3.1.2 Ion migration resistance of geopolymer mortar

290 In order to further investigate the transport performance of corrosive ions in GP
291 mortar, a mortar mixture was prepared by incorporating artificial seawater containing
292 corrosive ions such as Cl^- , Mg^{2+} , and SO_4^{2-} . Once the mortar reached a specific age,

293 ion content measurements were conducted in each layer of the mortar along the
 294 direction of hydrostatic pressure. These measurements were used to calculate the
 295 migration coefficient of the GP mortar. For the ion migration tests, a self-made ion
 296 migration testing device was utilized, as depicted in Figure 2. The device includes a
 297 water tank ①, which is connected to an air compressor ② through a pipe. The valve is
 298 set on the pipeline, the air pressure machine ② is connected to the specimen
 299 mounting device ⑤ through the pressure pipe ③. The pressure gauge ④ is set on the
 300 pressure pipe ③, and the specimen mounting device ⑤ is installed with an osmotic
 301 liquid collector ⑥ on the upper part of the specimen mounting device. After migrating
 302 for a certain period of time, the liquid in the collector ⑥ is poured into a measuring
 303 cylinder to measure its volume, and the ion concentration in the liquid is measured by
 304 ion chromatography to calculate the amount of ions migrating for a certain period of
 305 time. Cylindrical mortar specimens with a bottom diameter of 100 mm, top diameter
 306 of 80 mm, and height of 100 mm were employed as migration specimens. The
 307 cement-to-sand ratio was 1:3, and the water-to-cement ratio was 0.5. After curing for
 308 28 days, the specimens were subjected to testing under standard conditions with a
 309 relative humidity (RH) of at least 95% and a temperature of $20\pm 2^{\circ}\text{C}$.



310
 311
 312

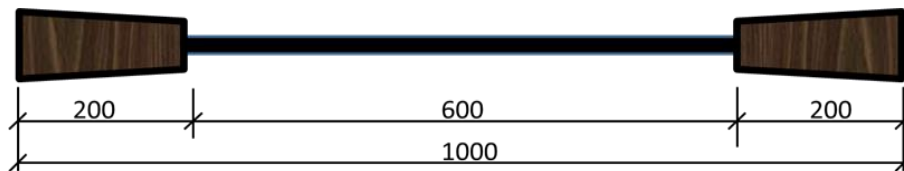
Fig. 2. The schematic diagram of device for testing ion migration in mortar specimens

313 3.2 Tensile performance of BFRP bars

314 After being immersed in tap water, artificial seawater, and alkaline simulated
315 seawater (saturated with a $\text{Ca}(\text{OH})_2$ artificial seawater solution), the BFRP bars were
316 removed and the surfaces were dried. The tensile specimens of the BFRP bars were
317 designed and manufactured following the guidelines outlined in ACI440.3R-04
318 "Guide to Test Methods for FRP Bars Reinforced Concrete Structures". The total
319 length of the tensile specimen, denoted as "L," was set to 1000 mm.

320 To prevent shear damage caused by the tensile machine fixture, adhesive anchors
321 were incorporated at both ends of the tensile test sample within a length of 200 mm,
322 as depicted in Fig. 3. These anchors were constructed using galvanized steel pipes
323 with a bottom diameter of 30 mm, top diameter of 35 mm, and thickness of 3 mm.
324 The steel sleeves were bonded to the BFRP bars by pouring epoxy resin.

325 Following the specifications outlined in the "Test Method for Basic Mechanical
326 Properties of Fiber Reinforced Composite Bars" (GB/T 30022-2013), the prepared
327 BFRP bars were subjected to a tensile test using an electro-hydraulic servo universal
328 testing machine. This test aimed to measure the ultimate tensile strength and tensile
329 strain of the specimens. A displacement control method was employed to ensure that
330 the specimens were destroyed within a timeframe of 1 to 10 minutes.



331

332 **Fig. 3.** BFRP specimen for tension test (mm)

333 3.3 Microscopic analysis

334 The microstructural tests conducted in this study included scanning electron
335 microscopy (SEM), mercury intrusion porosimetry (MIP), and backscattering electron
336 (BSE) imaging. To investigate the impact of marine corrosive substances on the
337 microstructure of GPC, different dosages of NaCl , Na_2SO_4 , and MgSO_4 were added
338 into the GP paste, as detailed in Table 9. The MIP method was employed to examine
339 the pore structure characteristics of GPC after 28 days of exposure to corrosive
340 substances. The microstructure of the BFRP bars was analyzed using SEM after 180

341 days of immersion in tap water, artificial seawater, and alkaline simulated seawater
 342 (saturated with a $\text{Ca}(\text{OH})_2$ artificial seawater solution).

343 **Table 9** Dosage of corrosion ions in geopolymer

Groups	Dosage of corrosion ions (%)								
	NaCl			Na ₂ SO ₄			MgSO ₄		
1	0	3.5	5	-	-	-	-	-	-
2	-	-	-	0	3	8	-	-	-
3	-	-	-	-	-	-	0	3	8

344 3.3.1 Scanning electron microscopy (SEM) tests

345 The hardened paste samples were fractured into pieces after being cured for a
 346 specific duration, and some of these fragments underwent gold-plating treatment. The
 347 BFRP bars were immersed in tap water, artificial seawater, and alkaline simulated
 348 seawater (saturated with a $\text{Ca}(\text{OH})_2$ artificial seawater solution) until reaching a
 349 predetermined age. Subsequently, the bars were taken out and the surfaces were dried.
 350 The microstructures of these samples were analyzed using EVO18 scanning electron
 351 microscopy (SEM) equipment, manufactured by Carl Zeiss Germany.

352 3.3.2 Mercury Intrusion Porosimetry (MIP) tests

353 MIP was employed to assess the total porosity and pore size distribution of the
 354 mortars. The samples were crushed into small pieces measuring 5×5×5 mm and
 355 soaked in ethanol for over 24 hours, with a volume ratio of approximately 1:4 for the
 356 sample to ethanol. The pore structure of the hardened paste was determined using an
 357 AutoPore IV 9500 mercury porosimeter.

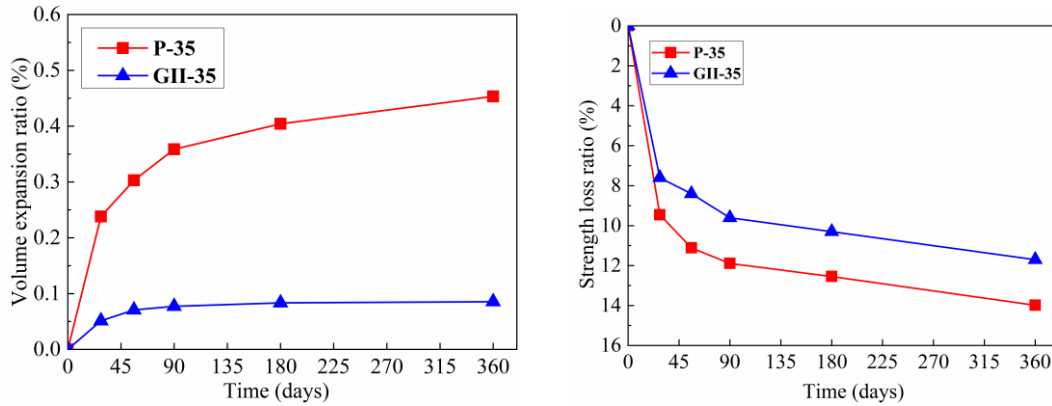
358 3.3.3 Backscattering electron (BSE) tests

359 The samples were analyzed using backscattered electron imaging with an S-
 360 3400N Scanning Electron Microscope. The sample preparation process is as follows:
 361 Initially, the fractured samples were immersed in epoxy resin and left to demold for
 362 24 hours. Subsequently, the samples solidified with epoxy resin were polished using
 363 an automatic Polish-grinding machine, employing sandpapers of various mesh sizes
 364 including 60, 120, 320, 500, 2000, and 4000. Prior to testing, the samples were coated
 365 with a layer of gold to enhance conductivity.

366 **4 Result and discussion**

367 **4.1 Time-Dependent Behavior of Geopolymer Concrete: Volume and Strength**

368 Figure 4 illustrates the seawater resistance of GPC (GII-35) and PC concrete (P-35) over an exposure period of up to 360 days. It can be observed that, compared to
 369 PC concrete, GPC exhibited a significantly lower volume expansion ratio at 180 and
 370 360 days, with increases of 384.6% and 430.0% respectively (Figure 4a). Similarly,
 371 the strength loss ratio of PC concrete at 180 and 360 days increased by 10.4% and
 372 9.6% respectively (Figure 4b). Conversely, GPC demonstrated a remarkable reduction
 373 in both volume expansion ratio and strength loss ratio, which decreased by 77.6% and
 374 8.7% respectively after 360 days of seawater corrosion. These results indicate that
 375 GPC exhibits superior resistance to seawater corrosion compared to PC concrete.
 376



377 (a) Volume expansion
 378 (b) Strength loss

379 **Fig. 4.** The corrosion resistance of GPC and PC concretes

380 **4.2 Time-dependent strength model of GPC in marine environments**

381 Concrete strength will change with service time under the influence of
 382 environmental factors and sustained loads. Based on the strength data of long-term
 383 concrete in actual marine engineering, scholars have analyzed its degradation pattern
 384 using regression methods and proposed a time-dependent decay model for the average
 385 strength of concrete in marine environments, as presented in Eq. (3).

$$f_c(t) = f_0 \times 1.248e^{-0.0340 \times (\ln t - 0.3468)^2} \quad (3)$$

387 Where $f_c(t)$ represents the compressive strength of concrete after t years, MPa; f_0
 388 represents the average value of initial concrete strength, MPa.

389 The time-dependence equation of concrete strength retention rate in marine

390 environments can be determined by Eq.(4). $F_c(t)$ is strength retention rate of concrete
 391 in marine environments in immersion time t .

$$392 \quad F_c(t) = \frac{f_c(t)}{f_0} = 1.248e^{-0.0340 \times (\text{Int}-0.3468)^2} \times 100\% \quad (4)$$

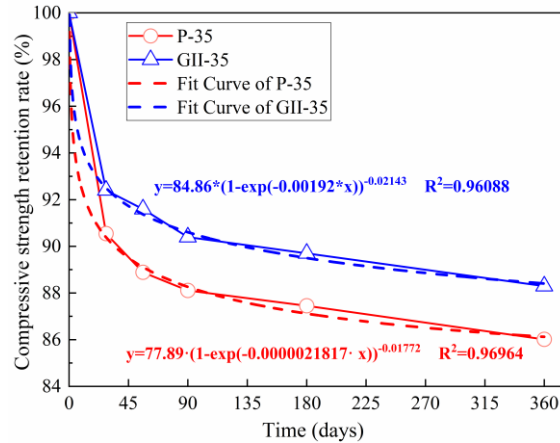
393 In Fig. 5, the fitting curve illustrates the seawater corrosion resistance test results
 394 of GPC (GII-35) and PC concrete (P-35). As time approaches infinity, the strength
 395 retention rate of GII-35 and P-35 reaches 84.9% and 77.9%, respectively. Thus, the
 396 time-dependent degradation equation for the strength retention rate of GPC in marine
 397 environments can be expressed as Eq. (5). $F_w(t)$ is strength retention rate of GPC in
 398 marine environments in immersion time t

$$399 \quad F_w(t) = \frac{84.9}{77.9} \times F_c(t) = 1.360e^{-0.0340 \times (\text{Int}-0.3468)^2} \times 100\% \quad (5)$$

400 The decay equation for the mechanical properties of GPC in marine
 401 environments can be expressed as Eq. (6).

$$402 \quad f_w(t) = f_{w0} \times 1.248e^{-0.0340 \times (\text{Int}-0.3468)^2} \quad (6)$$

403 Where $f_w(t)$ is the compressive strength of GPC after t years, MPa; f_{w0} is the average
 404 initial strength of GPC, MPa.



405
 406 **Fig.5.** Compressive strength of PC (P-35) and GPC (GII-35) in seawater for different
 407 immersion periods

408 4.3 Transport performance of ions in seawater in GP mortar

409 Under the hydrostatic pressure (1.4 MPa), the water samples of mortar specimens
 410 (mixed with artificial seawater) at different exposure ages were analyzed. By
 411 measuring the contents of Cl^- , SO_4^{2-} and Mg^{2+} in the water samples, the amount of
 412 ions permeation migration ΣA_n at different ages were obtained. Based on the ratio of

413 chemical bonding and physical adsorption, A_0 was calculated and $\Sigma A_n/A_0$ was obtained.
 414 The cumulative leaching fraction of ions can be calculated using Eq. (7). The leaching
 415 rate and cumulative leaching fraction of PC mortar and GP mortar were obtained, as
 416 shown in Table 10 and Table 11.

$$417 \quad P_t = \frac{\Sigma A(t)}{A_0} \times \frac{V}{S} \quad (7)$$

418 Where P_t is the cumulative leaching fraction of ions, cm; t is exposure time; $\Sigma A(t)$ is
 419 the accumulated leaching amount of the first n ions, g; A_0 is the amounts of ions that
 420 can migrate in the sample, g; V is the volume of sample, cm^3 ; S is the geometrical area
 421 of the solidified sample in contact with water, cm^2 .

422 **Table 10** Leaching ratio and cumulative leaching fraction of ions from Portland
 423 cement mortar

Time (d)	$\frac{\Sigma A_n}{A_0}$ (Cl^-)	P_t (Cl^-/cm)	$\frac{\Sigma A_n}{A_0}$ (SO_4^{2-})	P_t ($\text{SO}_4^{2-}/\text{cm}$)	$\frac{\Sigma A_n}{A_0}$ (Mg^{2+})	P_t (Mg^{2+}/cm)
1	0.0138	0.1168	0.0050	0.1111	0.0131	0.1161
2	0.0966	0.8178	0.0190	0.4222	0.0291	0.2589
3	0.1494	1.2648	0.0305	0.6778	0.0852	0.7572
5	0.2691	2.2781	0.0455	1.0111	0.1073	0.9541
7	0.3207	2.7149	0.0665	1.4778	0.1984	1.7639
10	0.3981	3.3702	0.1050	2.3333	0.2306	2.0500
15	0.4672	3.9551	0.1567	3.4811	0.2909	2.5861
20	0.5463	4.6248	0.1792	3.9822	0.3853	3.4244
25	0.5953	5.0396	0.2005	4.4556	0.4206	3.7383
30	0.6244	5.2859	0.2250	5.0000	0.4809	4.2744
35	0.6534	5.5314	0.2475	5.5000	0.5902	5.2461
40	0.6625	5.6085	0.2517	5.5933	0.6605	5.8711
50	0.6806	5.7617	0.2681	5.9567	0.7511	6.6767
60	0.7288	6.1697	0.2700	6.0000	0.8408	7.4733

424 **Table 11** Leaching ratio and cumulative percentage of ions from geopolymer mortar

Time (d)	$\Sigma A_n/A_0$ (Cl^-)	P_t (Cl^-/cm)	$\Sigma A_n/A_0$ (SO_4^{2-})	P_t ($\text{SO}_4^{2-}/\text{cm}$)	$\Sigma A_n/A_0$ (Mg^{2+})	P_t (Mg^{2+}/cm)
1	0.0066	0.0512	0.0060	0.0636	0.0030	0.8830
2	0.0593	0.4572	0.0350	0.3719	0.0068	2.0000
3	0.0879	0.6781	0.0455	0.4833	0.0101	2.9415
5	0.1182	0.9117	0.0864	0.9190	0.0165	4.8246
7	0.1507	1.1622	0.1136	1.2083	0.0219	6.4152
10	0.1984	1.5303	0.1353	1.4385	0.0340	9.9415

15	0.2585	1.9932	0.1943	2.0659	0.0473	13.8304
20	0.3029	2.3358	0.2173	2.3099	0.0664	19.4152
25	0.3661	2.8234	0.2472	2.6279	0.0815	23.8304
30	0.4094	3.1567	0.2746	2.9196	0.1006	29.4152
35	0.4426	3.4130	0.2900	3.0837	0.1157	33.8304
40	0.4858	3.7463	0.3009	3.1998	0.1328	38.8304
50	0.5123	3.9503	0.3105	3.3019	0.1670	48.8304
60	0.5387	4.1542	0.3192	3.3937	0.2012	58.8304

425 The following hypotheses are proposed for ion migration in the solidified sample:

426 1) The leaching process of the three ions occurs through one-dimensional leaching
427 along the diameter of the solidified sample; 2) The hardened paste is a homogeneous
428 system; 3) The diffusion coefficient is constant; 4) The permeable water is a
429 homogeneous semi-infinite medium; 5) Ions bound by chemical bonding or physical
430 adsorption remain stable during osmotic dissolution; 6) Hardened pastes will not be
431 damaged by corrosion. According to Fick's 2nd law, the equation for ion osmosis
432 migration and diffusion can be obtained. C_0 is the chloride concentration on the
433 exposed surface of concrete. C is the free chloride concentration in diffusion time t .

$$434 \quad \frac{C}{C_0} = \operatorname{erf}\left(\frac{x}{2\sqrt{Dt}}\right) \quad (8)$$

435 The amount of ions penetration and migration in a solidified sample can be
436 obtained by Fick's 1st law:

$$437 \quad J(t) = -D \frac{\partial C}{\partial x} \Big|_{x=0} = -C_0 \sqrt{\frac{D}{\pi t}} \quad (9)$$

438 The amount of ions migration in a solidified sample per unit area at t migration
439 period can be expressed as:

$$440 \quad A_n(t) = \int_0^t J(t) dt = 2A_0 \sqrt{\frac{Dt}{\pi}} \quad (10)$$

441 Where A_n is the accumulated amount of ions dissolved in t migration period, g; A_0 is
442 the initial amount of transferable ions in the solidified sample, g; D is the surface
443 migration coefficient, mm^2/s .

444 According to the above equations and the cumulative migration fraction, P_t , of
445 the ions in the solidified sample, Eq.(11) can be obtained:

$$446 \quad \frac{\Sigma A_n}{A_0} = 2\left(\frac{S}{V}\right) \sqrt{\frac{Dt}{\pi}} \quad (11)$$

447 Where ΣA_n is the cumulative dissolution amount of ions in t migration period, g; A_0 is

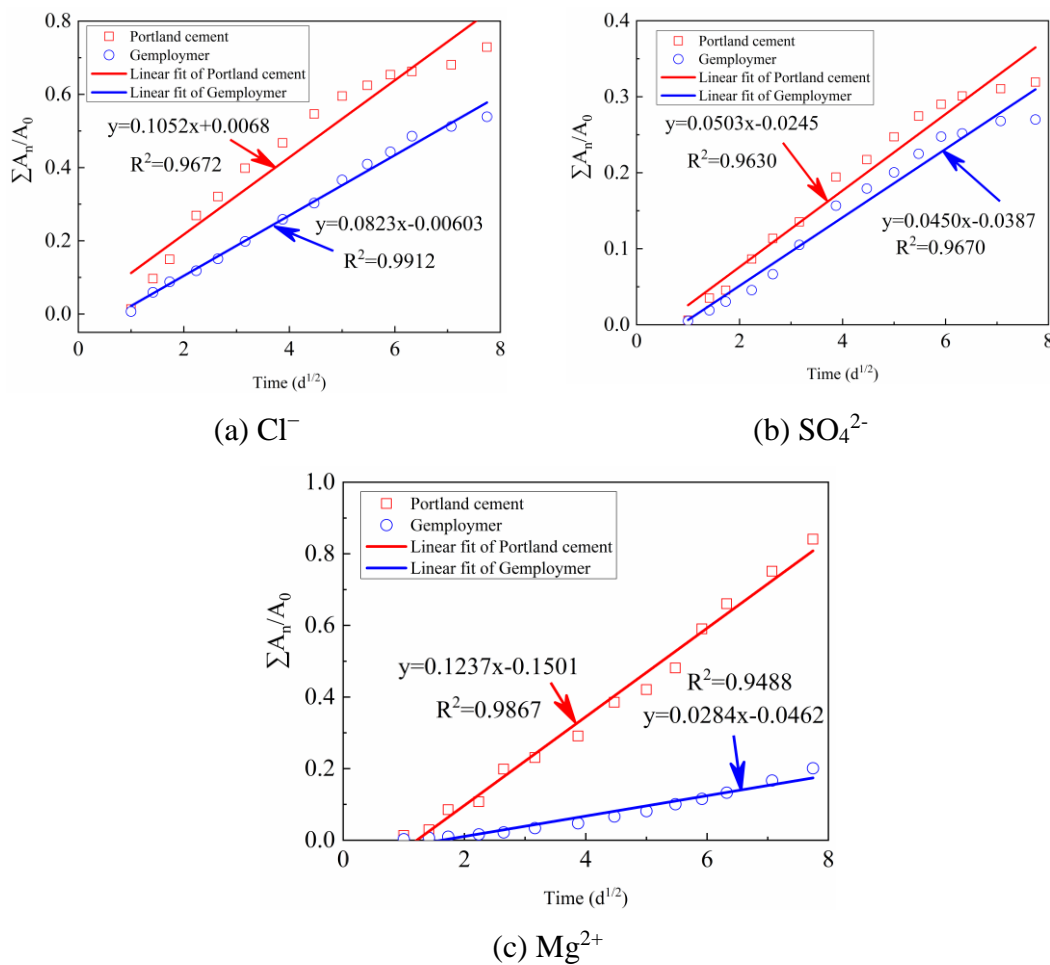
448 the initial amount of transferable ions in the solidified sample, g ; D is the permeability
 449 diffusion coefficient of ions migration, cm^2/d .

450 The migration diffusion coefficient, D , can be obtained from the slope of the line
 451 formed by $\Sigma A_n/A_0$ and $t_n^{1/2}$:

$$452 \quad D = \pi \left(\frac{mV}{2S} \right)^2 \quad (12)$$

453 The cumulative leaching rate ($\Sigma A_n/A_0$) of Cl^- , SO_4^{2-} and Mg^{2+} in the PC mortar and
 454 GP mortar solidified samples obtained by the test is shown in Table 10 and Table 11.

455 The result obtained by curve fitting and $t^{1/2}$ is shown in Fig 6.



456

457

458

Fig. 6. Relationship between $\Sigma A_n/A_0$ and $t_n^{1/2}$

459 According to the fitting results in Fig. 6, the ions diffusion coefficient D of GP
 460 and PC mortar in seawater can be calculated by Eq. (12). Table 12 shows that the
 461 chloride diffusion coefficient of GP mortar is only $6.15 \times 10^{-4} \text{ mm}^2/\text{s}$, which is 61.2%
 462 of that of PC mortar. The sulphate diffusion coefficient of GP mortar is about 1.84×10^{-4}
 463 mm^2/s , which is 81.1% of that of PC mortar. The Magnesium ion diffusion

464 coefficient of GP mortar is $0.73 \times 10^{-4} \text{ mm}^2/\text{s}$, which is only 5.3% of that of PC mortar.
 465 In other words, GP shows excellent performance to resist ions migration.

466 **Table 12** Diffusion coefficient of Cl^- , SO_4^{2-} and Mg^{2+} in GP mortar and PC mortar

Material type	D (Cl^-) / ($\times 10^{-4} \text{ mm}^2/\text{s}$)	D (SO_4^{2-}) / ($\times 10^{-4} \text{ mm}^2/\text{s}$)	D (Mg^{2+}) / ($\times 10^{-4} \text{ mm}^2/\text{s}$)
GP mortar	6.15	1.84	0.73
PC mortar	10.06	2.30	1.39

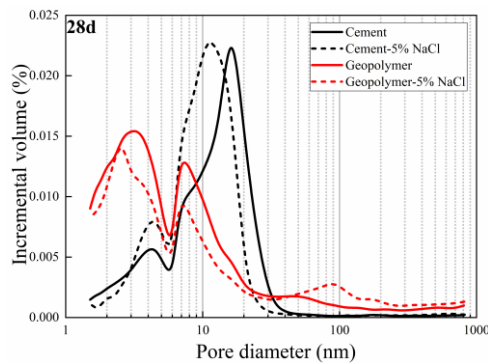
467 4.4 Effect of corrosive ions on pore structure of GP pastes

468 The pore size distributions of cement paste and geopolymer paste with a 28-day
 469 curing age were measured using MIP. The influence of NaCl , Na_2SO_4 , and MgSO_4 on
 470 pore distribution is presented in Fig. 7. The results demonstrate that the pore size and
 471 total porosity of the geopolymer are much smaller than those of the cement. In the
 472 geopolymer pastes, the pore size after 28 days of age is typically smaller than 20 nm.

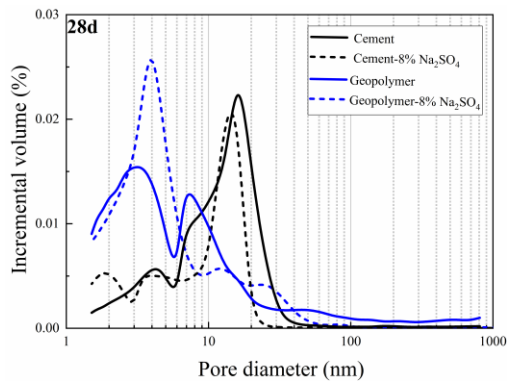
473 Fig. 7(a) shows that the introduction of 5% NaCl has a minimal effect on the
 474 total porosity of the cement paste but refines the pore size. On the other hand, the pore
 475 size of the geopolymer pastes remains relatively unchanged, but the total porosity
 476 decreases significantly with the introduction of 5% NaCl . When considering the initial
 477 and final setting times of the geopolymer pastes, it can be observed that the
 478 introduction of 5% Cl^- delays the reaction speed and increases the reaction degree,
 479 resulting in a decrease in total porosity.

480 Fig. 7(b) and Fig. 7(c) demonstrate that the median pore size of the geopolymer
 481 paste increases with the addition of 8% SO_4^{2-} , while the median pore size of the
 482 cement paste decreases. It is worth noting that the results indicate a decreasing trend
 483 in the number of large pores in the geopolymer paste with the addition of SO_4^{2-} , while
 484 the number of small pores increases significantly. The observed phenomena can be
 485 attributed to the early-stage erosion process, where the erosion products of SO_4^{2-} tend
 486 to initially fill the pores, resulting in a reduction of the median pore size in the cement
 487 paste. Furthermore, the introduction of 8% Mg^{2+} causes a notable increase in the
 488 number of macropores in the cement paste, while simultaneously leading to a
 489 significant decrease in the percentage of macropores in the geopolymer. This
 490 observation suggests that Mg^{2+} erosion converts the hydration product C-S-H gel into
 491 M-S-H, leading to the formation of loosely structured macropores. As a consequence

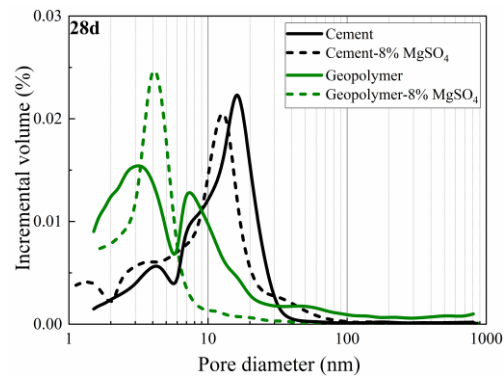
492 of these findings, it can be inferred that geopolymers exhibit favorable resistance to
 493 the penetration of erosive materials, which can be attributed to their compact pore
 494 structure.



(a) Pastes with NaCl



(b) Pastes with Na₂SO₄



(c) Pastes with MgSO₄

495 **Fig.7.** Pore size distribution of geopolymer and cement pastes with NaCl, Na₂SO₄ and
 496 MgSO₄

497 **4.5 Time-dependence regulation of mechanical properties of BFRP bars in**
 498 **seawater**

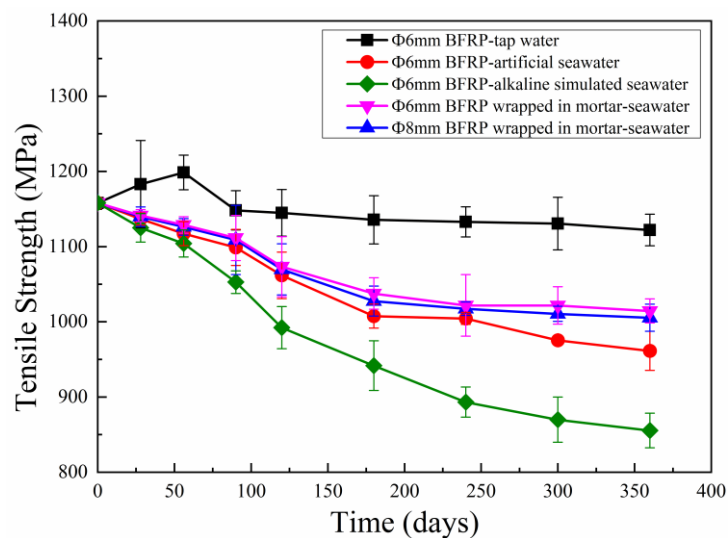
499 Fig. 8 illustrates the degradation of tensile strength for bare BFRP bars with
 500 diameters of Φ 6mm and Φ 8mm when immersed in different media (tap water,
 501 artificial seawater, and alkaline simulated seawater). It also shows the degradation of
 502 BFRP bars with a diameter of Φ 6mm that were wrapped in mortar and immersed in
 503 artificial seawater for varying periods of time. In all solutions, the tensile strengths of
 504 BFRP bars initially decrease rapidly and then exhibit a slower decrease as the
 505 exposure period increases.

506 One possible explanation for this phenomenon is that the corrosion medium
 507 reaches equilibrium after diffusing to a certain depth within the BFRP bars, causing

508 the corrosion reaction to slow down due to the accumulation of reaction products.
 509 Notably, the degradation is significantly accelerated in alkaline environments. The
 510 trend of tensile strength retention for BFRP bars under the same conditions follows
 511 this order: tap water immersion > artificial seawater immersion > alkaline seawater
 512 immersion.

513 It is important to mention that the tensile strength degradation of BFRP bars
 514 wrapped in mortar and immersed in seawater for 360 days was found to be 6%
 515 stronger compared to bare BFRP bars. Additionally, when comparing the tensile
 516 strength of Φ 6mm and Φ 8mm BFRP bars wrapped in mortar, it is observed that the
 517 degradation of tensile strength is more pronounced in the larger diameter bars.

518



519

520 **Fig.8.** Variation of tensile strength of BFRP bars in different corrosive solutions

520

521 **4.6 Microstructure of BFRP bars in seawater**

522 Fig. 9 presents SEM images of the cross section of Φ 6mm BFRP bars immersed
 523 in different media for a period of 180 days. In Fig. 9(a), which represents immersion
 524 in tap water, it is evident that a significant amount of resin remains bonded to the
 525 surface of the fibers. This bonding facilitates the formation of tight bundles as the
 526 fibers combine with each other.

527

528 In Fig. 9(b), corresponding to immersion in artificial seawater, the outer fibers
 529 display the presence of pores at the edge of the cross-section, and the surface structure

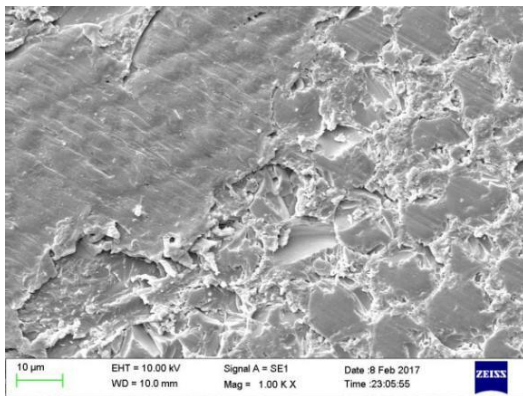
530 appears to have loosened due to corrosion.

531

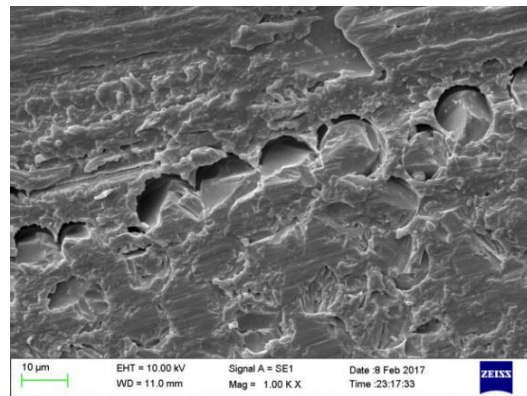
532 Fig. 9(c) illustrates the cross section of BFRP bars after immersion in alkaline
533 simulated seawater. The damage process is visibly pronounced, characterized by fiber
534 ruptures, resin degradation, and debonding of the resin-fiber interface. This results in
535 an increased loose area and noticeable protrusion of fibers.

536

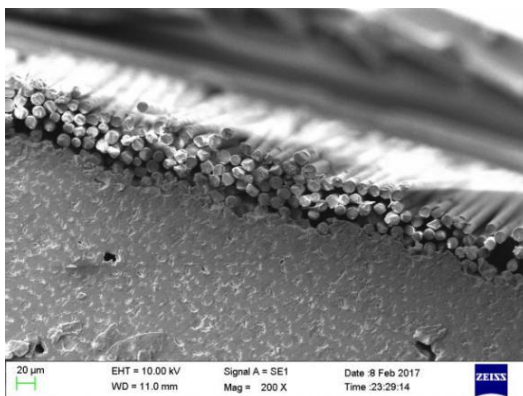
537 These SEM images provide insight into the changes and damage experienced by
538 the BFRP bars under different immersion conditions, highlighting the effects of
539 various media on the surface and structural integrity of the bars.



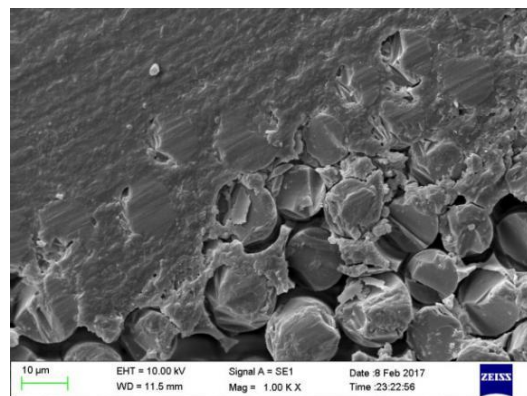
(a) BFRP bar immersed in water



(b) BFRP bar immersed in artificial seawater



(c) BFRP bar immersed in saturated Ca(OH)₂ seawater



540 **Fig.9.** Microstructure of cross section of BFRP bars after 180 days corrosion

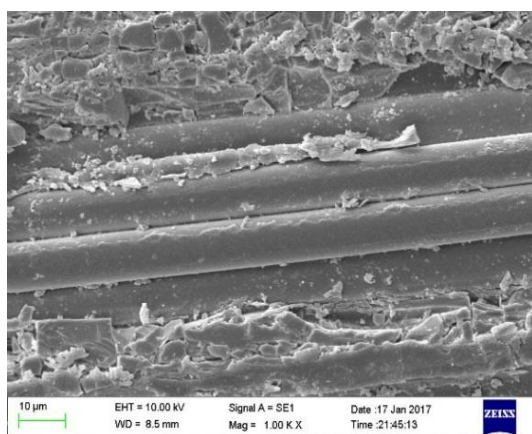
541 Fig. 10 displays SEM micrographs of the longitudinal section of Φ 6mm BFRP

542 bars subjected to different immersion media for a duration of 180 days. In Fig. 10(a),
543 representing immersion in tap water, the surface of the fiber and resin remains
544 unchanged. The fiber maintains a smooth and flat appearance, tightly connected to the
545 resin.

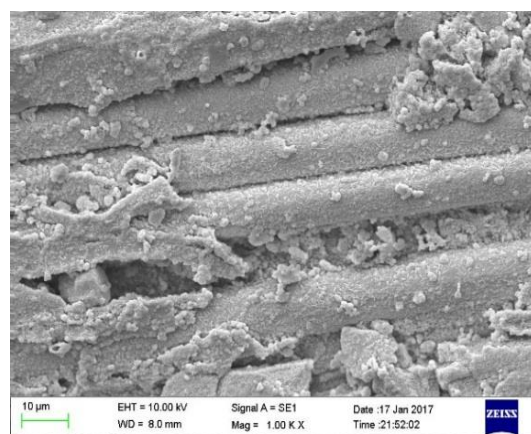
546 In Fig. 10(b), following immersion in seawater, the intermediate resin that
547 bonded the fibers together disappears, leading to a further loosening of the fiber
548 bundles. Additionally, a significant amount of salt crystals can be observed attached
549 to the surface.

550 Fig. 10(c) reveals that after immersion in alkaline simulated seawater, very little
551 resin remains bonded to the fiber surface. The fibers exhibit evident corrosion, with
552 signs of detachment and noticeable damage defects. This phenomenon can be
553 attributed to the gradual penetration of the corrosive medium along the radial
554 direction of the bars. Initially, the shedding of fiber and resin occurs, followed by
555 fiber surface corrosion in the later stages. These factors contribute to a significant
556 decrease in the tensile strength of the BFRP bars.

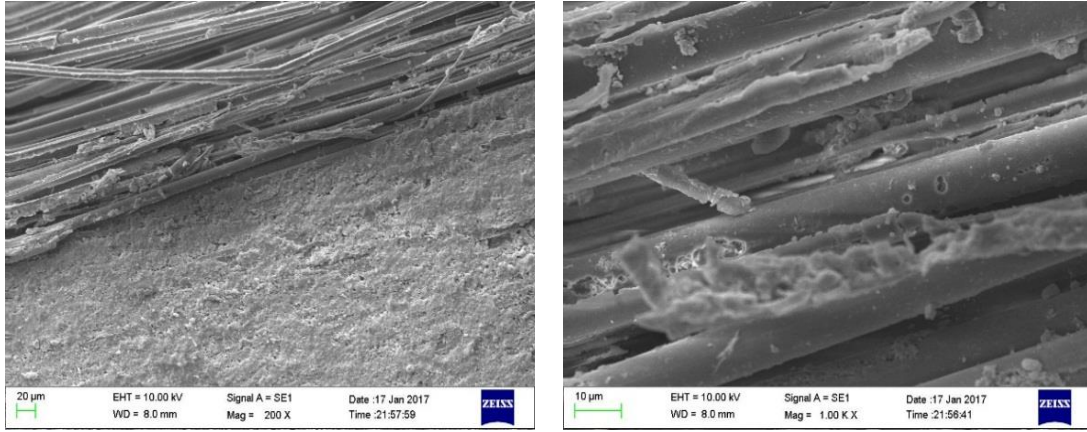
557 The observations presented in Fig. 10, along with those in Fig. 9, demonstrate
558 the decisive influence of alkaline environments on the degradation of tensile strength
559 in BFRP bars. This finding aligns with the results obtained from the tensile strength
560 tests.



(a) BFRP bar immersed in water



(b) BFRP bar immersed in artificial seawater



(c) BFRP bar immersed in saturated Ca(OH)_2 seawater

561 **Fig.10.** Microstructure of vertical section of BFRP bars after 180d corrosion

562 **4.7 Degradation model of tensile strength of BFRP bars in marine environments**

563 Through microscopic analysis of BFRP bars, the degradation mechanism in a
 564 seawater environment is identified as fiber-resin matrix interface split and separated
 565 failure. This mechanism can be expressed as follows [46]:

566
$$f_f = (100 - Y_\infty) \exp\left(-\frac{t}{\tau}\right) + Y_\infty \quad (13)$$

567 Where, Y_∞ is the residual tensile strength of BFRP bars when the corrosion time tends
 568 to infinity; τ is the characteristic time determined by corrosion temperature.

569 The corrosion of BFRP bars that are wrapped in GPC in marine environments is
 570 primarily caused by seawater corrosion and the alkaline environment within the GPC.
 571 Therefore, Eq (13) is modified as follows:

572
$$f_f = Y_\infty \times \exp(-b \times t)^c + Y_\infty \quad (14)$$

573 To verify the modified Eq. (14), the time-dependent variation of tensile
 574 properties of Φ 6 mm and Φ 8 mm BFRP bars wrapped in GP mortar under seawater
 575 immersion is fitted, as shown in Fig. 11. The fitting parameters are presented in Table
 576 13. In the seawater environment, the final strengths of Φ 6 mm and Φ 8 mm BFRP
 577 bars are 695 MPa and 663 MPa, respectively. The established tensile strength
 578 degradation models for the BFRP bars are as follows:

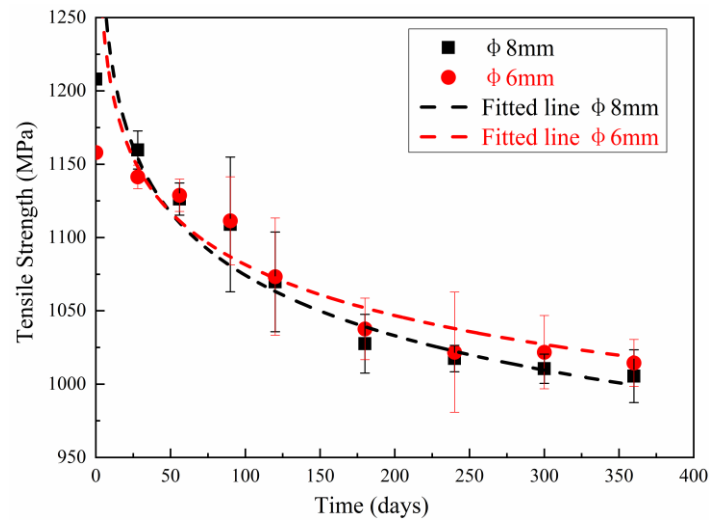
579 Φ 6 mm BFRP bar:

580
$$f_f = 695.38 \times (1 - \exp(-8.19958E - 7 \times t))^{-0.04694} \quad (15)$$

581 Φ 8 mm BFRP bar:

582

$$f_f = 663.76 \times (1 - \exp(-1.98349E - 6 \times t))^{-0.04248} \quad (16)$$



583

584

Fig.11. Tensile strength of BFRP immersed in a marine environment

585

Table 13 Parameters of the fitting equation to describe the degradation of BFRP bars

	Φ6 mm	Φ8 mm
Y_{∞}	695.38	663.76
b	8.19958E-7	1.98349E-6
c	-0.04694	-0.04248
R^2	0.92197	0.95115

586

4.8 Microstructure characteristics of the interface of BFRP bars reinforced

587

geopolymer in seawater

588

4.8.1 Microscopic properties of the interface between geopolymer and aggregate in

589

seawater

590

The microscopic morphology of hardened samples of GPC and PC concrete after

591

immersion in tap water and artificial seawater for 360 days is depicted in Fig. 12 and

592

13. The backscattered electron (BSE) images of the hardened samples reveal certain

593

characteristics. The brightly colored irregular blocks represent unreacted clinker or

594

slag, while the brightly colored globular particles indicate unreacted fly ash. The gray

595

areas correspond to the reaction products formed during the reaction, and the black

596

areas represent pores within the hardened samples.

597

Fig. 12(a) demonstrates that in tap water for 360 days, the GP mortar exhibits a

598

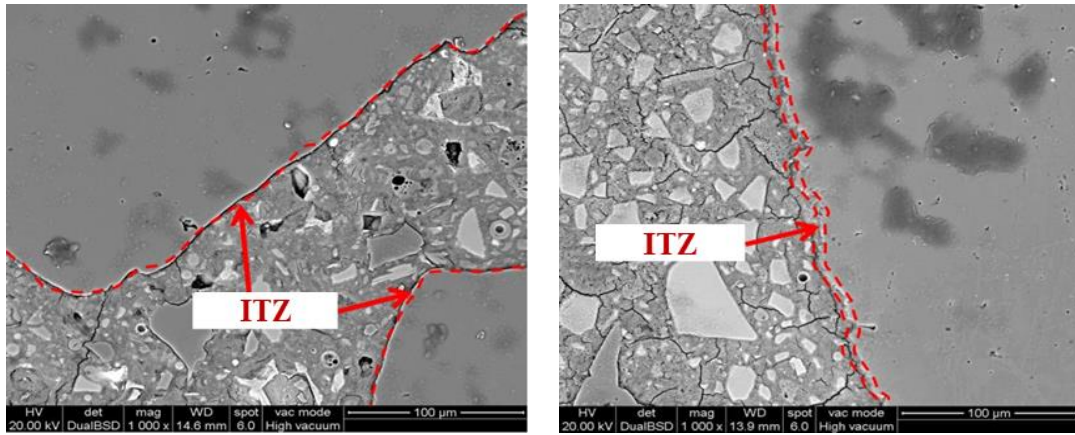
tight bond with the aggregate, without a distinct boundary of interfacial transition. Fig.

599

12(b) shows that after immersion in artificial seawater for 360 days, the interface area

600 between the GP mortar and aggregate does not show a significant increase, but some
601 areas exhibit fine cracks.

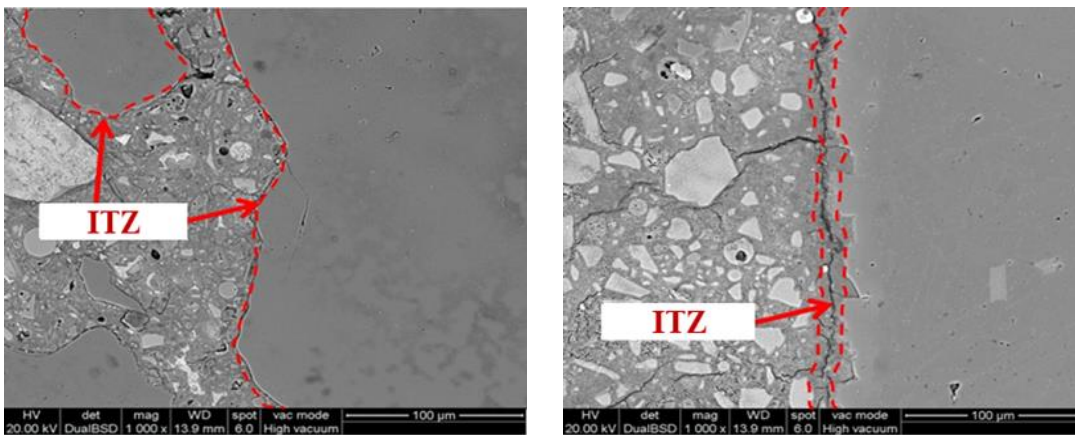
602 Fig. 13(a) illustrates that in the PC concrete samples, there is a wide black area
603 accompanied by a distribution of porosity between the PC mortar and aggregate. This
604 indicates the presence of an obvious interfacial transition zone (ITZ) in the PC
605 concrete samples, which is more pronounced compared to the GPC samples. Fig. 13(b)
606 further demonstrates that the ITZ of the PC concrete samples becomes more apparent
607 after seawater corrosion, along with a higher proportion of pores and cracks.



(a) GPC in water for 360 days

(b) GPC in artificial seawater for 360 days

608 **Fig. 12.** Interfacial transition zone of GPC after 360 days corrosion



(a) PC concrete in water for 360 days

(b) PC concrete in artificial seawater for 360
days

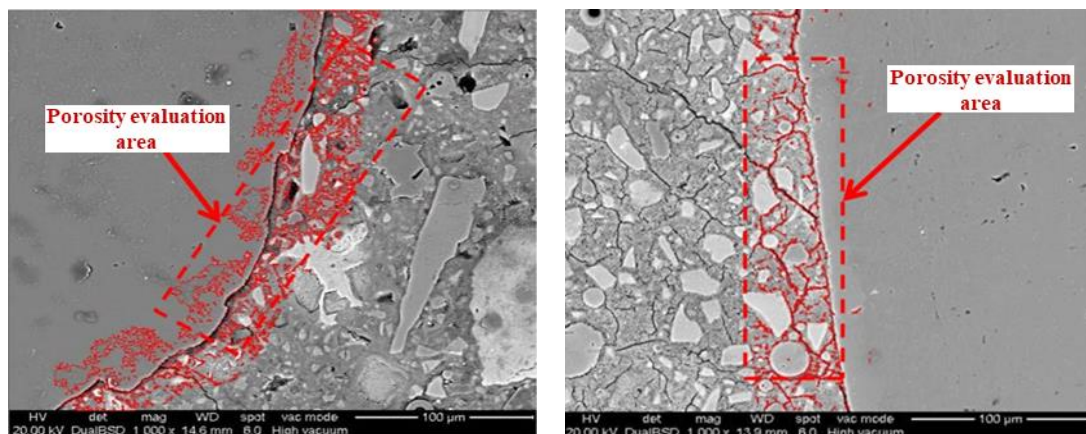
609 **Fig. 13.** Interfacial transition zone of PC concrete after 360 days corrosion

610 The porosity of the interfacial transition zone (ITZ) in concrete was further
611 calculated using the fractal theory with the aid of Image-Pro Plus (IPP) image

612 processing software. Fig. 14 and 15 display the IPP image processing photos of the
613 ITZ in GPC and PC concrete, respectively, while Table 14 presents the statistical
614 results of porosity.

615 After immersion in tap water for 360 days, the average porosity of the ITZ in
616 GPC and PC concrete samples is approximately 27.89% and 37.97%, respectively.
617 This indicates that the average porosity of the ITZ in GPC is approximately 36.0%
618 lower than that in PC concrete.

619 Following 360 days of artificial seawater corrosion, the average porosity of the
620 ITZ in GPC samples only increases by 4.44%, reaching approximately 29.13% in total.
621 In contrast, the average porosity of the ITZ in PC concrete increases from 37.97% to
622 40.74%, exhibiting a 7.29% increase compared to 360 days of tap water corrosion.
623 These findings indicate that GPC possesses a smaller porosity and a lower proportion
624 of porosity increase compared to PC concrete after seawater corrosion. This
625 demonstrates the excellent resistance of GPC to seawater corrosion.

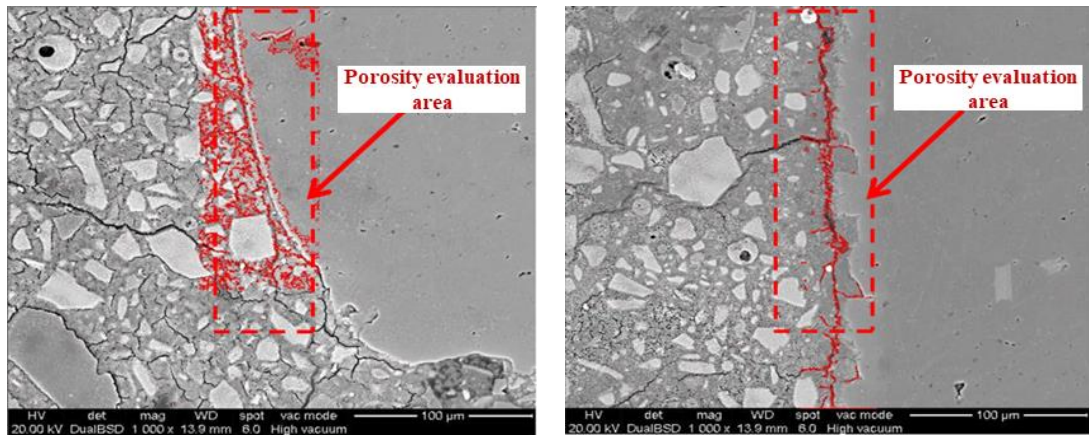


(a) GPC in water for 360 days

(b) GPC in artificial seawater for 360 days

626

Fig. 14. Interfacial transition zone of GPC after corrosion



(a) PC concrete in water for 360 days

(b) PC concrete in artificial seawater for 360 days

627 **Fig. 15.** Interfacial transition zone of PC concrete after corrosion

628 **Table 14** Porosity of interfacial transition zone in concrete after corrosion

Porosity	GPC		PC concrete	
	water for 360 d	artificial Seawater 360 d	Reference	artificial Seawater 360 d
Range	23.25~31.43	22.53~33.30	32.03~43.26	34.06~47.06
Average value(%)	27.89	29.13	37.97	40.74

629 Note. 10 images were selected to analyze the porosity of the interfacial transition zone
630 of concretes.

631 4.8.2 Microstructure characteristics of interface between BFRP bars and geopolymer
632 in seawater

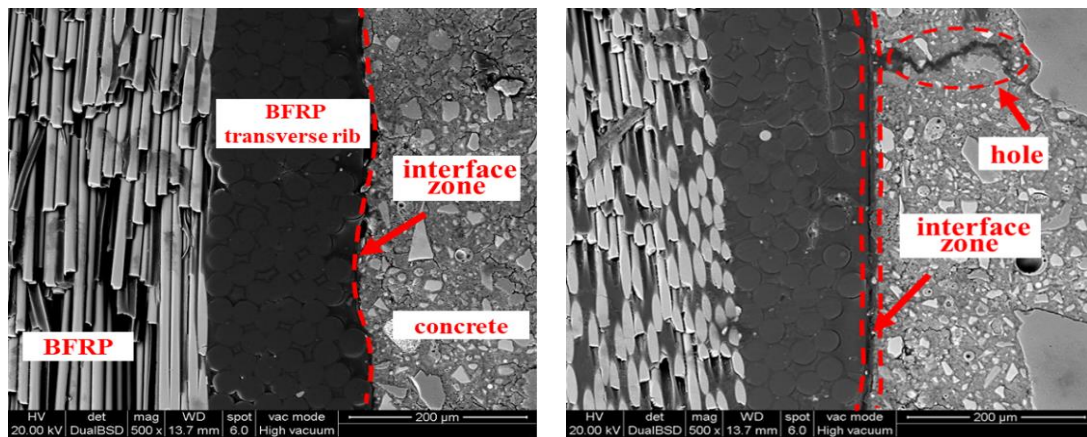
633 In the seawater environment, the microstructure characteristics of the interface
634 between BFRP bars and GPC were examined. Fig. 16 (a) illustrates that the BFRP
635 bars consist of basalt fibers bonded with resin and are further reinforced with
636 transverse ribs. The interface between the BFRP bars and GPC exhibits a tight bond
637 without any distinct interfacial transition zone (ITZ) or noticeable interfacial pores.

638 After 360 days of seawater corrosion, as shown in Fig. 16 (b), the interface
639 between the BFRP bars and GPC slightly expanded. Some cracks and pores appeared
640 in the GPC, but the bond between the GPC and BFRP bars remained relatively tight.

641 These observations suggest that even after seawater corrosion, the bond between
642 the BFRP bars and GPC remains intact, indicating the favorable compatibility and

643 durability of the interface in the seawater environment.

644 Fig. 16 (a) shows that BFRP bars are composed of resin bonded basalt fibers and
645 then wound with transverse ribs. BFRP bars are tightly bonded to GPC with no
646 obvious ITZ and no obvious interfacial pores. Fig. 16 (b) shows that the interface
647 between BFRP bars and GPC was slightly enlarged after 360 days of seawater
648 corrosion, and GPC appear some cracks and pores. It is noted that the bond between
649 the GPC and BFRP bars is still relatively tight.



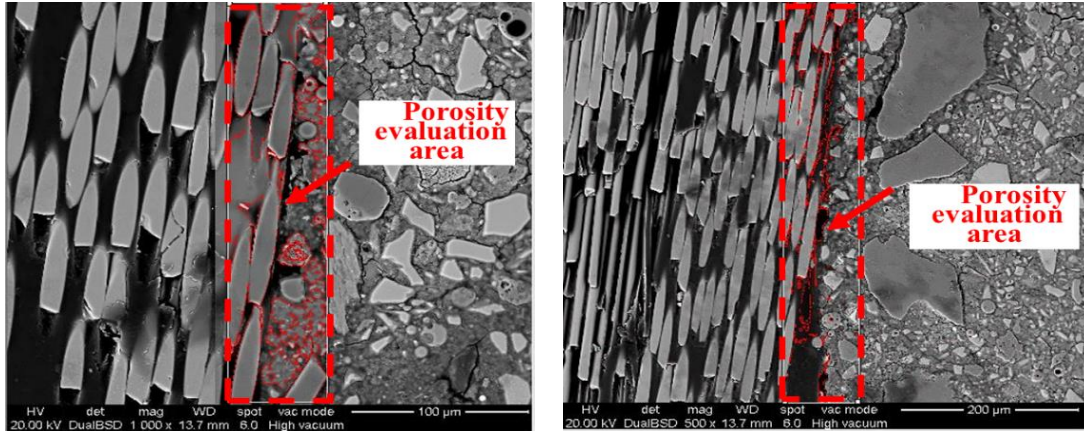
(a) Before corrosion

(b) After artificial seawater for 360 days

650 **Fig. 16.** Interface between BFRP bars and GPC before and after corrosion

651 To analyze the porosity of the interface area between the BFRP bars and GPC,
652 IPP image processing software was utilized. Fig. 17 presents the results of porosity
653 analysis before and after artificial seawater corrosion. The statistical data of porosity
654 are summarized in Table 15.

655 Before seawater corrosion, the interface between the BFRP bars and GPC
656 exhibited a tight bond, and the average porosity of the interfacial transition zone (ITZ)
657 was measured to be 27.88%. Following seawater corrosion, the average porosity of
658 the ITZ increased slightly to 29.06%, which represents a 1.2% increment compared to
659 the pre-corrosion condition. These results indicate that seawater corrosion has a
660 negligible impact on the porosity of the ITZ between the GPC and BFRP bars.



(a) GPC in water

(b) GPC in artificial seawater for 360 days

661 **Fig. 17.** Interfacial transition zone of BFRP bars in GPC after corrosion

662 **Table 15** Porosity of interface between BFRP bars and GPC after corrosion

Porosity/%	GPC	
	Reference	Immersed in artificial seawater for 360 days
Range	24.10~31.58	24.90~33.30
Average value/%	27.88	29.06

663 Note. 10 images were selected to analyze the porosity of the interface between BFRP
664 and GPC.

665 5 Conclusion

666 This study focused on investigating the corrosion resistance and interface
667 characteristics of GPC and BFRP bars in a seawater environment. The main emphasis
668 of this research was on analyzing the ionic attack resistance of BFRP reinforced
669 geopolymer concrete using laboratory-simulated seawater conditions. However, it is
670 essential to acknowledge that in actual marine environments, ion migration occurs not
671 only through diffusion but also potentially involves convective effects under
672 hydrostatic pressure.

673 Several critical questions remain to be addressed: How can we simulate ocean
674 conditions more realistically through systematically designed experiments? What are
675 the effects of competing antagonistic processes on the performance of BFRP
676 reinforced geopolymer concrete when subjected to multiple-ion combined attack in
677 marine environments? To answer these questions, further studies employing
678 systematically designed experiments and long-term observations will be crucial. Such
679 research endeavors will not only help refine the proposed mathematical models but
680 also enhance our understanding of the behavior of BFRP reinforced geopolymer

681 concrete under realistic marine conditions.

682 Based on the findings of the present study, the following specific conclusions
683 may be drawn:

684 (1) The corrosion resistance of GPC exhibited an initial sharp increase, followed by a
685 slower increase, and finally reached a stable state after 90 days of exposure. The
686 volume corrosion resistance coefficient and strength corrosion resistance
687 coefficient of GPC after 360 days of immersion were 0.06 and 0.085, respectively,
688 indicating excellent resistance to seawater corrosion. A degradation model for the
689 mechanical performance of GPC in a marine environment was established.

690

691 (2) GP mortar demonstrated superior resistance to ion migration compared to PC
692 mortar. The migration properties of chloride ions (Cl^-), sulfate ions (SO_4^{2-}), and
693 magnesium ions (Mg^{2+}) were evaluated, with Cl^- showing the highest migration,
694 followed by SO_4^{2-} and Mg^{2+} .

695

696 (3) The tensile strength degradation of BFRP bars in seawater combined with an
697 alkaline environment was more pronounced than in seawater alone. Wrapping
698 BFRP bars in GP mortar mitigated the reduction in tensile strength in seawater,
699 and a smaller BFRP diameter resulted in reduced deterioration. The ultimate
700 strengths of BFRP bars with diameters of 6 mm and 8 mm were 695 MPa and 663
701 MPa, respectively. A degradation model for the tensile strength of BFRP bars in
702 marine environments was established.

703

704 (4) Microscopic analysis revealed that seawater corrosion had little impact on the
705 porosity of the dual interfaces in BFRP bars reinforced with geopolymer concrete.
706 The average porosity of the interfacial transition zone (ITZ) between GP paste
707 and aggregate was significantly lower than that of PC concrete. The ITZ between
708 BFRP bars and GP paste exhibited a slight increase in porosity, but still
709 maintained tight interfacial bonding and narrow interface widths. Seawater
710 corrosion did not significantly affect the ITZ structure of BFRP reinforced
711 geopolymer concrete.

712

713 These findings contribute to a better understanding of the corrosion behavior and

714 interface characteristics of GPC and BFRP bars in seawater environments, and
715 provide valuable insights for the development of corrosion-resistant and durable
716 concrete structures.

717

718 **ACKNOWLEDGEMENTS**

719 This study was funded by Natural Science Foundation of Guangxi Province
720 (2021GXNSFAA220045), China Postdoctoral Science Foundation (2021M690765),
721 Systematic Project of Guangxi Key Laboratory of Disaster Prevention and
722 Engineering Safety (2021ZDK007), National Key Research and Development
723 Program of China (2021YFB2600903) and National Natural Science Foundation of
724 China (U2006224).

725

726 **REFERENCE**

- 727 [1] Zhang B, Zhu H, Li F Z, Dong Z Q, Zhang P. Compressive stress-strain
728 behavior of seawater coral aggregate concrete incorporating eco-efficient
729 alkali-activated slag materials [J]. *Construction and Building Materials*, 2021,
730 299.
- 731 [2] Zhang B, Zhu H, Cao R M, Ding J M, Chen X H. Feasibility of using
732 geopolymers to investigate the bond behavior of FRP bars in seawater sea-
733 sand concrete [J]. *Construction and Building Materials*, 2021, 282.
- 734 [3] Zhang B, Zhu H, Lu F. Fracture properties of slag-based alkali-activated
735 seawater coral aggregate concrete [J]. *Theoretical and Applied Fracture*
736 *Mechanics*, 2021, 115.
- 737 [4] Chen G, Zheng D P, Chen Y W, Lin J X, Lao W J, Guo Y C, Chen Z B, Lan X
738 W. Development of high performance geopolymer concrete with waste rubber
739 and recycle steel fiber: A study on compressive behavior, carbon emissions
740 and economical performance [J]. *Construction and Building Materials*, 2023,
741 393.
- 742 [5] Elahi M M A, Hossain M M, Karim M R, Zain M F M, Shearer C. A review
743 on alkali-activated binders: Materials composition and fresh properties of
744 concrete [J]. *Construction and Building Materials*, 2020, 260.
- 745 [6] Morsy A M, Ragheb A M, Shalan A H, Mohamed O H. Mechanical
746 Characteristics of GGBFS/FA-Based Geopolymer Concrete and Its
747 Environmental Impact [J]. *Practice Periodical on Structural Design and*
748 *Construction*, 2022, 27(2).
- 749 [7] Perumal P, Sreenivasan H, Luukkonen T, Kantola A M, Telkki V V, Kinnunen
750 P, Illikainen M. High strength one-part alkali-activated slag blends designed

- 751 by particle packing optimization [J]. *Construction and Building Materials*,
752 2021, 299.
- 753 [8] Shehata N, Sayed E T, Abdelkareem M A. Recent progress in environmentally
754 friendly geopolymers: A review [J]. *Science of The Total Environment*, 2021,
755 762: 143166.
- 756 [9] Wang A G, Zheng Y, Zhang Z H, Liu K W, Li Y, Shi L, Sun D S. The
757 Durability of Alkali-Activated Materials in Comparison with Ordinary
758 Portland Cements and Concretes: A Review [J]. *Engineering*, 2020, 6(6): 695-
759 706.
- 760 [10] Zhang B, Zhu H, Wang Q, Shah K W, Wang W. Design and properties of
761 seawater coral aggregate alkali-activated concrete [J]. *Journal of Sustainable
762 Cement-Based Materials*, 2022, 11(3): 175-84.
- 763 [11] Xiao J Z, Qiang C B, Nanni A, Zhang K J. Use of sea-sand and seawater in
764 concrete construction: Current status and future opportunities [J]. *Construction
765 and Building Materials*, 2017, 155: 1101-11.
- 766 [12] Li J L, Xie J H, Liu F, Lu Z Y. A critical review and assessment for FRP-
767 concrete bond systems with epoxy resin exposed to chloride environments [J].
768 *Composite Structures*, 2019, 229.
- 769 [13] Lu Z Y, Li J L, Xie J H, Huang P Y, Xue L F. Durability of flexurally
770 strengthened RC beams with prestressed CFRP sheet under wet-dry cycling in
771 a chloride-containing environment [J]. *Composite Structures*, 2021, 255.
- 772 [14] Yan F, Lin Z B, Yang M J. Bond mechanism and bond strength of GFRP bars
773 to concrete: A review [J]. *Composites Part B-Engineering*, 2016, 98: 56-69.
- 774 [15] Torres L, Sharaky I A, Barris C, Baena M. EXPERIMENTAL STUDY OF
775 THE INFLUENCE OF ADHESIVE PROPERTIES AND BOND LENGTH
776 ON THE BOND BEHAVIOUR OF NSM FRP BARS IN CONCRETE [J].
777 *Journal of Civil Engineering and Management*, 2016, 22(6): 808-17.
- 778 [16] Aslani F, Sun J B, Bromley D, Ma G W. Fiber-reinforced lightweight self-
779 compacting concrete incorporating scoria aggregates at elevated temperatures
780 [J]. *Structural Concrete*, 2019, 20(3): 1022-35.
- 781 [17] Aslani F, Sun J B, Huang G Q. Mechanical Behavior of Fiber-Reinforced Self-
782 Compacting Rubberized Concrete Exposed to Elevated Temperatures [J].
783 *Journal of Materials in Civil Engineering*, 2019, 31(12).
- 784 [18] Thomas R J, Ariyachandra E, Lezama D, Peethamparan S. Comparison of
785 chloride permeability methods for Alkali-Activated concrete [J]. *Construction
786 and Building Materials*, 2018, 165: 104-11.
- 787 [19] Gunasekara C, Law D, Bhuiyan S, Setunge S, Ward L. Chloride induced
788 corrosion in different fly ash based geopolymer concretes [J]. *Construction
789 and Building Materials*, 2019, 200: 502-13.
- 790 [20] Amorim Júnior N S, Andrade Neto J S, Santana H A, Cilla M S, Ribeiro D V.
791 Durability and service life analysis of metakaolin-based geopolymer concretes
792 with respect to chloride penetration using chloride migration test and corrosion
793 potential [J]. *Construction and Building Materials*, 2021, 287: 122970.
- 794 [21] Monticelli C, Natali M E, Balbo A, Chiavari C, Zanutto F, Manzi S, Bignozzi

- 795 M C. Corrosion behavior of steel in alkali-activated fly ash mortars in the light
 796 of their microstructural, mechanical and chemical characterization [J]. *Cement*
 797 *and Concrete Research*, 2016, 80: 60-8.
- 798 [22] Dzunuzovic N, Komljenovic M, Nikolic V, Ivanovic T. External sulfate attack
 799 on alkali-activated fly ash-blast furnace slag composite [J]. *Construction and*
 800 *Building Materials*, 2017, 157: 737-47.
- 801 [23] Kuri J C, Nuruzzaman M, Sarker P K. Sodium sulphate resistance of
 802 geopolymer mortar produced using ground ferronickel slag with fly ash [J].
 803 *Ceramics International*, 2023, 49(2): 2765-73.
- 804 [24] Elyamany H E, Abd Elmoaty A M, Elshaboury A M. Magnesium sulfate
 805 resistance of geopolymer mortar [J]. *Construction and Building Materials*,
 806 2018, 184: 111-27.
- 807 [25] Saavedra W G V, Angulo D E, De Gutierrez R M. Fly Ash Slag Geopolymer
 808 Concrete: Resistance to Sodium and Magnesium Sulfate Attack [J]. *Journal of*
 809 *Materials in Civil Engineering*, 2016, 28(12).
- 810 [26] Pasupathy K, Berndt M, Sanjayan J, Rajeev P, Cheema D S. Durability of low-
 811 calcium fly ash based geopolymer concrete culvert in a saline environment [J].
 812 *Cement and Concrete Research*, 2017, 100: 297-310.
- 813 [27] Tennakoon C, Shayan A, Sanjayan J G, Xu A M. Chloride ingress and steel
 814 corrosion in geopolymer concrete based on long term tests [J]. *Materials &*
 815 *Design*, 2017, 116: 287-99.
- 816 [28] Dong Z Q, Wu G, Zhao X L, Zhu H, Lian J L. Durability test on the flexural
 817 performance of seawater sea-sand concrete beams completely reinforced with
 818 FRP bars [J]. *Construction and Building Materials*, 2018, 192: 671-82.
- 819 [29] Monticelli C, Natali M E, Balbo A, Chiavari C, Zanotto F, Manzi S, Bignozzi
 820 M C. A study on the corrosion of reinforcing bars in alkali-activated fly ash
 821 mortars under wet and dry exposures to chloride solutions [J]. *Cement and*
 822 *Concrete Research*, 2016, 87: 53-63.
- 823 [30] Tittarelli F, Mobili A, Giosue C, Belli A, Bellezze T. Corrosion behaviour of
 824 bare and galvanized steel in geopolymer and Ordinary Portland Cement based
 825 mortars with the same strength class exposed to chlorides [J]. *Corrosion*
 826 *Science*, 2018, 134: 64-77.
- 827 [31] Wang W R, Chen H S, Li X Y, Zhu Z G. Corrosion behavior of steel bars
 828 immersed in simulated pore solutions of alkali-activated slag mortar [J].
 829 *Construction and Building Materials*, 2017, 143: 289-97.
- 830 [32] Wang Z K, Zhao X L, Xian G J, Wu G, Raman R K S, Al-Saadi S, Haque A.
 831 Long-term durability of basalt- and glass-fibre reinforced polymer
 832 (BFRP/GFRP) bars in seawater and sea sand concrete environment [J].
 833 *Construction and Building Materials*, 2017, 139: 467-89.
- 834 [33] Lu C H, Ni M Z, Chu T S, He L Y. Comparative Investigation on Tensile
 835 Performance of FRP Bars after Exposure to Water, Seawater, and Alkaline
 836 Solutions [J]. *Journal of Materials in Civil Engineering*, 2020, 32(7).
- 837 [34] Lu Z Y, Li Y C, Xie J H. Durability of BFRP bars wrapped in seawater sea
 838 sand concrete [J]. *Composite Structures*, 2021, 255.

- 839 [35] Luo Z Y, Li W G, Wang K J, Castel A, Shah S P. Comparison on the properties
840 of ITZs in fly ash-based geopolymer and Portland cement concretes with
841 equivalent flowability [J]. *Cement and Concrete Research*, 2021, 143.
- 842 [36] Cai Y J, Xiao S H, Chen Y W, Huang Z R, Lin J X, Guo Y C, Peng Y Q, Xie Z
843 H. Tensile behavior and durability prediction of GFRP-steel composite bars
844 under chloride environments [J]. *Journal of Materials Research and
845 Technology-Jmr&T*, 2023, 23: 5746-59.
- 846 [37] Xiong Z, Wei W, Liu F, Cui C, Li L, Zou R, Zeng Y. Bond behaviour of
847 recycled aggregate concrete with basalt fibre-reinforced polymer bars [J].
848 *Composite Structures*, 2021, 256: 113078.
- 849 [38] Xiong Z, Mai G, Qiao S, He S, Zhang B, Wang H, Zhou K, Li L. Fatigue bond
850 behaviour between basalt fibre-reinforced polymer bars and seawater sea-sand
851 concrete [J]. *Ocean & Coastal Management*, 2022, 218: 106038.
- 852 [39] Zou R, Liu F, Xiong Z, He S, Li L, Wei W. Experimental study on fatigue
853 bond behaviour between basalt fibre-reinforced polymer bars and recycled
854 aggregate concrete [J]. *Construction and Building Materials*, 2021, 270:
855 121399.
- 856 [40] Xiong Z, Wei W, He S, Liu F, Luo H, Li L. Dynamic bond behaviour of fibre-
857 wrapped basalt fibre-reinforced polymer bars embedded in sea sand and
858 recycled aggregate concrete under high-strain rate pull-out tests [J].
859 *Construction and Building Materials*, 2021, 276: 122195.
- 860 [41] Neupane K. “Fly ash and GGBFS based powder-activated geopolymer
861 binders: A viable sustainable alternative of portland cement in concrete
862 industry” [J]. *Mechanics of Materials*, 2016, 103: 110-22.
- 863 [42] Khan M S H, Castel A, Akbarnezhad A, Foster S J, Smith M. Utilisation of
864 steel furnace slag coarse aggregate in a low calcium fly ash geopolymer
865 concrete [J]. *Cement and Concrete Research*, 2016, 89: 220-9.
- 866 [43] Tian Z, Zhang Z, Liu H, Zheng W, Tang X, Gui Z. Interfacial characteristics
867 and mechanical behaviors of geopolymer binder with steel slag aggregate:
868 Insights from molecular dynamics [J]. *Journal of Cleaner Production*, 2022,
869 362: 132385.
- 870 [44] Ren X, Zhang L. Experimental study of interfacial transition zones between
871 geopolymer binder and recycled aggregate [J]. *Construction and Building
872 Materials*, 2018, 167: 749-56.
- 873 [45] Yang Y, Chen Z, Feng W, Nong Y, Yao M, Tang Y. Shrinkage compensation
874 design and mechanism of geopolymer pastes [J]. *Construction and Building
875 Materials*, 2021, 299: 123916.
- 876 [46] Lee S L, Wong S F, Swaddiwudhipong S, Wee T H, Loo Y H. Accelerated test
877 of ingress of chloride ions in concrete under pressure and concentration
878 gradients [J]. *Magazine of Concrete Research*, 1996, 48(174): 15-25.
- 879

1 **Beyond Time: Enhancing Corrosion Resistance of Geopolymer Concrete and**
2 **BFRP Bars in Seawater**

3 Zheng Chen¹; Jiamin Yu²; Yumei Nong³; Yongmin Yang⁴; Hexin Zhang⁵; and Yunchao
4 Tang^{*,6}

5 ¹Professor

6 State Key Laboratory of Featured Metal Materials and Life-cycle Safety for
7 Composite Structures, Key Laboratory of Disaster Prevention and Structural Safety of
8 Ministry of Education, Guangxi Key Laboratory of Disaster Prevention and
9 Engineering Safety, School of Civil Engineering and Architecture, Guangxi University,
10 Nanning 530004, China. Email address: chenzheng@gxu.edu.cn

11 ²Ph.D Candidate

12 Key Laboratory of Disaster Prevention and Structural Safety of Ministry of Education,
13 School of Civil Engineering and Architecture, Guangxi Key Laboratory of Disaster
14 Prevention and Engineering Safety, Guangxi University, Nanning 530004, China.
15 Email address: 2427376485@qq.com

16 ³Ph.D

17 Key Laboratory of Disaster Prevention and Structural Safety of Ministry of Education,
18 School of Civil Engineering and Architecture, Guangxi Key Laboratory of Disaster
19 Prevention and Engineering Safety, Guangxi University, Nanning 530004, China.
20 Email address: nongyumei1222@outlook.com

21 ⁴Professor

22 Guangdong Lingnan Township Green Building Industrialization Engineering
23 Technology Research Center, Zhongkai University of Agriculture and Engineering,
24 Guangzhou 510225, China. Email address: 381982967@qq.com

25 ⁵Professor

26 School of Computing, Engineering and the Built Environment, Edinburgh Napier
27 University, 10 Colinton Road, Edinburgh, Scotland, UK, EH10 5DT. Email address:
28 j.zhang@napier.ac.uk

29 ⁶Associate Professor

30 State Key Laboratory of Featured Metal Materials and Life-cycle Safety for
31 Composite Structures, Key Laboratory of Disaster Prevention and Structural Safety of
32 Ministry of Education, Guangxi Key Laboratory of Disaster Prevention and
33 Engineering Safety, School of Civil Engineering and Architecture, Guangxi University,
34 Nanning 530004, China. Email address: joshua0115@gxu.edu.cn

35
36 **ABSTRACT:** To improve the durability of Basalt fiber reinforced polymer (BFRP)
37 bars reinforced geopolymer concrete (GPC), it is important to study the time-
38 dependent variation of the corrosion resistance ability of GPC and BFRP in a seawater
39 environment. This paper presents an experimental investigation to study the time-
40 dependent mechanical properties and durability of BFRP bars and geopolymer
41 materials synthesized by granulated blast furnace slag (GGBFS), fly ash, and silica
42 fume. The resulting GPC and Portland cement (PC) concrete were exposed to
43 artificial seawater. The mechanical properties of GPC were evaluated by analyzing
44 and comparing the volume expansion and strength loss rates of GPC and PC concrete
45 in an artificial seawater environment. The corrosion resistance of geopolymer (GP)

46 mortar and PC mortar was evaluated by studying the migration ability and pore
47 structure in corrosive ions attack (Cl^- , SO_4^{2-} , Mg^{2+}) in artificial seawater. Moreover,
48 the time-dependent tensile strength of BFRP was comparatively investigated by
49 immersing in different solutions (tap water, artificial seawater, and alkaline simulated
50 seawater). In addition, the dual interface transition zones (ITZs) characteristics of
51 BFRP reinforced GPC under artificial seawater were also investigated by SEM and
52 BSE tests. The results showed that the volume expansion rate and strength loss rate of
53 GPC decreased by 77.6% and 8.7%, respectively, after 360 days of seawater corrosion
54 compared with PC concrete. This enabled the development of a time-dependent
55 strength model of GPC in marine environments. The coefficient of ions diffusion in
56 GP mortar is much lower than that of PC mortar, and GP mortar shows excellent
57 resistance to ion migration. In addition, the effect of seawater corrosion on the tensile
58 strength of BFRP bars increases with the increase of bars' diameter, and the ultimate
59 strengths of BFRP bars with diameters of 6 mm and 8 mm were 695 MPa and 663
60 MPa, respectively. The tensile strength degradation model of BFRP bars in
61 geopolymer concrete under seawater corrosion was established. After 360 days of
62 seawater immersion, the average porosity of the ITZ between geopolymer and
63 aggregates, and the average porosity of the ITZ between geopolymer and BFRP bars
64 increased insignificantly compared to that of PC concrete. This research can provide a
65 theoretical basis for the service life prediction of BFRP reinforced geopolymer
66 concrete within marine environments.

67 **Keywords:** Geopolymer concrete, Basalt fiber reinforced polymer (BFRP) bars,
68 Seawater, Time-dependence, Interface characteristic.

69

70

71 1 Introduction

72 Geopolymer concrete (GPC) has attracted extensive attention from researchers
73 due to its excellent characteristics, such as stable hydration products, compact paste
74 structure, adjustable setting time, early strength, and high strength [1-4]. Meanwhile, it
75 can effectively reduce energy consumption and greenhouse gas emissions of ordinary
76 Portland cement (OPC) production [5-10]. The process of preparing GPC is given in
77 Fig.1. In addition, GPC has excellent seawater corrosion resistance, enabling the use
78 of local materials and sea sand as aggregate, to solve the problem of insufficient river

79 sand resources. Therefore, GPC is suitable for the characteristics of marine
80 engineering construction, and it can address issues such as the shortage of materials
81 and fresh water, the influence of tidal action in the construction process, and the
82 corrosion from harmful ions in seawater in the service process of buildings.
83 Experimental results show that the mechanical properties of seawater sea sand
84 concrete (SWSSC) are similar to those of traditional concrete^[11]. However, seawater
85 and sea sand contain high concentrations of chloride ions, which will lead to the
86 corrosion of steel bars in SWSSC structures ^[12, 13]. Corrosion and expansion of steel
87 bars cause durability problems such as cracking and peeling of the protective concrete
88 layer. These problems seriously reduce the safety of SWSSC structures and lead to
89 high maintenance costs. However, fiber reinforced polymer (FRP) bars are believed to
90 be another effective way to solve these problems, potentially eliminating the
91 limitation that seawater sea sand cannot be directly used as concrete raw material ^[14].
92 Recently, basalt fiber reinforced polymer (BFRP) bars have been used in some
93 concrete structures subjected to extreme environmental conditions due to their
94 superior chemical resistance ^[15-17]. There is no corrosion and expansion problem in
95 marine environments, so BFRP reinforced geopolymer concrete (hereafter called
96 BFRP GPC) has broad application prospects in marine engineering construction.
97 However, it is worth noting that BFRP GPC has double interface transition zones
98 (ITZs), and the transport of corrosive ions in seawater in the GPC is time-dependent.
99 Existing research results do not reveal the time-dependence variation of corrosive ions
100 transported in GPC under seawater corrosion and the influence of the time-
101 dependence variation on the performance of BFRP bars. Thus, it is necessary to study
102 the time-dependence mechanism of GPC and BFRP bars under seawater corrosion as
103 it can provide a basis for service life prediction of BFRP GPC in marine environments.

104 In previous studies, there have been numerous research efforts on the seawater
105 corrosion resistance of GPC, including Cl^- permeability resistance, sulfate resistance
106 (SO_4^{2-} and Mg^{2+}), and the variation of properties in artificial seawater. On Cl^-
107 permeability resistance of GPC, Thomas et al. ^[18] studied the chloride ion
108 permeability of alkali-activated fly ash, alkali-activated slag, and PC concrete
109 immersed in 3% NaCl for 90 days. In general, alkali-activated slag concrete has better
110 chloride ion permeability resistance, slightly better than PC concrete. Gunasekara et al.
111 ^[19] studied the corrosion of fly ash-based geopolymers and PC concrete immersed in

112 3% NaCl for 540 days. Test results indicated that the three-dimensional N-A-S-H and
113 C-A-S-H crosslinking formed in the fly ash-based geopolymers reduces the diffusion
114 of chloride ions into the depth of the concrete, resulting in a lower corrosion rate
115 compared to PC concrete. Amorim Junior et al. [20] showed that metakaolin GPC has
116 similar or higher durability than OPC concrete by the migration test of chloride.
117 Therefore, GPC has excellent resistance to chloride ion penetration, which is related
118 to the type of activator, alkali content, and curing mode in GPC. In addition, the
119 presence of sulfate ions and magnesium ions can also affect the durability of concrete
120 structures in the marine environment. Krivenko et al. [21] proposed that slag-based
121 geopolymer concrete has better sulfate resistance than PC paste, even better than
122 sulfate-resistant cement pastes, and sodium sulfate is beneficial to promote the
123 polymerization of GPC continuous reaction, making the structure more compact.
124 Dzunuzovic et al. [22] studied the influence of 5% sodium sulfate solution on the
125 mechanical properties and microstructure properties of fly ash-slag base binder (FA-
126 BFS) and PC concrete for 180 days. During the whole immersion period, the strength
127 loss index was higher than 1, and the compressive strength of specimens exposed to
128 the sulfate solution developed slowly. XRD (X-ray diffractometer) analysis shows that
129 there were no new substances produced by the alkali-activated material and sulfate
130 reaction. Sanghamitra Jena [23] used silica ash to partially replace fly ash to prepare
131 GPC. Specimens were respectively immersed in 5% NaCl and 2% MgSO₄ corrosive
132 solution for 28 days. The experimental results showed that adding fly ash and silica
133 fume can improve the strength of GPC. Hafez E. Elyamany et al. [24] compared the
134 corrosion resistance of GP mortar with added slag and silica fume substituted for fly
135 ash, GP mortar with fly ash, and OPC mortar after immersion in 10% MgSO₄ solution
136 for 48 weeks. The results showed that the corrosion resistance of GP mortar mixed
137 with slag and silica fume is higher than that of GP mortar mixed with fly ash only, and
138 both are higher than that of OPC mortar. Valencia Saavedra et al. [25] studied the
139 performance of GPC (composed of 80% fly ash and 20% mineral powder) and OPC
140 concrete after curing in 5% MgSO₄ solution for 360 days. The results showed that the
141 expansion rate of FA/GBFS (Class fly ash and granulated blast-furnace slag) concrete
142 is 0.04% and the mechanical resistance is reduced by 33%, while the expansion rate
143 of OPC concrete is 0.08% and the mechanical resistance is reduced by 48% under the
144 same conditions. Therefore, FA/GBFS concrete has better resistance to MgSO₄

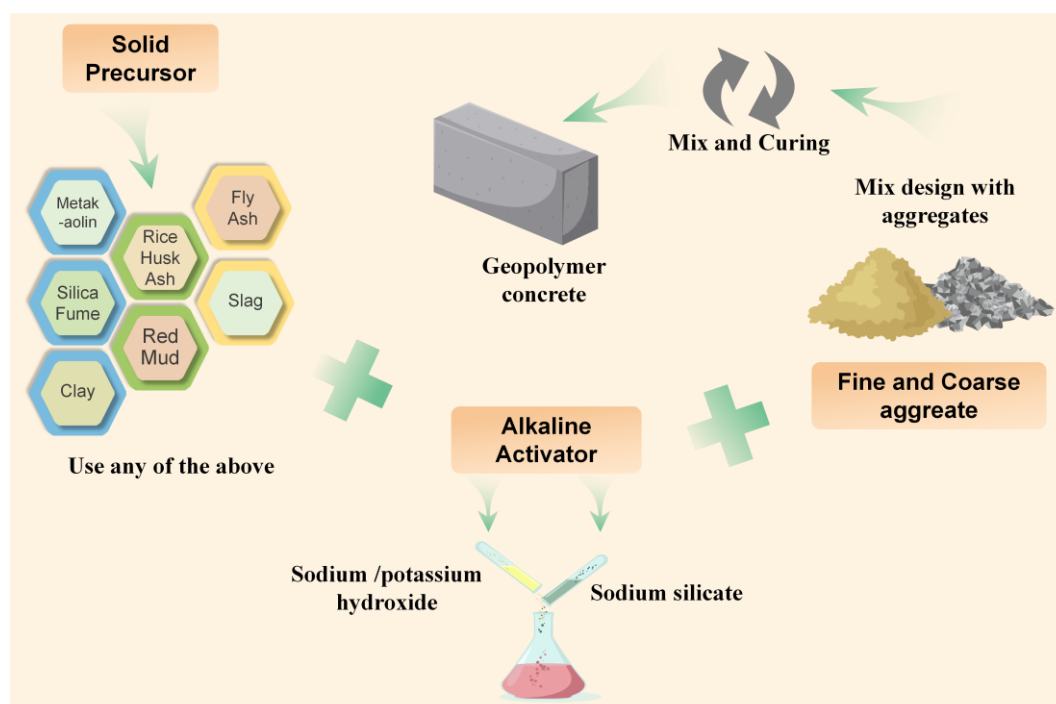
145 corrosion than OPC concrete. The above research shows that all kinds of GPC have
146 better sulfate resistance than OPC concrete, as the reaction products are difficult to
147 corrode and the microstructure is compact. However, existing research on the
148 seawater corrosion resistance of GPC does not consider the time-dependence of
149 corrosive ion transport, and the influence mechanism of the dynamic transport process
150 of corrosive ions in GPC on their macroscopic properties and microstructure evolution
151 has not been determined. In addition, the corrosion resistance of GPC in marine
152 environments is an important problem to understand to enable their successful
153 application [20, 26, 27].

154 Some researchers have studied the corrosion resistance of steel bars in GP
155 mortars and concrete in marine environments [21, 28-32], but few articles have evaluated
156 the long-term performance (such as durability and strength degradation) of BFRP bars.
157 Yan et al. [14] concluded that the tensile strength of BFRP bars in an alkaline concrete
158 pore solution decreases much faster than in distilled water, salt, or acid environments.
159 In addition, they found that the long-term performance degradation of BFRP bars in
160 alkaline solutions was more obvious than in seawater because OH^- broke the Si-O-Si
161 bonds in the basalt fibers [13]. Z. Wang et al. [32] conducted accelerated corrosion tests
162 on BFRP bars under different pH values, immersion temperatures, and durations.
163 Subsequently, they used Arrhenius degradation theory to predict the long-term
164 behavior of BFRP bars under service conditions. The study [33] evaluated the residual
165 tensile properties of BFRP bars coated with different SWSSC thicknesses exposed to
166 tap water, simulated seawater, and alkaline solution at 28°C, 40°C, 60°C. It was found
167 that the alkaline solution has a more harmful effect on the tensile properties of BFRP
168 bars than tap water or seawater. Alkalinity is the key factor leading to the deterioration
169 of BFRP bars. Therefore, thicker SWSSC-coated BFRP bars have higher resistance in
170 alkaline environments, and their tensile strength retention is lower than bare BFRP
171 bars. To sum up, although BFRP bars have an excellent ability to resist chloride
172 corrosion, the high alkaline environment in concrete will deteriorate their performance
173 [33-36]. Therefore, it is important to evaluate the long-term durability of BFRP bars in
174 marine environments. Existing studies have not revealed the time-dependence
175 mechanism of the mechanical properties and microstructure of BFRP under seawater
176 corrosion, so further research work is necessary to establish the strength degradation
177 model of BFRP under seawater corrosion.

178 Many studies^[37-40] have focused on the macroscopic analysis of the bonding
179 properties of BFRP bars and concrete, while less research has been done on the
180 microscopic mechanism of the interface. Furthermore, interface transition zones (ITZs)
181 play a crucial role in BFRP GPC, both between aggregates and pastes and between
182 pastes and BFRP bars. While the ITZ between GP pastes and aggregates is denser
183 than that between OPC pastes and aggregates^[41], it remains a weak area prone to the
184 development of microcracks and is key to controlling the overall strength, chemical
185 corrosion resistance, permeability, and other macro properties of GPC ^[42]. Current
186 research on the ITZ between pastes and aggregates primarily focuses on PC concrete,
187 with limited investigation on GPC. Luo ^[35] compared the performance of ITZs in PC
188 concrete and GPC, finding that the interface bond between the GPC matrix and
189 aggregates is stronger than in PC concrete. In PC concrete, the ITZs contain numerous
190 crystalline hydration products, whereas in GPC, the ITZs consist of a gelate-rich paste
191 with a denser microstructure. Tian et al. ^[43] examined the interface characteristics and
192 mechanical behavior of slag aggregates and GPC, comparing different GPC/steel slag
193 interface systems. They observed that the interface interaction between GPC and steel
194 slag aggregates significantly influenced the interface properties and mechanical
195 behavior. Xin Ren et al. ^[44] conducted comparative experiments to study the bond
196 strength of ITZs between GPC and aggregate, as well as OPC and aggregate. Their
197 experiments suggested that the development of ITZ bond strength in GPC appeared to
198 be more rapid than in OPC concrete after 7 days. In summary, both domestic and
199 international scholars have investigated the microstructure, composition, and bond
200 strength of the ITZ in GPC. However, it should be noted that previous research
201 primarily relied on qualitative analyses, lacking quantitative characterization, and the
202 mechanism of deterioration remains unclear, making it difficult to establish the
203 regulatory influence of ITZ microstructure on mesoscopic and macroscopic properties.
204 Furthermore, the double interface transition zone of BFRP reinforcement geopolymer
205 concrete has not been adequately considered.

206 As a result, the time-dependent strength model of GPC and the tensile strength
207 model of BFRP in marine environments have yet to be established. Additionally, the
208 changes in composition and microstructure of reaction products with GPC when
209 exposed to corrosive ions in seawater environments are not well understood. The
210 mechanism by which corrosive ions affect the properties of double interface transition

211 zones in BFRP GPC has not been confirmed. Consequently, this study aims to
212 investigate the volume and strength loss rates of GPC in a simulated seawater
213 environment during various immersion periods. The migration of corrosive ions (Cl^- ,
214 SO_4^{2-} , Mg^{2+}) in seawater will be evaluated. Simultaneously, the tensile strength of all
215 BFRP bars will be tested after immersion in artificial seawater and alkaline simulated
216 seawater for different durations, considering the effects of GP mortar wrapping on the
217 properties of BFRP bars. The research will analyze the microstructural changes of
218 BFRP bars in artificial seawater environments. Ultimately, this study aims to provide
219 a theoretical basis for predicting the service life of BFRP GPC in marine
220 environments.



221
222 **Fig. 1.** Production of geopolymer concrete
223

224 **2 Experimental Design**

225 **2.1 Materials**

226 The feasibility of utilizing a Geopolymer in marine environments was
227 investigated using a composition comprising 70% granulated blast-furnace slag
228 (GGBFS), 12% fly ash, 5% silica fume, and 13% activator, which consisted of a solid
229 mixture of sodium silicate and sodium carbonate. The composites and chemical
230 composition of the Geopolymer are provided in Table 1 and Table 2 [45]. By

231 considering the results of MgO compensation GPC volume shrinkage, stability, and
 232 mortar strength, it was possible to prepare a Geopolymer with minimal volume
 233 shrinkage (referred to as GII) by incorporating 6% MgO (in a ratio of 60 seconds: 220
 234 seconds = 1:1) into the GPC [45]. This formulation was then used to assess its
 235 suitability for marine environments. The mixture ratio and mechanical properties of
 236 the GPC and PC concrete are presented in Table 3 and Table 4, respectively. The sand
 237 was sourced from Huilai County, Guangdong Province and is natural sea sand. Table
 238 5 provides information on the performance and ion content of the sea sand.
 239 Additionally, Table 6 presents the basic physical properties of limestone gravel. The
 240 BFRP bars were supplied by Sichuan Aerospace Tuoxin Basalt Industry Co., LTD, an
 241 industrial manufacturer. Table 7 displays the initial physical properties of the BFRP
 242 bars.

243 **Table 1.** Composition of Geopolymer (wt%)

Material	Composites				Blaine specific surface area, m ² /kg	Density, g/cm ³	Flexural strength, MPa		Compressive strength, MPa	
	GGBFS	Fly ash	Silica fume	Activator			3 d	28 d	3 d	28 d
Geopolymer	70%	12%	5%	13%	375	2.90	4.5	7.9	30.6	50.2

244 **Table 2** Chemical composition of geopolymer binder /wt%

Composition	SiO ₂	Al ₂ O ₃	Fe ₂ O ₃	TiO ₂	CaO	Mg O	SO ₃	P ₂ O ₅	K ₂ O	Na ₂ O	LOI
Geopolymer	30.5 6	19.56	2.22	0.85	34.40	3.23	1.2 3	0.05	2.09	4.88	0.9 3

245 **Table 3** Mix proportions of geopolymer and Portland cement concretes

Sample ID.	Strengt h grade	W/ C	ρ /%	Binder /(kg/m ³)	Sand /(kg/m ³)	Aggrega te /(kg/m ³)	Superplastictiz er /(kg/m ³)	Water /(kg/m ³)
P-35	C35	0.4 0	42	440	760	1050	7.92	176
GII-35		0.4 0	42	440	720	1000	/	176

246 **Table 4** Physical and mechanical properties of geopolymer and Portland cement
 247 concretes

Sample ID.	Workability		Compressive strength /MPa		
	Slumps/cm	Slump flow/mm	3 days	7 days	28 days
P-35	14.0	170	30.5	38.5	45.0

GII -35 18.0 220 39.6 45.0 56.5

248 **Table 5** Performance of sea sand from Huilai County of Guangdong Province

Fineness modulus	Particle size range	Apparent density/(kg/m ³)	Bulk density/(kg/m ³)	Shell /(wt%)	Cl ⁻ (wt%)	Mg ²⁺ (wt %)	SO ₄ ²⁻ /(wt %)
2.52	II	2590	1520	2.5~3.6	0.1008	0.0098	0.0090

249 **Table 6** Physical properties of aggregate

Percentage of flat-elongated particles /%	Crushin g index/ %	Bulk density/(kg/m ³)	Apparent density/(kg/m ³)	Voidage/%
7.5	9.1	1560	2750	43.3

250 **Table 7** Physical properties of BFRP bars

Type	Length/(mm)	Diameter/(mm)	Tensile strength/(MPa)	Anchorage length/(mm)
BFRP	1000	$\frac{6}{8}$	800~1100	400

251

252 **2.2 Exposure condition**

253 In this study, two immersion environments were employed for testing purposes.
 254 The GPC specimens were immersed in tap water, while the bare BFRP bars were
 255 immersed in artificial seawater. The composition of the artificial seawater solution
 256 was designed based on ASTM D 1141-98 and is outlined in Table 8. Considering the
 257 alkaline nature of the concrete environment, the BFRP bars were additionally
 258 immersed in alkaline simulated seawater. This simulated seawater was prepared using
 259 a saturated Ca(OH)₂ solution, following the composition specified in Table 8. To
 260 facilitate comparative analysis, BFRP bars coated with GP mortar were also immersed
 261 in artificial seawater. The exposure periods for all specimens were 28 days, 56 days,
 262 90 days, 180 days, and 360 days.

263 **Table 8** The composition of artificial seawater

Ion types	NaCl	MgCl ₂	Na ₂ SO ₄	CaCl ₂
Concentration (g/L)	4.53	20	4.09	1.16

264 3 Test methods

265 3.1 Seawater resistance of geopolymer concrete

266 3.1.1 Volume expansion and strength loss of geopolymer concrete

267 The specimens were prepared according to the mix proportions specified in Table
268 3. They were cast in the form of 150×150×150 mm blocks and cured at room
269 temperature for 24 hours. After demolding, the specimens were transferred to a
270 standard curing chamber maintained at a temperature of 25 °C and a relative humidity
271 of 95% for a period of 28 days.

272 Following the curing period, any loosely adhering portions at the corners of the
273 test blocks were removed, and the resulting volume was measured using the drainage
274 method. This initial volume measurement was recorded as the original volume of the
275 specimens.

276 During the immersion and corrosion period, the volume and compressive
277 strength of the specimens were measured after a certain duration denoted as "t" days.
278 The V_t (volume corrosion resistance coefficient) and S_t (strength corrosion resistance
279 coefficient) were utilized to characterize the seawater corrosion resistance of the
280 concrete. The physical meanings of these parameters are as follows:

$$281 \quad V_t = \frac{v_t - v_{28}}{v_{28}} \quad (1)$$

282 Where, V_t is coefficient of the volume corrosion resistance at time, t ; v_t is the volume
283 of the concrete specimens at t age (mm^3); v_{28} is the volume of the concrete specimens
284 at 28 days (mm^3).

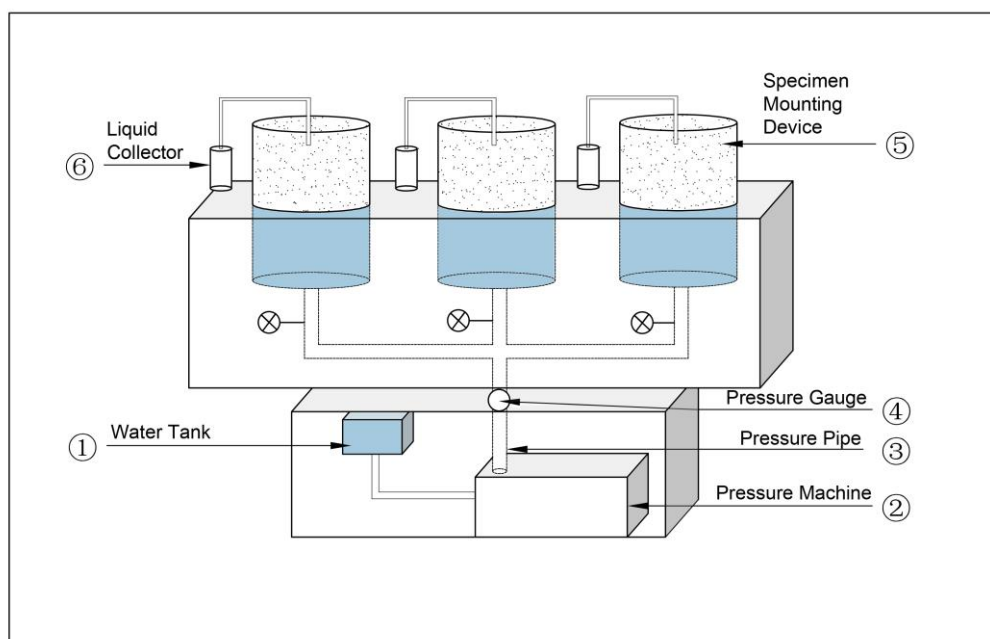
$$285 \quad S_t = \frac{s_{28} - s_t}{s_{28}} \quad (2)$$

286 Where, S_t is coefficient of the strength corrosion resistance at time, t ; s_t is the
287 compressive strength of the concrete specimens at t age (MPa); s_{28} is the compressive
288 strength of the concrete specimens at 28 days (MPa).

289 3.1.2 Ion migration resistance of geopolymer mortar

290 In order to further investigate the transport performance of corrosive ions in GP
291 mortar, a mortar mixture was prepared by incorporating artificial seawater containing
292 corrosive ions such as Cl^- , Mg^{2+} , and SO_4^{2-} . Once the mortar reached a specific age,

293 ion content measurements were conducted in each layer of the mortar along the
 294 direction of hydrostatic pressure. These measurements were used to calculate the
 295 migration coefficient of the GP mortar. For the ion migration tests, a self-made ion
 296 migration testing device was utilized, as depicted in Figure 2. The device includes a
 297 water tank ①, which is connected to an air compressor ② through a pipe. The valve is
 298 set on the pipeline, the air pressure machine ② is connected to the specimen
 299 mounting device ⑤ through the pressure pipe ③. The pressure gauge ④ is set on the
 300 pressure pipe ③, and the specimen mounting device ⑤ is installed with an osmotic
 301 liquid collector ⑥ on the upper part of the specimen mounting device. After migrating
 302 for a certain period of time, the liquid in the collector ⑥ is poured into a measuring
 303 cylinder to measure its volume, and the ion concentration in the liquid is measured by
 304 ion chromatography to calculate the amount of ions migrating for a certain period of
 305 time. Cylindrical mortar specimens with a bottom diameter of 100 mm, top diameter
 306 of 80 mm, and height of 100 mm were employed as migration specimens. The
 307 cement-to-sand ratio was 1:3, and the water-to-cement ratio was 0.5. After curing for
 308 28 days, the specimens were subjected to testing under standard conditions with a
 309 relative humidity (RH) of at least 95% and a temperature of $20\pm 2^{\circ}\text{C}$.



310
 311
 312

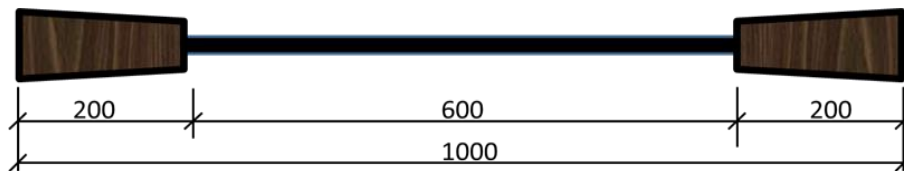
Fig. 2. The schematic diagram of device for testing ion migration in mortar specimens

313 3.2 Tensile performance of BFRP bars

314 After being immersed in tap water, artificial seawater, and alkaline simulated
315 seawater (saturated with a $\text{Ca}(\text{OH})_2$ artificial seawater solution), the BFRP bars were
316 removed and the surfaces were dried. The tensile specimens of the BFRP bars were
317 designed and manufactured following the guidelines outlined in ACI440.3R-04
318 "Guide to Test Methods for FRP Bars Reinforced Concrete Structures". The total
319 length of the tensile specimen, denoted as "L," was set to 1000 mm.

320 To prevent shear damage caused by the tensile machine fixture, adhesive anchors
321 were incorporated at both ends of the tensile test sample within a length of 200 mm,
322 as depicted in Fig. 3. These anchors were constructed using galvanized steel pipes
323 with a bottom diameter of 30 mm, top diameter of 35 mm, and thickness of 3 mm.
324 The steel sleeves were bonded to the BFRP bars by pouring epoxy resin.

325 Following the specifications outlined in the "Test Method for Basic Mechanical
326 Properties of Fiber Reinforced Composite Bars" (GB/T 30022-2013), the prepared
327 BFRP bars were subjected to a tensile test using an electro-hydraulic servo universal
328 testing machine. This test aimed to measure the ultimate tensile strength and tensile
329 strain of the specimens. A displacement control method was employed to ensure that
330 the specimens were destroyed within a timeframe of 1 to 10 minutes.



331

332 **Fig. 3.** BFRP specimen for tension test (mm)

333 3.3 Microscopic analysis

334 The microstructural tests conducted in this study included scanning electron
335 microscopy (SEM), mercury intrusion porosimetry (MIP), and backscattering electron
336 (BSE) imaging. To investigate the impact of marine corrosive substances on the
337 microstructure of GPC, different dosages of NaCl , Na_2SO_4 , and MgSO_4 were added
338 into the GP paste, as detailed in Table 9. The MIP method was employed to examine
339 the pore structure characteristics of GPC after 28 days of exposure to corrosive
340 substances. The microstructure of the BFRP bars was analyzed using SEM after 180

341 days of immersion in tap water, artificial seawater, and alkaline simulated seawater
 342 (saturated with a $\text{Ca}(\text{OH})_2$ artificial seawater solution).

343 **Table 9** Dosage of corrosion ions in geopolymer

Groups	Dosage of corrosion ions (%)								
	NaCl			Na ₂ SO ₄			MgSO ₄		
1	0	3.5	5	-	-	-	-	-	-
2	-	-	-	0	3	8	-	-	-
3	-	-	-	-	-	-	0	3	8

344 3.3.1 Scanning electron microscopy (SEM) tests

345 The hardened paste samples were fractured into pieces after being cured for a
 346 specific duration, and some of these fragments underwent gold-plating treatment. The
 347 BFRP bars were immersed in tap water, artificial seawater, and alkaline simulated
 348 seawater (saturated with a $\text{Ca}(\text{OH})_2$ artificial seawater solution) until reaching a
 349 predetermined age. Subsequently, the bars were taken out and the surfaces were dried.
 350 The microstructures of these samples were analyzed using EVO18 scanning electron
 351 microscopy (SEM) equipment, manufactured by Carl Zeiss Germany.

352 3.3.2 Mercury Intrusion Porosimetry (MIP) tests

353 MIP was employed to assess the total porosity and pore size distribution of the
 354 mortars. The samples were crushed into small pieces measuring 5×5×5 mm and
 355 soaked in ethanol for over 24 hours, with a volume ratio of approximately 1:4 for the
 356 sample to ethanol. The pore structure of the hardened paste was determined using an
 357 AutoPore IV 9500 mercury porosimeter.

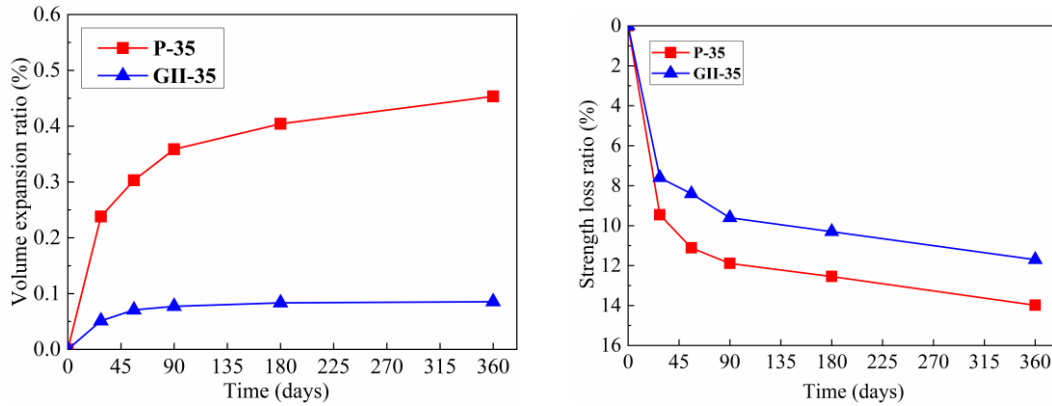
358 3.3.3 Backscattering electron (BSE) tests

359 The samples were analyzed using backscattered electron imaging with an S-
 360 3400N Scanning Electron Microscope. The sample preparation process is as follows:
 361 Initially, the fractured samples were immersed in epoxy resin and left to demold for
 362 24 hours. Subsequently, the samples solidified with epoxy resin were polished using
 363 an automatic Polish-grinding machine, employing sandpapers of various mesh sizes
 364 including 60, 120, 320, 500, 2000, and 4000. Prior to testing, the samples were coated
 365 with a layer of gold to enhance conductivity.

366 **4 Result and discussion**

367 **4.1 Time-Dependent Behavior of Geopolymer Concrete: Volume and Strength**

368 Figure 4 illustrates the seawater resistance of GPC (GII-35) and PC concrete (P-
 369 35) over an exposure period of up to 360 days. It can be observed that, compared to
 370 GPC, PC concrete exhibited a significantly higher volume expansion ratio at 180 and
 371 360 days, with increases of 384.6% and 430.0% respectively (Figure 4a). Similarly,
 372 the strength loss ratio of PC concrete at 180 and 360 days increased by 10.4% and
 373 9.6% respectively (Figure 4b). Conversely, GPC demonstrated a remarkable reduction
 374 in both volume expansion ratio and strength loss ratio, which decreased by 77.6% and
 375 8.7% respectively after 360 days of seawater corrosion. These results indicate that
 376 GPC exhibits superior resistance to seawater corrosion compared to PC concrete.



377 (a) Volume expansion
 378 (b) Strength loss
 379 **Fig. 4.** The corrosion resistance of GPC and PC concretes

380 **4.2 Time-dependent strength model of GPC in marine environments**

381 Concrete strength will change with service time under the influence of
 382 environmental factors and sustained loads. Based on the strength data of long-term
 383 concrete in actual marine engineering, scholars have analyzed its degradation pattern
 384 using regression methods and proposed a time-dependent decay model for the average
 385 strength of concrete in marine environments, as presented in Eq. (3).

$$f_c(t) = f_0 \times 1.248e^{-0.0340 \times (\ln t - 0.3468)^2} \quad (3)$$

387 Where $f_c(t)$ represents the compressive strength of concrete after t years, MPa; f_0
 388 represents the average value of initial concrete strength, MPa.

389 The time-dependence equation of concrete strength retention rate in marine

390 environments can be determined by Eq.(4). $F_c(t)$ is strength retention rate of concrete
 391 in marine environments in immersion time t .

$$392 \quad F_c(t) = \frac{f_c(t)}{f_0} = 1.248e^{-0.0340 \times (\text{Int}-0.3468)^2} \times 100\% \quad (4)$$

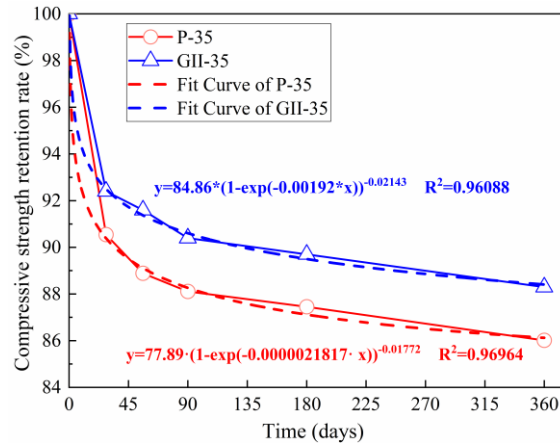
393 In Fig. 5, the fitting curve illustrates the seawater corrosion resistance test results
 394 of GPC (GII-35) and PC concrete (P-35). As time approaches infinity, the strength
 395 retention rate of GII-35 and P-35 reaches 84.9% and 77.9%, respectively. Thus, the
 396 time-dependent degradation equation for the strength retention rate of GPC in marine
 397 environments can be expressed as Eq. (5). $F_w(t)$ is strength retention rate of GPC in
 398 marine environments in immersion time t

$$399 \quad F_w(t) = \frac{84.9}{77.9} \times F_c(t) = 1.360e^{-0.0340 \times (\text{Int}-0.3468)^2} \times 100\% \quad (5)$$

400 The decay equation for the mechanical properties of GPC in marine
 401 environments can be expressed as Eq. (6).

$$402 \quad f_w(t) = f_{w0} \times 1.248e^{-0.0340 \times (\text{Int}-0.3468)^2} \quad (6)$$

403 Where $f_w(t)$ is the compressive strength of GPC after t years, MPa; f_{w0} is the average
 404 initial strength of GPC, MPa.



405
 406 **Fig.5.** Compressive strength of PC (P-35) and GPC (GII-35) in seawater for different
 407 immersion periods

408 4.3 Transport performance of ions in seawater in GP mortar

409 Under the hydrostatic pressure (1.4 MPa), the water samples of mortar specimens
 410 (mixed with artificial seawater) at different exposure ages were analyzed. By
 411 measuring the contents of Cl^- , SO_4^{2-} and Mg^{2+} in the water samples, the amount of
 412 ions permeation migration ΣA_n at different ages were obtained. Based on the ratio of

413 chemical bonding and physical adsorption, A_0 was calculated and $\Sigma A_n/A_0$ was obtained.
 414 The cumulative leaching fraction of ions can be calculated using Eq. (7). The leaching
 415 rate and cumulative leaching fraction of PC mortar and GP mortar were obtained, as
 416 shown in Table 10 and Table 11.

$$417 \quad P_t = \frac{\Sigma A(t)}{A_0} \times \frac{V}{S} \quad (7)$$

418 Where P_t is the cumulative leaching fraction of ions, cm; t is exposure time; $\Sigma A(t)$ is
 419 the accumulated leaching amount of the first n ions, g; A_0 is the amounts of ions that
 420 can migrate in the sample, g; V is the volume of sample, cm^3 ; S is the geometrical area
 421 of the solidified sample in contact with water, cm^2 .

422 **Table 10** Leaching ratio and cumulative leaching fraction of ions from Portland
 423 cement mortar

Time (d)	$\frac{\Sigma A_n}{A_0}$ (Cl^-)	P_t (Cl^-/cm)	$\frac{\Sigma A_n}{A_0}$ (SO_4^{2-})	P_t ($\text{SO}_4^{2-}/\text{cm}$)	$\frac{\Sigma A_n}{A_0}$ (Mg^{2+})	P_t (Mg^{2+}/cm)
1	0.0138	0.1168	0.0050	0.1111	0.0131	0.1161
2	0.0966	0.8178	0.0190	0.4222	0.0291	0.2589
3	0.1494	1.2648	0.0305	0.6778	0.0852	0.7572
5	0.2691	2.2781	0.0455	1.0111	0.1073	0.9541
7	0.3207	2.7149	0.0665	1.4778	0.1984	1.7639
10	0.3981	3.3702	0.1050	2.3333	0.2306	2.0500
15	0.4672	3.9551	0.1567	3.4811	0.2909	2.5861
20	0.5463	4.6248	0.1792	3.9822	0.3853	3.4244
25	0.5953	5.0396	0.2005	4.4556	0.4206	3.7383
30	0.6244	5.2859	0.2250	5.0000	0.4809	4.2744
35	0.6534	5.5314	0.2475	5.5000	0.5902	5.2461
40	0.6625	5.6085	0.2517	5.5933	0.6605	5.8711
50	0.6806	5.7617	0.2681	5.9567	0.7511	6.6767
60	0.7288	6.1697	0.2700	6.0000	0.8408	7.4733

424 **Table 11** Leaching ratio and cumulative percentage of ions from geopolymer mortar

Time (d)	$\Sigma A_n/A_0$ (Cl^-)	P_t (Cl^-/cm)	$\Sigma A_n/A_0$ (SO_4^{2-})	P_t ($\text{SO}_4^{2-}/\text{cm}$)	$\Sigma A_n/A_0$ (Mg^{2+})	P_t (Mg^{2+}/cm)
1	0.0066	0.0512	0.0060	0.0636	0.0030	0.8830
2	0.0593	0.4572	0.0350	0.3719	0.0068	2.0000
3	0.0879	0.6781	0.0455	0.4833	0.0101	2.9415
5	0.1182	0.9117	0.0864	0.9190	0.0165	4.8246
7	0.1507	1.1622	0.1136	1.2083	0.0219	6.4152
10	0.1984	1.5303	0.1353	1.4385	0.0340	9.9415

15	0.2585	1.9932	0.1943	2.0659	0.0473	13.8304
20	0.3029	2.3358	0.2173	2.3099	0.0664	19.4152
25	0.3661	2.8234	0.2472	2.6279	0.0815	23.8304
30	0.4094	3.1567	0.2746	2.9196	0.1006	29.4152
35	0.4426	3.4130	0.2900	3.0837	0.1157	33.8304
40	0.4858	3.7463	0.3009	3.1998	0.1328	38.8304
50	0.5123	3.9503	0.3105	3.3019	0.1670	48.8304
60	0.5387	4.1542	0.3192	3.3937	0.2012	58.8304

425 The following hypotheses are proposed for ion migration in the solidified sample:

426 1) The leaching process of the three ions occurs through one-dimensional leaching
427 along the diameter of the solidified sample; 2) The hardened paste is a homogeneous
428 system; 3) The diffusion coefficient is constant; 4) The permeable water is a
429 homogeneous semi-infinite medium; 5) Ions bound by chemical bonding or physical
430 adsorption remain stable during osmotic dissolution; 6) Hardened pastes will not be
431 damaged by corrosion. According to Fick's 2nd law, the equation for ion osmosis
432 migration and diffusion can be obtained. C_0 is the chloride concentration on the
433 exposed surface of concrete. C is the free chloride concentration in diffusion time t .

$$434 \quad \frac{C}{C_0} = \operatorname{erf}\left(\frac{x}{2\sqrt{Dt}}\right) \quad (8)$$

435 The amount of ions penetration and migration in a solidified sample can be
436 obtained by Fick's 1st law:

$$437 \quad J(t) = -D \frac{\partial C}{\partial x} \Big|_{x=0} = -C_0 \sqrt{\frac{D}{\pi t}} \quad (9)$$

438 The amount of ions migration in a solidified sample per unit area at t migration
439 period can be expressed as:

$$440 \quad A_n(t) = \int_0^t J(t) dt = 2A_0 \sqrt{\frac{Dt}{\pi}} \quad (10)$$

441 Where A_n is the accumulated amount of ions dissolved in t migration period, g; A_0 is
442 the initial amount of transferable ions in the solidified sample, g; D is the surface
443 migration coefficient, mm^2/s .

444 According to the above equations and the cumulative migration fraction, P_t , of
445 the ions in the solidified sample, Eq.(11) can be obtained:

$$446 \quad \frac{\sum A_n}{A_0} = 2\left(\frac{S}{V}\right) \sqrt{\frac{Dt}{\pi}} \quad (11)$$

447 Where $\sum A_n$ is the cumulative dissolution amount of ions in t migration period, g; A_0 is

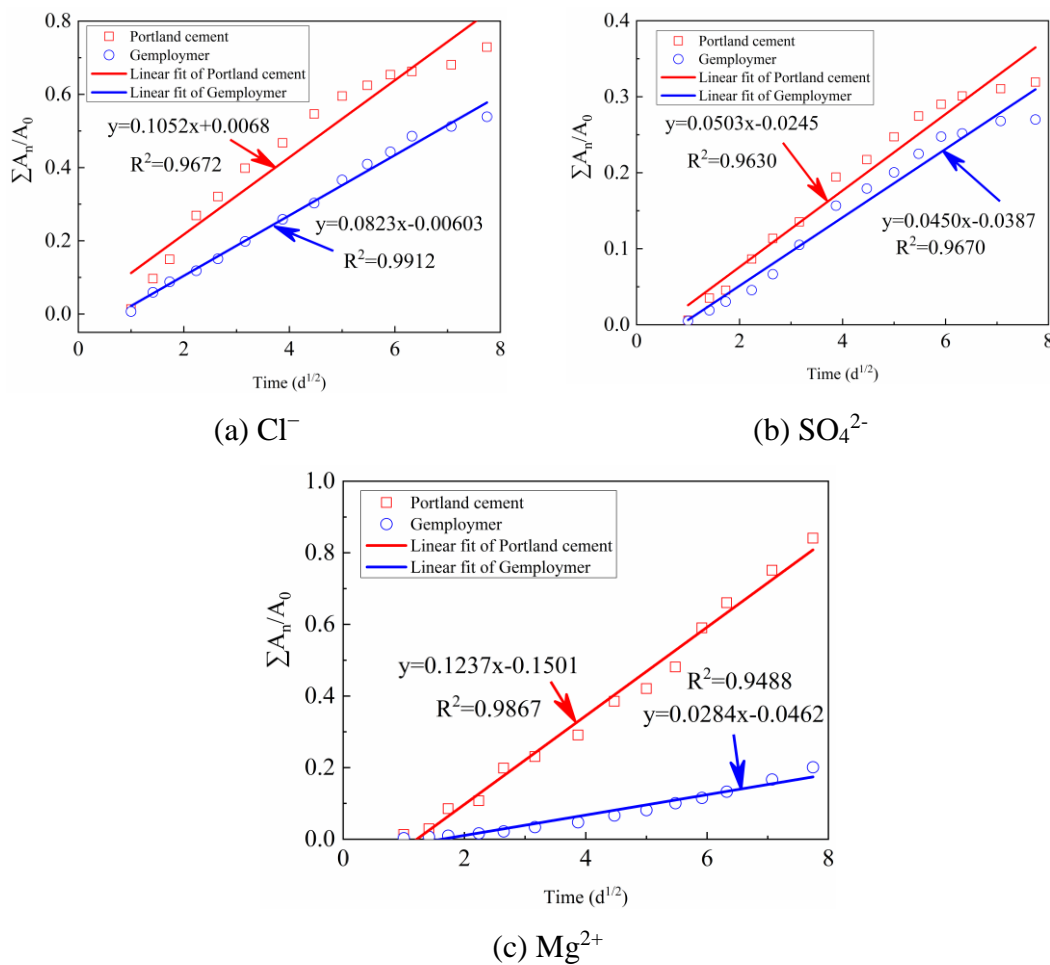
448 the initial amount of transferable ions in the solidified sample, g ; D is the permeability
 449 diffusion coefficient of ions migration, cm^2/d .

450 The migration diffusion coefficient, D , can be obtained from the slope of the line
 451 formed by $\Sigma A_n/A_0$ and $t_n^{1/2}$:

$$452 \quad D = \pi \left(\frac{mV}{2S} \right)^2 \quad (12)$$

453 The cumulative leaching rate ($\Sigma A_n/A_0$) of Cl^- , SO_4^{2-} and Mg^{2+} in the PC mortar and
 454 GP mortar solidified samples obtained by the test is shown in Table 10 and Table 11.

455 The result obtained by curve fitting and $t^{1/2}$ is shown in Fig 6.



456

457

458

Fig. 6. Relationship between $\Sigma A_n/A_0$ and $t_n^{1/2}$

459 According to the fitting results in Fig. 6, the ions diffusion coefficient D of GP
 460 and PC mortar in seawater can be calculated by Eq. (12). Table 12 shows that the
 461 chloride diffusion coefficient of GP mortar is only $6.15 \times 10^{-4} \text{ mm}^2/\text{s}$, which is 61.2%
 462 of that of PC mortar. The sulphate diffusion coefficient of GP mortar is about 1.84×10^{-4}
 463 $\text{ mm}^2/\text{s}$, which is 81.1% of that of PC mortar. The Magnesium ion diffusion

464 coefficient of GP mortar is $0.73 \times 10^{-4} \text{ mm}^2/\text{s}$, which is only 5.3% of that of PC mortar.
 465 In other words, GP shows excellent performance to resist ions migration.

466 **Table 12** Diffusion coefficient of Cl^- , SO_4^{2-} and Mg^{2+} in GP mortar and PC mortar

Material type	D (Cl^-) / ($\times 10^{-4} \text{ mm}^2/\text{s}$)	D (SO_4^{2-}) / ($\times 10^{-4} \text{ mm}^2/\text{s}$)	D (Mg^{2+}) / ($\times 10^{-4} \text{ mm}^2/\text{s}$)
GP mortar	6.15	1.84	0.73
PC mortar	10.06	2.30	1.39

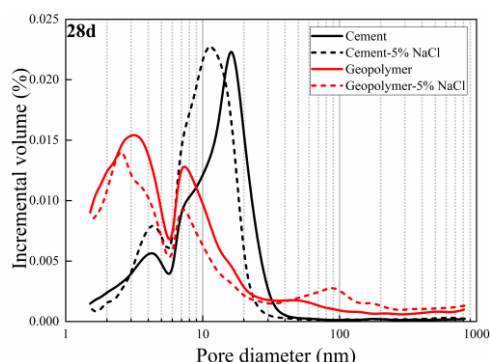
467 4.4 Effect of corrosive ions on pore structure of GP pastes

468 The pore size distributions of cement paste and geopolymer paste with a 28-day
 469 curing age were measured using MIP. The influence of NaCl , Na_2SO_4 , and MgSO_4 on
 470 pore distribution is presented in Fig. 7. The results demonstrate that the pore size and
 471 total porosity of the geopolymer are much smaller than those of the cement. In the
 472 geopolymer pastes, the pore size after 28 days of age is typically smaller than 20 nm.

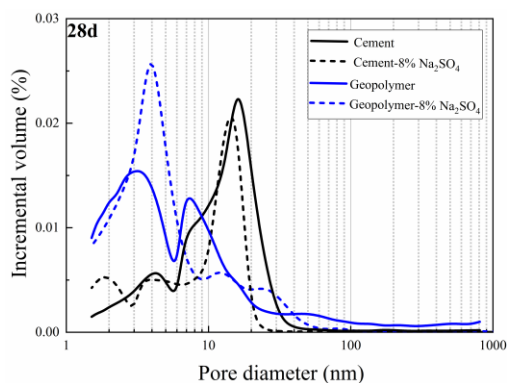
473 Fig. 7(a) shows that the introduction of 5% NaCl has a minimal effect on the
 474 total porosity of the cement paste but refines the pore size. On the other hand, the pore
 475 size of the geopolymer pastes remains relatively unchanged, but the total porosity
 476 decreases significantly with the introduction of 5% NaCl . When considering the initial
 477 and final setting times of the geopolymer pastes, it can be observed that the
 478 introduction of 5% Cl^- delays the reaction speed and increases the reaction degree,
 479 resulting in a decrease in total porosity.

480 Fig. 7(b) and Fig. 7(c) demonstrate that the median pore size of the geopolymer
 481 paste increases with the addition of 8% SO_4^{2-} , while the median pore size of the
 482 cement paste decreases. It is worth noting that the results indicate a decreasing trend
 483 in the number of large pores in the geopolymer paste with the addition of SO_4^{2-} , while
 484 the number of small pores increases significantly. The observed phenomena can be
 485 attributed to the early-stage erosion process, where the erosion products of SO_4^{2-} tend
 486 to initially fill the pores, resulting in a reduction of the median pore size in the cement
 487 paste. Furthermore, the introduction of 8% Mg^{2+} causes a notable increase in the
 488 number of macropores in the cement paste, while simultaneously leading to a
 489 significant decrease in the percentage of macropores in the geopolymer. This
 490 observation suggests that Mg^{2+} erosion converts the hydration product C-S-H gel into
 491 M-S-H, leading to the formation of loosely structured macropores. As a consequence

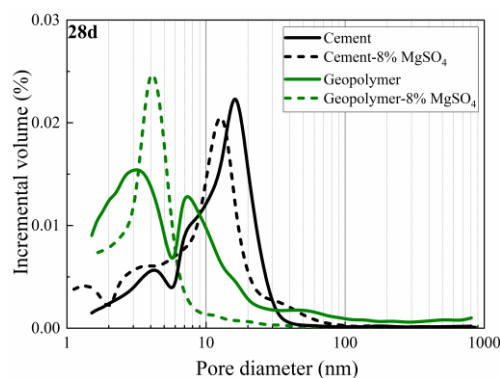
492 of these findings, it can be inferred that geopolymers exhibit favorable resistance to
 493 the penetration of erosive materials, which can be attributed to their compact pore
 494 structure.



(a) Pastes with NaCl



(b) Pastes with Na₂SO₄



(c) Pastes with MgSO₄

495 **Fig.7.** Pore size distribution of geopolymer and cement pastes with NaCl, Na₂SO₄ and
 496 MgSO₄

497 **4.5 Time-dependence regulation of mechanical properties of BFRP bars in**
 498 **seawater**

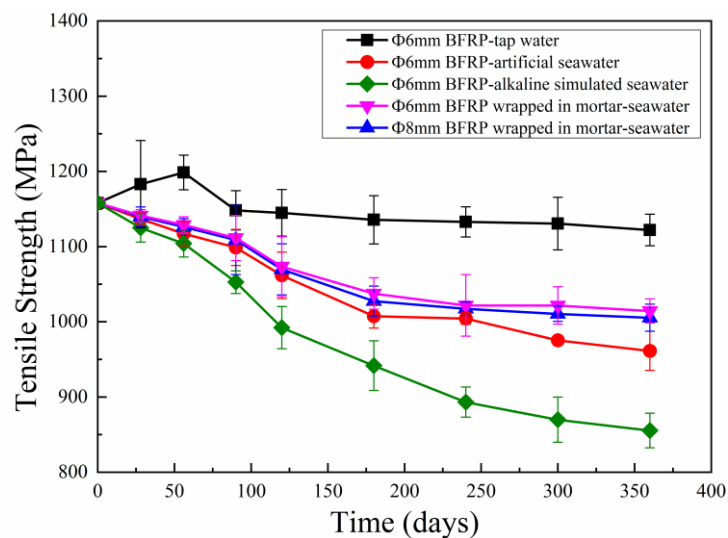
499 Fig. 8 illustrates the degradation of tensile strength for bare BFRP bars with
 500 diameters of Φ 6mm and Φ 8mm when immersed in different media (tap water,
 501 artificial seawater, and alkaline simulated seawater). It also shows the degradation of
 502 BFRP bars with a diameter of Φ 6mm that were wrapped in mortar and immersed in
 503 artificial seawater for varying periods of time. In all solutions, the tensile strengths of
 504 BFRP bars initially decrease rapidly and then exhibit a slower decrease as the
 505 exposure period increases.

506 One possible explanation for this phenomenon is that the corrosion medium
 507 reaches equilibrium after diffusing to a certain depth within the BFRP bars, causing

508 the corrosion reaction to slow down due to the accumulation of reaction products.
 509 Notably, the degradation is significantly accelerated in alkaline environments. The
 510 trend of tensile strength retention for BFRP bars under the same conditions follows
 511 this order: tap water immersion > artificial seawater immersion > alkaline seawater
 512 immersion.

513 It is important to mention that the tensile strength degradation of BFRP bars
 514 wrapped in mortar and immersed in seawater for 360 days was found to be 6%
 515 stronger compared to bare BFRP bars. Additionally, when comparing the tensile
 516 strength of Φ 6mm and Φ 8mm BFRP bars wrapped in mortar, it is observed that the
 517 degradation of tensile strength is more pronounced in the larger diameter bars.

518



519

520 **Fig.8.** Variation of tensile strength of BFRP bars in different corrosive solutions

521 **4.6 Microstructure of BFRP bars in seawater**

522 Fig. 9 presents SEM images of the cross section of Φ 6mm BFRP bars immersed
 523 in different media for a period of 180 days. In Fig. 9(a), which represents immersion
 524 in tap water, it is evident that a significant amount of resin remains bonded to the
 525 surface of the fibers. This bonding facilitates the formation of tight bundles as the
 526 fibers combine with each other.

527

528 In Fig. 9(b), corresponding to immersion in artificial seawater, the outer fibers
 529 display the presence of pores at the edge of the cross-section, and the surface structure

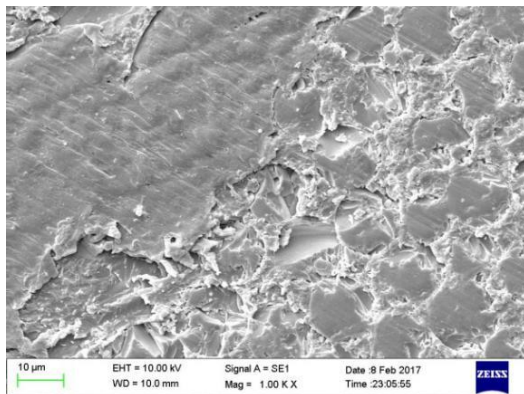
530 appears to have loosened due to corrosion.

531

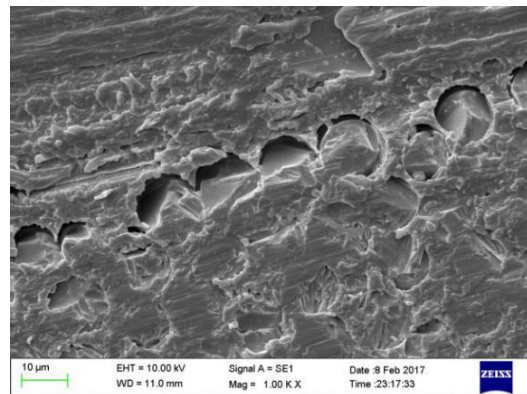
532 Fig. 9(c) illustrates the cross section of BFRP bars after immersion in alkaline
533 simulated seawater. The damage process is visibly pronounced, characterized by fiber
534 ruptures, resin degradation, and debonding of the resin-fiber interface. This results in
535 an increased loose area and noticeable protrusion of fibers.

536

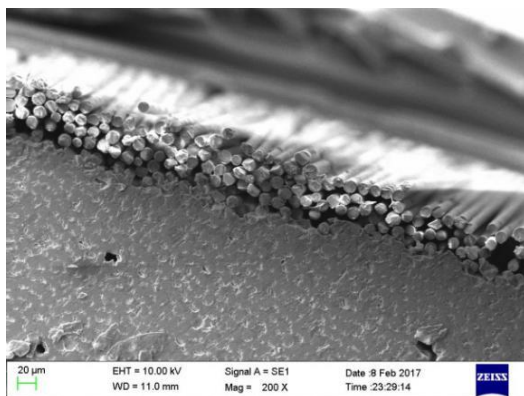
537 These SEM images provide insight into the changes and damage experienced by
538 the BFRP bars under different immersion conditions, highlighting the effects of
539 various media on the surface and structural integrity of the bars.



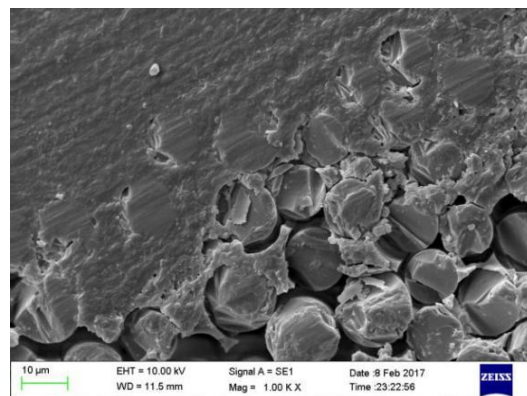
(a) BFRP bar immersed in water



(b) BFRP bar immersed in artificial seawater



(c) BFRP bar immersed in saturated Ca(OH)₂ seawater



540 **Fig.9.** Microstructure of cross section of BFRP bars after 180 days corrosion

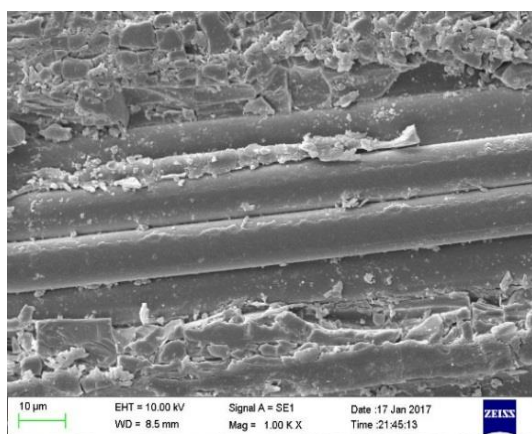
541 Fig. 10 displays SEM micrographs of the longitudinal section of Φ 6mm BFRP

542 bars subjected to different immersion media for a duration of 180 days. In Fig. 10(a),
543 representing immersion in tap water, the surface of the fiber and resin remains
544 unchanged. The fiber maintains a smooth and flat appearance, tightly connected to the
545 resin.

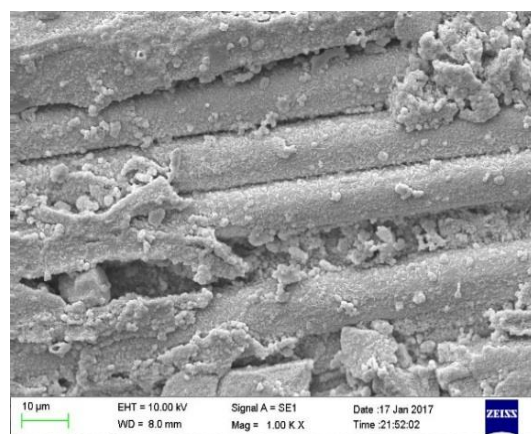
546 In Fig. 10(b), following immersion in seawater, the intermediate resin that
547 bonded the fibers together disappears, leading to a further loosening of the fiber
548 bundles. Additionally, a significant amount of salt crystals can be observed attached
549 to the surface.

550 Fig. 10(c) reveals that after immersion in alkaline simulated seawater, very little
551 resin remains bonded to the fiber surface. The fibers exhibit evident corrosion, with
552 signs of detachment and noticeable damage defects. This phenomenon can be
553 attributed to the gradual penetration of the corrosive medium along the radial
554 direction of the bars. Initially, the shedding of fiber and resin occurs, followed by
555 fiber surface corrosion in the later stages. These factors contribute to a significant
556 decrease in the tensile strength of the BFRP bars.

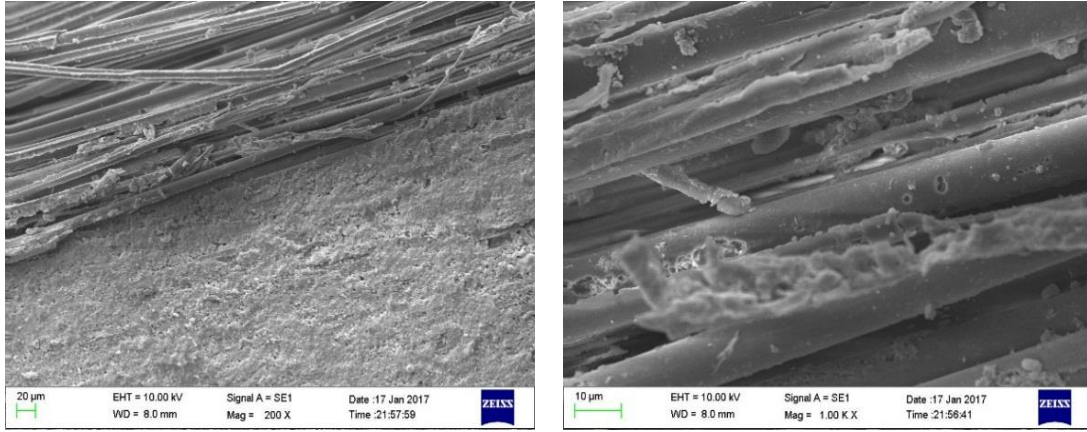
557 The observations presented in Fig. 10, along with those in Fig. 9, demonstrate
558 the decisive influence of alkaline environments on the degradation of tensile strength
559 in BFRP bars. This finding aligns with the results obtained from the tensile strength
560 tests.



(a) BFRP bar immersed in water



(b) BFRP bar immersed in artificial seawater



(c) BFRP bar immersed in saturated Ca(OH)_2 seawater

561 **Fig.10.** Microstructure of vertical section of BFRP bars after 180d corrosion

562 **4.7 Degradation model of tensile strength of BFRP bars in marine environments**

563 Through microscopic analysis of BFRP bars, the degradation mechanism in a
 564 seawater environment is identified as fiber-resin matrix interface split and separated
 565 failure. This mechanism can be expressed as follows [46]:

566
$$f_f = (100 - Y_\infty) \exp\left(-\frac{t}{\tau}\right) + Y_\infty \quad (13)$$

567 Where, Y_∞ is the residual tensile strength of BFRP bars when the corrosion time tends
 568 to infinity; τ is the characteristic time determined by corrosion temperature.

569 The corrosion of BFRP bars that are wrapped in GPC in marine environments is
 570 primarily caused by seawater corrosion and the alkaline environment within the GPC.
 571 Therefore, Eq (13) is modified as follows:

572
$$f_f = Y_\infty \times \exp(-b \times t)^c + Y_\infty \quad (14)$$

573 To verify the modified Eq. (14), the time-dependent variation of tensile
 574 properties of Φ 6 mm and Φ 8 mm BFRP bars wrapped in GP mortar under seawater
 575 immersion is fitted, as shown in Fig. 11. The fitting parameters are presented in Table
 576 13. In the seawater environment, the final strengths of Φ 6 mm and Φ 8 mm BFRP
 577 bars are 695 MPa and 663 MPa, respectively. The established tensile strength
 578 degradation models for the BFRP bars are as follows:

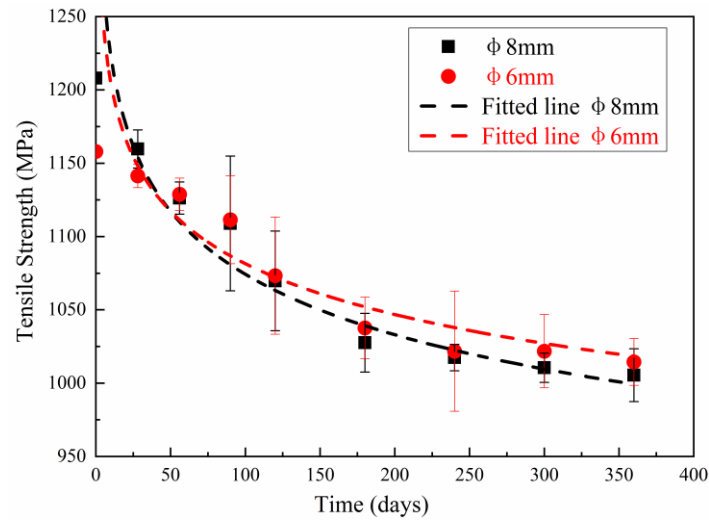
579 Φ 6 mm BFRP bar:

580
$$f_f = 695.38 \times (1 - \exp(-8.19958E - 7 \times t))^{-0.04694} \quad (15)$$

581 Φ 8 mm BFRP bar:

582

$$f_f = 663.76 \times (1 - \exp(-1.98349E - 6 \times t))^{-0.04248} \quad (16)$$



583

584

Fig.11. Tensile strength of BFRP immersed in a marine environment

585

Table 13 Parameters of the fitting equation to describe the degradation of BFRP bars

	Φ6 mm	Φ8 mm
Y_{∞}	695.38	663.76
b	8.19958E-7	1.98349E-6
c	-0.04694	-0.04248
R^2	0.92197	0.95115

586

4.8 Microstructure characteristics of the interface of BFRP bars reinforced

587

geopolymer in seawater

588

4.8.1 Microscopic properties of the interface between geopolymer and aggregate in

589

seawater

590

The microscopic morphology of hardened samples of GPC and PC concrete after

591

immersion in tap water and artificial seawater for 360 days is depicted in Fig. 12 and

592

13. The backscattered electron (BSE) images of the hardened samples reveal certain

593

characteristics. The brightly colored irregular blocks represent unreacted clinker or

594

slag, while the brightly colored globular particles indicate unreacted fly ash. The gray

595

areas correspond to the reaction products formed during the reaction, and the black

596

areas represent pores within the hardened samples.

597

Fig. 12(a) demonstrates that in tap water for 360 days, the GP mortar exhibits a

598

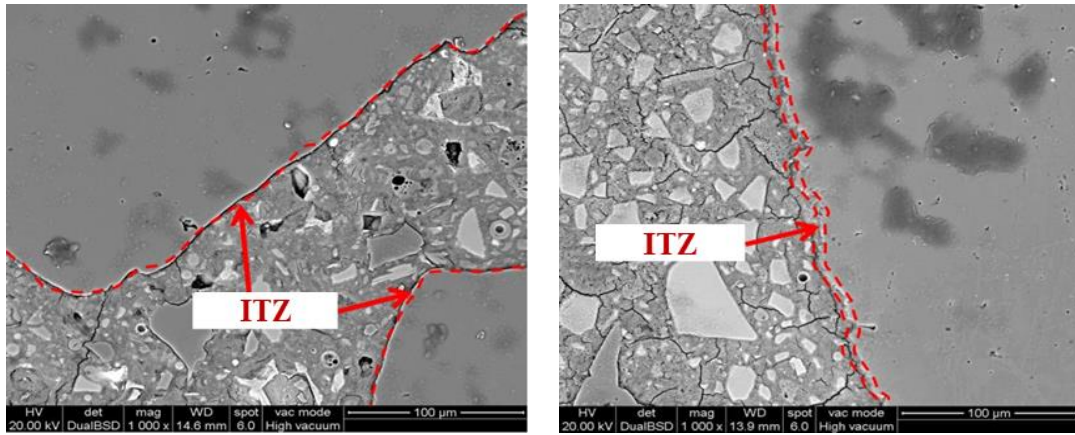
tight bond with the aggregate, without a distinct boundary of interfacial transition. Fig.

599

12(b) shows that after immersion in artificial seawater for 360 days, the interface area

600 between the GP mortar and aggregate does not show a significant increase, but some
601 areas exhibit fine cracks.

602 Fig. 13(a) illustrates that in the PC concrete samples, there is a wide black area
603 accompanied by a distribution of porosity between the PC mortar and aggregate. This
604 indicates the presence of an obvious interfacial transition zone (ITZ) in the PC
605 concrete samples, which is more pronounced compared to the GPC samples. Fig. 13(b)
606 further demonstrates that the ITZ of the PC concrete samples becomes more apparent
607 after seawater corrosion, along with a higher proportion of pores and cracks.

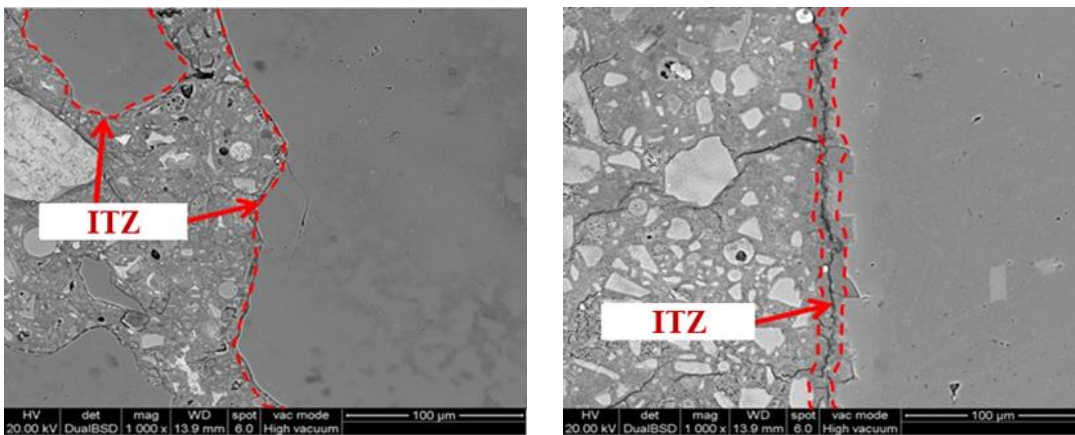


(a) GPC in water for 360 days

(b) GPC in artificial seawater for 360 days

608

Fig. 12. Interfacial transition zone of GPC after 360 days corrosion



(a) PC concrete in water for 360 days

(b) PC concrete in artificial seawater for 360
days

609

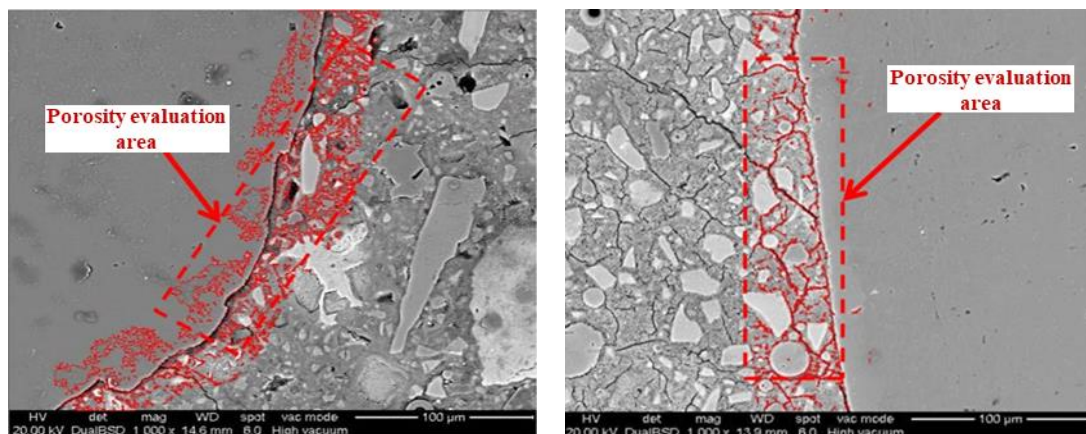
Fig. 13. Interfacial transition zone of PC concrete after 360 days corrosion

610 The porosity of the interfacial transition zone (ITZ) in concrete was further
611 calculated using the fractal theory with the aid of Image-Pro Plus (IPP) image

612 processing software. Fig. 14 and 15 display the IPP image processing photos of the
613 ITZ in GPC and PC concrete, respectively, while Table 14 presents the statistical
614 results of porosity.

615 After immersion in tap water for 360 days, the average porosity of the ITZ in
616 GPC and PC concrete samples is approximately 27.89% and 37.97%, respectively.
617 This indicates that the average porosity of the ITZ in GPC is approximately 36.0%
618 lower than that in PC concrete.

619 Following 360 days of artificial seawater corrosion, the average porosity of the
620 ITZ in GPC samples only increases by 4.44%, reaching approximately 29.13% in total.
621 In contrast, the average porosity of the ITZ in PC concrete increases from 37.97% to
622 40.74%, exhibiting a 7.29% increase compared to 360 days of tap water corrosion.
623 These findings indicate that GPC possesses a smaller porosity and a lower proportion
624 of porosity increase compared to PC concrete after seawater corrosion. This
625 demonstrates the excellent resistance of GPC to seawater corrosion.

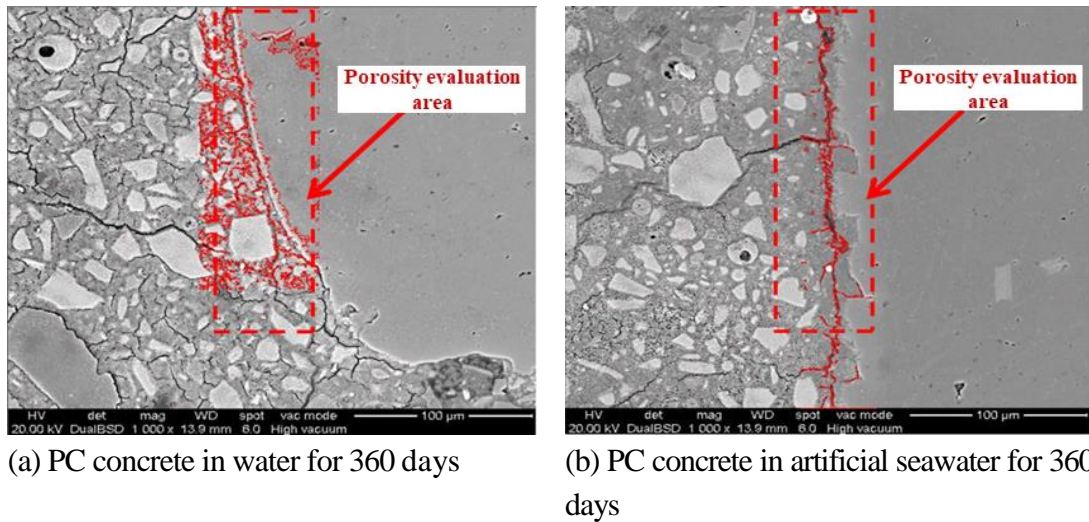


(a) GPC in water for 360 days

(b) GPC in artificial seawater for 360 days

626

Fig. 14. Interfacial transition zone of GPC after corrosion



627 **Fig. 15.** Interfacial transition zone of PC concrete after corrosion

628 **Table 14** Porosity of interfacial transition zone in concrete after corrosion

Porosity	GPC		PC concrete	
	water for 360 d	artificial Seawater 360 d	Reference	artificial Seawater 360 d
Range	23.25~31.43	22.53~33.30	32.03~43.26	34.06~47.06
Average value(%)	27.89	29.13	37.97	40.74

629 Note. 10 images were selected to analyze the porosity of the interfacial transition zone
630 of concretes.

631 4.8.2 Microstructure characteristics of interface between BFRP bars and geopolymer
632 in seawater

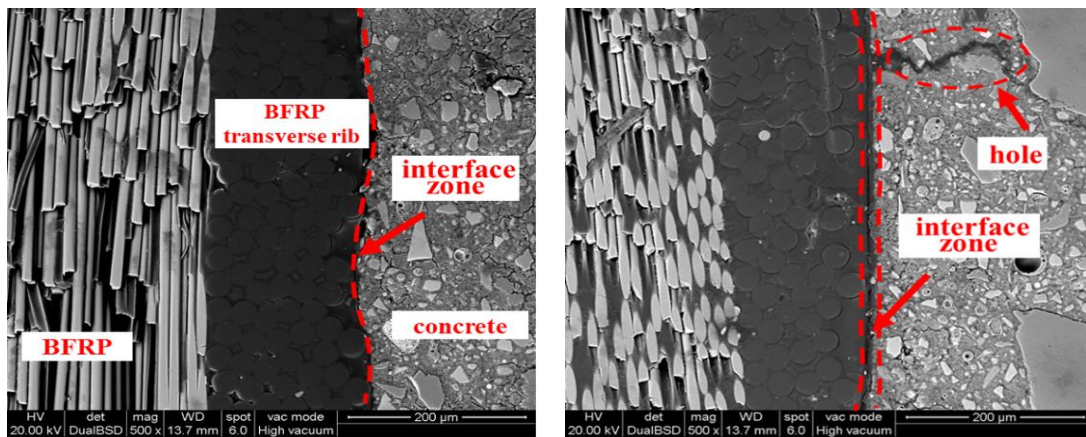
633 In the seawater environment, the microstructure characteristics of the interface
634 between BFRP bars and GPC were examined. Fig. 16 (a) illustrates that the BFRP
635 bars consist of basalt fibers bonded with resin and are further reinforced with
636 transverse ribs. The interface between the BFRP bars and GPC exhibits a tight bond
637 without any distinct interfacial transition zone (ITZ) or noticeable interfacial pores.

638 After 360 days of seawater corrosion, as shown in Fig. 16 (b), the interface
639 between the BFRP bars and GPC slightly expanded. Some cracks and pores appeared
640 in the GPC, but the bond between the GPC and BFRP bars remained relatively tight.

641 These observations suggest that even after seawater corrosion, the bond between
642 the BFRP bars and GPC remains intact, indicating the favorable compatibility and

643 durability of the interface in the seawater environment.

644 Fig. 16 (a) shows that BFRP bars are composed of resin bonded basalt fibers and
645 then wound with transverse ribs. BFRP bars are tightly bonded to GPC with no
646 obvious ITZ and no obvious interfacial pores. Fig. 16 (b) shows that the interface
647 between BFRP bars and GPC was slightly enlarged after 360 days of seawater
648 corrosion, and GPC appear some cracks and pores. It is noted that the bond between
649 the GPC and BFRP bars is still relatively tight.



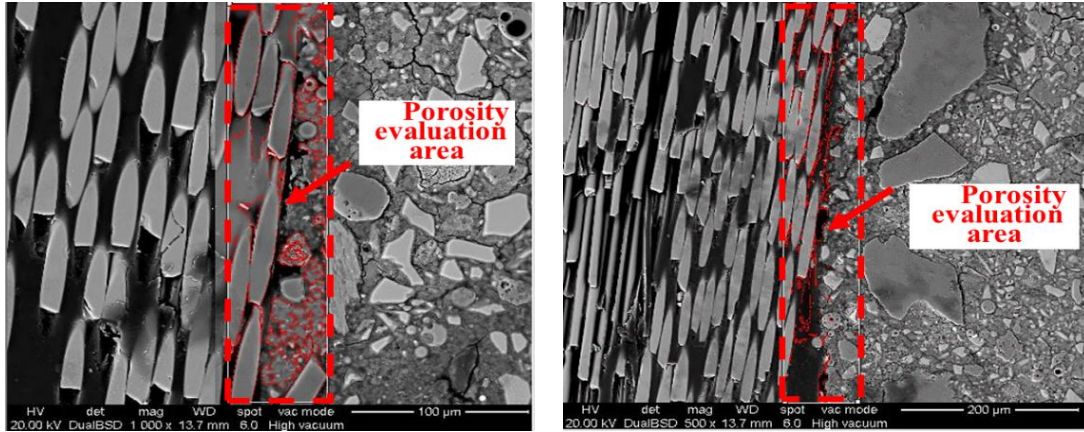
(a) Before corrosion

(b) After artificial seawater for 360 days

650 **Fig. 16.** Interface between BFRP bars and GPC before and after corrosion

651 To analyze the porosity of the interface area between the BFRP bars and GPC,
652 IPP image processing software was utilized. Fig. 17 presents the results of porosity
653 analysis before and after artificial seawater corrosion. The statistical data of porosity
654 are summarized in Table 15.

655 Before seawater corrosion, the interface between the BFRP bars and GPC
656 exhibited a tight bond, and the average porosity of the interfacial transition zone (ITZ)
657 was measured to be 27.88%. Following seawater corrosion, the average porosity of
658 the ITZ increased slightly to 29.06%, which represents a 1.2% increment compared to
659 the pre-corrosion condition. These results indicate that seawater corrosion has a
660 negligible impact on the porosity of the ITZ between the GPC and BFRP bars.



(a) GPC in water

(b) GPC in artificial seawater for 360 days

661 **Fig. 17.** Interfacial transition zone of BFRP bars in GPC after corrosion

662 **Table 15** Porosity of interface between BFRP bars and GPC after corrosion

Porosity/%	GPC	
	Reference	Immersed in artificial seawater for 360 days
Range	24.10~31.58	24.90~33.30
Average value/%	27.88	29.06

663 Note. 10 images were selected to analyze the porosity of the interface between BFRP
664 and GPC.

665 5 Conclusion

666 This study focused on investigating the corrosion resistance and interface
667 characteristics of GPC and BFRP bars in a seawater environment. The main emphasis
668 of this research was on analyzing the ionic attack resistance of BFRP reinforced
669 geopolymer concrete using laboratory-simulated seawater conditions. However, it is
670 essential to acknowledge that in actual marine environments, ion migration occurs not
671 only through diffusion but also potentially involves convective effects under
672 hydrostatic pressure.

673 Several critical questions remain to be addressed: How can we simulate ocean
674 conditions more realistically through systematically designed experiments? What are
675 the effects of competing antagonistic processes on the performance of BFRP
676 reinforced geopolymer concrete when subjected to multiple-ion combined attack in
677 marine environments? To answer these questions, further studies employing
678 systematically designed experiments and long-term observations will be crucial. Such
679 research endeavors will not only help refine the proposed mathematical models but
680 also enhance our understanding of the behavior of BFRP reinforced geopolymer

681 concrete under realistic marine conditions.

682 Based on the findings of the present study, the following specific conclusions
683 may be drawn:

684 (1) The corrosion resistance of GPC exhibited an initial sharp increase, followed by a
685 slower increase, and finally reached a stable state after 90 days of exposure. The
686 volume corrosion resistance coefficient and strength corrosion resistance
687 coefficient of GPC after 360 days of immersion were 0.06 and 0.085, respectively,
688 indicating excellent resistance to seawater corrosion. A degradation model for the
689 mechanical performance of GPC in a marine environment was established.

690

691 (2) GP mortar demonstrated superior resistance to ion migration compared to PC
692 mortar. The migration properties of chloride ions (Cl^-), sulfate ions (SO_4^{2-}), and
693 magnesium ions (Mg^{2+}) were evaluated, with Cl^- showing the highest migration,
694 followed by SO_4^{2-} and Mg^{2+} .

695

696 (3) The tensile strength degradation of BFRP bars in seawater combined with an
697 alkaline environment was more pronounced than in seawater alone. Wrapping
698 BFRP bars in GP mortar mitigated the reduction in tensile strength in seawater,
699 and a smaller BFRP diameter resulted in reduced deterioration. The ultimate
700 strengths of BFRP bars with diameters of 6 mm and 8 mm were 695 MPa and 663
701 MPa, respectively. A degradation model for the tensile strength of BFRP bars in
702 marine environments was established.

703

704 (4) Microscopic analysis revealed that seawater corrosion had little impact on the
705 porosity of the dual interfaces in BFRP bars reinforced with geopolymer concrete.
706 The average porosity of the interfacial transition zone (ITZ) between GP paste
707 and aggregate was significantly lower than that of PC concrete. The ITZ between
708 BFRP bars and GP paste exhibited a slight increase in porosity, but still
709 maintained tight interfacial bonding and narrow interface widths. Seawater
710 corrosion did not significantly affect the ITZ structure of BFRP reinforced
711 geopolymer concrete.

712

713 These findings contribute to a better understanding of the corrosion behavior and

714 interface characteristics of GPC and BFRP bars in seawater environments, and
715 provide valuable insights for the development of corrosion-resistant and durable
716 concrete structures.

717

718 **ACKNOWLEDGEMENTS**

719 This study was funded by Natural Science Foundation of Guangxi Province
720 (2021GXNSFAA220045), China Postdoctoral Science Foundation (2021M690765),
721 Systematic Project of Guangxi Key Laboratory of Disaster Prevention and
722 Engineering Safety (2021ZDK007), National Key Research and Development
723 Program of China (2021YFB2600903) and National Natural Science Foundation of
724 China (U2006224).

725

726 **REFERENCE**

- 727 [1] Zhang B, Zhu H, Li F Z, Dong Z Q, Zhang P. Compressive stress-strain
728 behavior of seawater coral aggregate concrete incorporating eco-efficient
729 alkali-activated slag materials [J]. *Construction and Building Materials*, 2021,
730 299.
- 731 [2] Zhang B, Zhu H, Cao R M, Ding J M, Chen X H. Feasibility of using
732 geopolymers to investigate the bond behavior of FRP bars in seawater sea-
733 sand concrete [J]. *Construction and Building Materials*, 2021, 282.
- 734 [3] Zhang B, Zhu H, Lu F. Fracture properties of slag-based alkali-activated
735 seawater coral aggregate concrete [J]. *Theoretical and Applied Fracture*
736 *Mechanics*, 2021, 115.
- 737 [4] Chen G, Zheng D P, Chen Y W, Lin J X, Lao W J, Guo Y C, Chen Z B, Lan X
738 W. Development of high performance geopolymer concrete with waste rubber
739 and recycle steel fiber: A study on compressive behavior, carbon emissions
740 and economical performance [J]. *Construction and Building Materials*, 2023,
741 393.
- 742 [5] Elahi M M A, Hossain M M, Karim M R, Zain M F M, Shearer C. A review
743 on alkali-activated binders: Materials composition and fresh properties of
744 concrete [J]. *Construction and Building Materials*, 2020, 260.
- 745 [6] Morsy A M, Ragheb A M, Shalan A H, Mohamed O H. Mechanical
746 Characteristics of GGBFS/FA-Based Geopolymer Concrete and Its
747 Environmental Impact [J]. *Practice Periodical on Structural Design and*
748 *Construction*, 2022, 27(2).
- 749 [7] Perumal P, Sreenivasan H, Luukkonen T, Kantola A M, Telkki V V, Kinnunen
750 P, Illikainen M. High strength one-part alkali-activated slag blends designed

- 751 by particle packing optimization [J]. *Construction and Building Materials*,
752 2021, 299.
- 753 [8] Shehata N, Sayed E T, Abdelkareem M A. Recent progress in environmentally
754 friendly geopolymers: A review [J]. *Science of The Total Environment*, 2021,
755 762: 143166.
- 756 [9] Wang A G, Zheng Y, Zhang Z H, Liu K W, Li Y, Shi L, Sun D S. The
757 Durability of Alkali-Activated Materials in Comparison with Ordinary
758 Portland Cements and Concretes: A Review [J]. *Engineering*, 2020, 6(6): 695-
759 706.
- 760 [10] Zhang B, Zhu H, Wang Q, Shah K W, Wang W. Design and properties of
761 seawater coral aggregate alkali-activated concrete [J]. *Journal of Sustainable
762 Cement-Based Materials*, 2022, 11(3): 175-84.
- 763 [11] Xiao J Z, Qiang C B, Nanni A, Zhang K J. Use of sea-sand and seawater in
764 concrete construction: Current status and future opportunities [J]. *Construction
765 and Building Materials*, 2017, 155: 1101-11.
- 766 [12] Li J L, Xie J H, Liu F, Lu Z Y. A critical review and assessment for FRP-
767 concrete bond systems with epoxy resin exposed to chloride environments [J].
768 *Composite Structures*, 2019, 229.
- 769 [13] Lu Z Y, Li J L, Xie J H, Huang P Y, Xue L F. Durability of flexurally
770 strengthened RC beams with prestressed CFRP sheet under wet-dry cycling in
771 a chloride-containing environment [J]. *Composite Structures*, 2021, 255.
- 772 [14] Yan F, Lin Z B, Yang M J. Bond mechanism and bond strength of GFRP bars
773 to concrete: A review [J]. *Composites Part B-Engineering*, 2016, 98: 56-69.
- 774 [15] Torres L, Sharaky I A, Barris C, Baena M. EXPERIMENTAL STUDY OF
775 THE INFLUENCE OF ADHESIVE PROPERTIES AND BOND LENGTH
776 ON THE BOND BEHAVIOUR OF NSM FRP BARS IN CONCRETE [J].
777 *Journal of Civil Engineering and Management*, 2016, 22(6): 808-17.
- 778 [16] Aslani F, Sun J B, Bromley D, Ma G W. Fiber-reinforced lightweight self-
779 compacting concrete incorporating scoria aggregates at elevated temperatures
780 [J]. *Structural Concrete*, 2019, 20(3): 1022-35.
- 781 [17] Aslani F, Sun J B, Huang G Q. Mechanical Behavior of Fiber-Reinforced Self-
782 Compacting Rubberized Concrete Exposed to Elevated Temperatures [J].
783 *Journal of Materials in Civil Engineering*, 2019, 31(12).
- 784 [18] Thomas R J, Ariyachandra E, Lezama D, Peethamparan S. Comparison of
785 chloride permeability methods for Alkali-Activated concrete [J]. *Construction
786 and Building Materials*, 2018, 165: 104-11.
- 787 [19] Gunasekara C, Law D, Bhuiyan S, Setunge S, Ward L. Chloride induced
788 corrosion in different fly ash based geopolymer concretes [J]. *Construction
789 and Building Materials*, 2019, 200: 502-13.
- 790 [20] Amorim Júnior N S, Andrade Neto J S, Santana H A, Cilla M S, Ribeiro D V.
791 Durability and service life analysis of metakaolin-based geopolymer concretes
792 with respect to chloride penetration using chloride migration test and corrosion
793 potential [J]. *Construction and Building Materials*, 2021, 287: 122970.
- 794 [21] Monticelli C, Natali M E, Balbo A, Chiavari C, Zanutto F, Manzi S, Bignozzi

- 795 M C. Corrosion behavior of steel in alkali-activated fly ash mortars in the light
 796 of their microstructural, mechanical and chemical characterization [J]. *Cement*
 797 *and Concrete Research*, 2016, 80: 60-8.
- 798 [22] Dzunuzovic N, Komljenovic M, Nikolic V, Ivanovic T. External sulfate attack
 799 on alkali-activated fly ash-blast furnace slag composite [J]. *Construction and*
 800 *Building Materials*, 2017, 157: 737-47.
- 801 [23] Kuri J C, Nuruzzaman M, Sarker P K. Sodium sulphate resistance of
 802 geopolymer mortar produced using ground ferronickel slag with fly ash [J].
 803 *Ceramics International*, 2023, 49(2): 2765-73.
- 804 [24] Elyamany H E, Abd Elmoaty A M, Elshaboury A M. Magnesium sulfate
 805 resistance of geopolymer mortar [J]. *Construction and Building Materials*,
 806 2018, 184: 111-27.
- 807 [25] Saavedra W G V, Angulo D E, De Gutierrez R M. Fly Ash Slag Geopolymer
 808 Concrete: Resistance to Sodium and Magnesium Sulfate Attack [J]. *Journal of*
 809 *Materials in Civil Engineering*, 2016, 28(12).
- 810 [26] Pasupathy K, Berndt M, Sanjayan J, Rajeev P, Cheema D S. Durability of low-
 811 calcium fly ash based geopolymer concrete culvert in a saline environment [J].
 812 *Cement and Concrete Research*, 2017, 100: 297-310.
- 813 [27] Tennakoon C, Shayan A, Sanjayan J G, Xu A M. Chloride ingress and steel
 814 corrosion in geopolymer concrete based on long term tests [J]. *Materials &*
 815 *Design*, 2017, 116: 287-99.
- 816 [28] Dong Z Q, Wu G, Zhao X L, Zhu H, Lian J L. Durability test on the flexural
 817 performance of seawater sea-sand concrete beams completely reinforced with
 818 FRP bars [J]. *Construction and Building Materials*, 2018, 192: 671-82.
- 819 [29] Monticelli C, Natali M E, Balbo A, Chiavari C, Zanotto F, Manzi S, Bignozzi
 820 M C. A study on the corrosion of reinforcing bars in alkali-activated fly ash
 821 mortars under wet and dry exposures to chloride solutions [J]. *Cement and*
 822 *Concrete Research*, 2016, 87: 53-63.
- 823 [30] Tittarelli F, Mobili A, Giosue C, Belli A, Bellezze T. Corrosion behaviour of
 824 bare and galvanized steel in geopolymer and Ordinary Portland Cement based
 825 mortars with the same strength class exposed to chlorides [J]. *Corrosion*
 826 *Science*, 2018, 134: 64-77.
- 827 [31] Wang W R, Chen H S, Li X Y, Zhu Z G. Corrosion behavior of steel bars
 828 immersed in simulated pore solutions of alkali-activated slag mortar [J].
 829 *Construction and Building Materials*, 2017, 143: 289-97.
- 830 [32] Wang Z K, Zhao X L, Xian G J, Wu G, Raman R K S, Al-Saadi S, Haque A.
 831 Long-term durability of basalt- and glass-fibre reinforced polymer
 832 (BFRP/GFRP) bars in seawater and sea sand concrete environment [J].
 833 *Construction and Building Materials*, 2017, 139: 467-89.
- 834 [33] Lu C H, Ni M Z, Chu T S, He L Y. Comparative Investigation on Tensile
 835 Performance of FRP Bars after Exposure to Water, Seawater, and Alkaline
 836 Solutions [J]. *Journal of Materials in Civil Engineering*, 2020, 32(7).
- 837 [34] Lu Z Y, Li Y C, Xie J H. Durability of BFRP bars wrapped in seawater sea
 838 sand concrete [J]. *Composite Structures*, 2021, 255.

- 839 [35] Luo Z Y, Li W G, Wang K J, Castel A, Shah S P. Comparison on the properties
840 of ITZs in fly ash-based geopolymer and Portland cement concretes with
841 equivalent flowability [J]. *Cement and Concrete Research*, 2021, 143.
- 842 [36] Cai Y J, Xiao S H, Chen Y W, Huang Z R, Lin J X, Guo Y C, Peng Y Q, Xie Z
843 H. Tensile behavior and durability prediction of GFRP-steel composite bars
844 under chloride environments [J]. *Journal of Materials Research and
845 Technology-Jmr&T*, 2023, 23: 5746-59.
- 846 [37] Xiong Z, Wei W, Liu F, Cui C, Li L, Zou R, Zeng Y. Bond behaviour of
847 recycled aggregate concrete with basalt fibre-reinforced polymer bars [J].
848 *Composite Structures*, 2021, 256: 113078.
- 849 [38] Xiong Z, Mai G, Qiao S, He S, Zhang B, Wang H, Zhou K, Li L. Fatigue bond
850 behaviour between basalt fibre-reinforced polymer bars and seawater sea-sand
851 concrete [J]. *Ocean & Coastal Management*, 2022, 218: 106038.
- 852 [39] Zou R, Liu F, Xiong Z, He S, Li L, Wei W. Experimental study on fatigue
853 bond behaviour between basalt fibre-reinforced polymer bars and recycled
854 aggregate concrete [J]. *Construction and Building Materials*, 2021, 270:
855 121399.
- 856 [40] Xiong Z, Wei W, He S, Liu F, Luo H, Li L. Dynamic bond behaviour of fibre-
857 wrapped basalt fibre-reinforced polymer bars embedded in sea sand and
858 recycled aggregate concrete under high-strain rate pull-out tests [J].
859 *Construction and Building Materials*, 2021, 276: 122195.
- 860 [41] Neupane K. "Fly ash and GGBFS based powder-activated geopolymer
861 binders: A viable sustainable alternative of portland cement in concrete
862 industry" [J]. *Mechanics of Materials*, 2016, 103: 110-22.
- 863 [42] Khan M S H, Castel A, Akbarnezhad A, Foster S J, Smith M. Utilisation of
864 steel furnace slag coarse aggregate in a low calcium fly ash geopolymer
865 concrete [J]. *Cement and Concrete Research*, 2016, 89: 220-9.
- 866 [43] Tian Z, Zhang Z, Liu H, Zheng W, Tang X, Gui Z. Interfacial characteristics
867 and mechanical behaviors of geopolymer binder with steel slag aggregate:
868 Insights from molecular dynamics [J]. *Journal of Cleaner Production*, 2022,
869 362: 132385.
- 870 [44] Ren X, Zhang L. Experimental study of interfacial transition zones between
871 geopolymer binder and recycled aggregate [J]. *Construction and Building
872 Materials*, 2018, 167: 749-56.
- 873 [45] Yang Y, Chen Z, Feng W, Nong Y, Yao M, Tang Y. Shrinkage compensation
874 design and mechanism of geopolymer pastes [J]. *Construction and Building
875 Materials*, 2021, 299: 123916.
- 876 [46] Lee S L, Wong S F, Swaddiwudhipong S, Wee T H, Loo Y H. Accelerated test
877 of ingress of chloride ions in concrete under pressure and concentration
878 gradients [J]. *Magazine of Concrete Research*, 1996, 48(174): 15-25.
- 879